Optical properties of transition metal dichalcogenide bilayers

Zhijie Li

München 2023

Optical properties of transition metal dichalcogenide bilayers

Zhijie Li

Dissertation
der Fakultät für Physik
der Ludwig-Maximilians-Universität
München

vorgelegt von
Zhijie Li
aus Shanxi, China

München, den 06.03.2023

Erstgutachter: Prof. Dr. Alexander Högele
Zweitgutachter: Prof. Dr. Alexander Urban
Tag der mündlichen Prüfung: 24.04.2023

Zusammenfassung

Zweidimensionale hableitende Übergangsmetall-Dichalcogenide sind bekannt für einzigartige opto-elektronische Eigenschaften. Sie erlauben auch gezielte Fabrikation von Homobilagen und Heterostrukturen aus einzelnen Monolagen und bieten damit vielfältige Möglichkeiten zur Herstellung neuartiger Quantenmaterialien mit durchstimmbaren optischen und elektronischen Eigenschaften auf Grundlage besonderer Spin-Valley Freiheitsgrade und starker elektronischer Wechselwirkungen. Monolagige Kristalle aus chemischer Gasphasenabscheidung (chemical vapor deposition, CVD) dienen dabei als elementare Bauelemente für vertikal geschichtete van der Waals Strukturen, deren Eigenschaften durch die Anzahl der Lagen sowie ihrer Komposition und Orientierung charakteristisch bestimmt werden können.

Im ersten Teil der vorliegenden Arbeit wurden WSe_2 Homobilagen in zwei gegensätzlichen Orientierungen mittels CVD-Synthese hergestellt und mit optischer Tieftemperatur-Spektroskopie untersucht. Unter kontrollierter CVD-Parametern wurden hochqualitative, lateral ausgedehnte Bilagen mit kontaminationsfreien Grenzflä)chen und strikt paralleler und antiparalleler Orientierung synthetisiert. Mittels komplementärer Techniken der optischen Spektroskopie bei Raumtemperatur und tiefen Temperaturen und unter Hinzunahme theoretischer Modellierung wurden charakteristische Signaturen von Impuls-direkten Exzitonen in der optischen Absorption sowie von Impuls-indirekten Exzitonen in der Photolumineszenz von WSe_2 Homobilagen mit paralleler und antiparalleler kristallographischer Orientierung identifiziert. Die Ergebnisse verknüpfen nicht nur optische Eigenschaften von Homobilagen mit zugrundeliegender Kristallsymmetrie und Schichtung, sie verweisen auch auf die Rolle der Kristallstruktur für die Ausbildung hybrider Interlagen-Exzitonen.

Im zweiten Teil werden Ergebnisse an $MoSe_2$-WSe_2 Heterostrukturen von separat synthetisierten Monolagen vorgestellt. Für derartige Heterostapel mit nahezu kommensurablen Gitterkonstanten ist theoretisch atomare Gitterrekonstruktion von Moiré-Übergittern hin zu periodischen Domänen nanostrukturierter Muster erwartet. In Heterostrukturen mit endlichen Abmessungen wurden jedoch Effekte der Gitterrekonstruktion auf mesoskopischen Skalen mit unmittelbaren Konsequenzen für optische Eigenschaften der Exzitonen beobachtet. Unter Einsatz vielfältiger Methoden der optischen Spektroskopie, korrelativer Bildgebung rekonstruierter Domänen

mittels Rasterelektronenmikroskopie und theoretischer Modellierung konnte in ein und derselben Probe die räumliche Koexistenz von nanoskaligen Quantendrähten, Quantenpunkten und ausgedehnten Domänen einer ausschließlichen atomaren Registratur nachgewiesen und als Ursprung vielfältiger spektraler Charakteristiken von Exzitonen in $MoSe_2$-WSe_2 Heterostrukturen identifiziert werden. Das Wissen um mesoskopische Rekonstruktion erlaubt ein vereinheitlichendes Verständnis der exzitonischer Phänomene in Heterobilagen mit und ohne Moiré-Effekte.

Im letzten Teil der Arbeit werden schließlich Ergebnisse an $MoSe_2$-WSe_2 Heterostrukturen, die als vertikal geschichtete dreieckige Kristalle im CVD-Prozess entstehen, vorgestellt. Mittels optischer Spektroskopie und hochauflösender Transmissionselektronenmikroskopie konnten ausgedehnte Moiré-freie Bereiche energetisch begünstigter atomarer Registraturen in H- und R-artigen Schichtfolgen identifiziert werden, die von Korngrenzen und Moiré-artigen Domänen konkurrierender Registraturen benachbart werden. Beachtenswert ist dabei, dass Exzitonen der sogenannten $\mathrm{R}_{\mathrm{h}}^{\mathrm{M}}$ Registratur die Photolumineszenz von CVD-gewachsenen Heterobilagen überwiegend bestimmen, ganz im Gegensatz zur Dominanz von $\mathrm{R}_{\mathrm{h}}^{\mathrm{X}}$ Exzitonen in mechanisch aufgeschichteten $MoSe_2$-WSe_2 Heterostrukturen.

Im Gesamtbild gibt die Arbeit eine vereinheitlichende Perspektive auf vielfältige Charakteristika von Exzitonen in Halbleiter-Homobilagen und Heterostrukturen mit parallel und antiparallel ausgerichteter Schichtfolge. Die Ergebnisse tragen bei zu einem besseren Verständnis exzitonischer Phänomene, die wiederum entscheidend die optischen Eigenschaften von geschichteten van der Waals Systemen bedingen.

Abstract

Two-dimensional transition metal dichalcogenide (TMD) semiconductors exhibit unique optoelectronic properties. Rational assembly of individual monolayers into homobilayers or heterostructures provides versatile means for realizations of a wide range of novel quantum materials with tunable optical and transport phenomena based on unique spin-valley degrees of freedom and strong electron correlations. Monolayer crystals synthesized by chemical vapor deposition (CVD) serve as elementary building blocks of layered van der Waals systems with distinct properties determined by layer number, composition and orientation.

In the first part of this work, bilayers of WSe_2 were obtained with CVD synthesis in two contrasting crystal structures and studied with cryogenic optical spectroscopy. Control of CVD growth parameters resulted in high-quality large-area homobilayer stacks with contamination-free interfaces and strictly parallel and antiparallel alignment. Using complementary optical spectroscopy techniques at room and cryogenic temperatures, and employing theoretical calculations, we identified distinct signatures of momentum-direct excitons in optical absorption and momentum-indirect excitons in the photoluminescence of WSe_2 homobilayers with parallel and antiparallel crystallographic orientation. The study not only relates optical properties of homobilayers to crystal symmetry and stacking, it also highlights the role of crystal structure for the formation of hybrid interlayer exciton states.

In the second part, we report studies of $MoSe_2$-WSe_2 heterostructures built as stacks of separately grown monolayers. For such nearly-commensurate heterostacks, theory predicts atomic reconstruction of the rigid moiré lattice into periodic domains of nanoscale patterns. In finite-size samples of heterostacks, however, we found effects of lattice reconstruction on mesoscopic length scales, with direct consequences for local optical properties dictated by excitons. Using extensive optical spectroscopy studies, correlative secondary electron imaging of reconstructed domains, and theoretical modeling, we identified the coexistence of nanoscale quantum arrays, quantum wires, and extended domains of only one atomic registry in the same sample as the main source of the diverse spectral features reported for excitons in $MoSe_2$-WSe_2 heterostacks. This notion of mesoscopic reconstruction provides a unifying perspective on exciton phenomena in heterobilayers with and without moiré effects.

Abstract

Finally, the last part of the work presents the results on $MoSe_2$-WSe_2 heterostacks obtained as vertically stacked triangular crystals from CVD-synthesis. With combined studies by cryogenic optical spectroscopy and high-resolution transmission electron microscopy, we identified extended moiré-free domains of energetically favored $\mathrm{H}_{\mathrm{h}}^{\mathrm{h}}$ and $\mathrm{R}_{\mathrm{h}}^{\mathrm{M}}$ registries in H- and R-type stacks, in addition to grain boundaries of alternative registries and moiré-type cores. Remarkably, optical spectroscopy suggests that the $\mathrm{R}_{\mathrm{h}}^{\mathrm{M}}$ registry hosts the majority of exciton population with in-plane dipolar emission, as opposed to the predominance of $\mathrm{R}_{\mathrm{h}}^{\mathrm{X}}$ exciton features with out-of-plane luminescence in exfoliation-stacked $MoSe_2$-WSe_2 heterostructures.

Overall, the work provides a unifying perspective on diverse signatures of excitons in semiconductor homobilayers and heterobilayers in parallel and antiparallel alignment. The results contribute to improved understanding of exciton phenomena that dictate the optical properties of layered semiconductor van der Waals systems.

Contents

Chapter 1

Introduction

The family of two-dimensional (2D) materials has grown appreciably since the famous discovery of graphene in 2004 [1], experiments contradicted the theoretical prediction and showed that long-range-ordered 2D crystals do exist [2, 3]. Each new 2D material brings interest and excitement due to their uniuqe properties which their 3D counterparts do not exhibit [4–6]. Graphene is very popular because of its many fascination properties, but its lack of an electronic bandgap has stimulated the search for 2D materials with semiconducting character [5, 7, 8].

Semiconductor transition metal dichalcogenides (TMDs) provide a huge flexibility in tuning of their optoelectronic properties. Thus, band gap engineering can be done by changing the number of layers [9, 10]. Single atomic layer (ML) TMDs exhibits a unique combination of atomic-scale thickness, direct bandgap, strong spin-orbit coupling and favorable electronic and mechanical properties [11]. Combining monolayers to form multilayers allows to access new functionalities [12–14]. Besides single-layer TMDs, bilayer TMDs are a promising platform on which to exert unique control of excitonic states [15–22].

The optical properties of TMDs are governed by excitons in different spin, valley and layer configurations [23, 24]. Twisted layers of atomically thin 2D materials realize a broad range of novel quantum materials with engineered optical and transport phenomena arising from spin and valley degrees of freedom and strong electron correlations in hybridized interlayer bands. The natural 2H TMD homobilayers obtained from bulk crystals using mechanical exfoliation have been widely studied [25–28]. Furthermore, chemical vapor deposition (CVD) method and dry-transfer techniques realize the 3R stacking homobilayers (BLs). As the two adjacent layers are bound together by the weak van der Waals interaction, the interlayer coupling in $\pm K$ valleys can be largely suppressed by the giant spin-orbit splitting [28–32]. In contrast to absorption probing zero-momentum exciton transitions, the photoluminescence (PL) of BLs is dominated by momentum-indirect excitons [9, 33] via luminescence phonon sidebands [34–36], which exhibit linear energy shifts in perpendicular electric fields according to the Stark effect [37–40].

The most recent observation of two different slopes in the energy dispersion of phonon sideband emission from 2H WSe_2 BL in electric field [39, 40] indicates the presence of two degrees of electron-hole layer separation with respective dipole moments attributed to excitons in distinct QK and $Q\Gamma$ reservoirs [39, 40]. Experiments employing strain tuning [41] and magnetic field [35], on the other hand, suggest that the PL sidebands stem exclusively from QK excitons, indicating shortcomings in the present understanding of the underlying lowest-energy exciton reservoirs with finite center-of mass momenta [P1].

For the TMD heterobilayers (HBLs) formed by two different TMD materials such as typical type-II band alignment $MoSe_2$/WSe_2 HBLs, its conduction band and valence band edges are located in different layers, which results in the ultrafast interlayer charge transfer and interlayer excitons [42–44]. HBLs research represents a rapid development from the beginning interpretation of moiré superlattice [45–47] to recent reported lattice reconstruction [48–54, P2]. It has been widely demonstrated that a moiré pattern formed in a HBL with small lattice mismatch or twist angle or both [55–57]. Moiré effects give rise to a new class of quantum materials with rich transport and optical phenomena, including correlated electron physics in flat bands of bilayer graphene [58] and moiré excitons in semiconductor HBLs [59–61]. These phenomena arise from modulations of interlayer interactions on the nanoscale of spatially varying atomic registries of moiré supercells [62–64]. However, recent theoretical and experimental results show that lattices of marginally-twisted HBLs can transform from moiré to periodically reconstructed patterns with triangular tiling in R-type or hexagonal tiling in H-type HBLs due to finite elasticity [51, 52, 65, 66]. Thus, atomic reconstructions have shown significant impact on the reported optical properties and fundamentally improve our understanding of such systems [51, 54].

In our work, we expand the notion of nanoscale lattice reconstruction to the mesoscopic scale of extended samples and demonstrate rich consequences in optical studies of excitons in $MoSe_2$-WSe_2 HBLs with parallel and antiparallel alignment [P2]. Our results provide a unified perspective on diverse and partly controversial signatures of moiré excitons in semiconductor HBLs [19, 46, 47, 54, 67] by identifying domains with exciton properties of distinct effective dimensionality and establish mesoscopic reconstruction as a compelling feature of real samples and devices with inherent finite-size effects and disorder.

Overview

This thesis is structured as follows:

Starting with an overview of relevant physical properties such as crystal structure, phonons and the opto-electronic properties of transition metal dichalchogenides (TMDs), homobilayers (BLs) and heterobilayers (HBLs) in Chapter 2. Afterwards, we focus on stacking-dependent homobilayers of tungsten diselenide (WSe_2). Possible alignment shows the stacking of commensurate lattices, electronic band structure calculations theory, oscillator strength as well as Landé g-factors. Finally, we mainly expand ideal moiré superlattice to lattice reconstructions in ML stacked $MoSe_2$/WSe_2 HBLs along with corresponding optical selection rules.

Chapter 3 describes our CVD growth technique, involving principle, equipment and detailed grown parameters for each TMD. Sample fabrication process along with the confocal microscope for cryogenic spectroscopy are presented.

CVD grown two stable configurations of 2H and 3R stacking BLs WSe_2 were studied with cryogenic optical experiments and DFT theoretical calculations (Chapter 4). The results highlight the role of layer stacking for the spectral multiplicity of momentum-direct intralayer exciton transitions in absorption, and relate the multiplicity of phonon sidebands in the photoluminescence to momentum-indirect excitons with different spin valley and layer character.

Chapter 5 describes the spectra characteristic of reconstructed nanoscale quantum arrays, quantum wires and extended domains of just one atomic registry in one $MoSe_2$/WSe_2 HBL sample. The interpretation is supported and substantiated by theoretical calculations of interlayer excitons in all atomic registries of R- and H-type HBLs and modelling of their geometries in real samples. It also identifies novel features of exciton-polaron PL that dominate samples with large twist angles and non-reconstructed moiré patterns.

Chapter 6 presents cryogenic spectroscopy of CVD grown R- and H-type $MoSe_2$-WSe_2 HBLs. All the three atomic registries $\mathrm{R}_\mathrm{h}^\mathrm{h}$, $\mathrm{R}_\mathrm{h}^\mathrm{M}$ and $\mathrm{R}_\mathrm{h}^\mathrm{X}$ can be optically measured in R-type HBLs with $\mathrm{R}_\mathrm{h}^\mathrm{M}$ dominates among the registries.

Finally, Chapter 7 summarizes the experimental results and provides perspectives on subsequent research.

Chapter 2

Fundamental aspects of transition metal dichalcogenides

In this chapter, we give an overview of relevant physical properties of TMDs. Beginning with the parameters of MLs, such as crystal structure, phonons and the opto-electronic properties are summarized. Afterwards, we focus on the discussion of stacking-dependent properties in WSe_2 homobilayers, which consists of possible stacking orders of commensurate lattices, electronic band structure calculations theory, oscillator strength as well as Landé g-factors. Finally, we mainly discuss the properties in $MoSe_2$-WSe_2 HBLs made from stacked MLs and direct CVD growth. Aligned stackings of nearly commensurate lattices are shown along with ideal moiré superlattice and periodically reconstructed patterns.

2.1 Basics of monolayer crystals

Single atomic layers of TMDs are promising building blocks for developing fundamental science and applications. Combining monolayers (MLs) to form multilayers allows to access new functionalities and physical phenomena. Therefore, it is instructive to give a short review on the intrinsic properties of these single layer components.

2.1.1 Crystal structure and lattice vibrations

ML TMDs are atomically thin semiconductors of the type MX_2, with M a transition metal atom (Mo, W, etc.) and X a chalcogen atom (S, Se, or Te), possess a variety of polytypic structures such as 1H, 1T, and 1T′ phase [11, 68]. The most-studied 1H structure is a sandwich of covalently bonded three planes of two-dimensional (2D) hexagonally packed atoms in the trigonal prismatic structure as shown in Figure 2.1a. This lattice structure has out-of-plane mirror symmetry and broken in-plane inversion symmetry [69]. The discovery of graphene shows how new physical properties

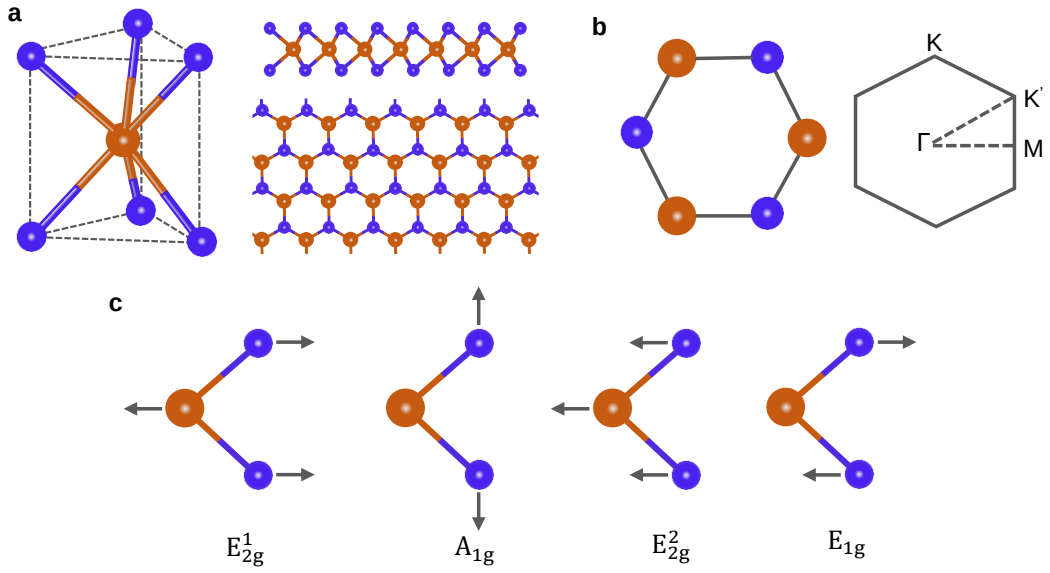

Figure 2.1: a, Crystal structure of ML TMDs. Trigonal prismatic structure of ML TMDs (left panel). Side and top view of a single layer (right panel). The transition metal atoms (M) are shown in red, and chalcogen atoms (X) in blue. **b**, The honeycomb lattice structure (left) and the first Brillouin zone with high-symmetry points (right). **c**, Schematics showing the atomic displacement of the four Raman active modes in ML WSe_2.

emerge when a bulk crystal of macroscopic dimensions is thinned down to one atomic layer. Like graphite, bulk TMDs materials are formed of monolayers bound to each other by van der Waals interaction, and can subsequently be peeled apart to achieve a single layer [70]. The utilization of mechanically exfoliated samples has rapidly led to abundant insights into fundamental properties of these MLs [71, 72]. Further implementation into technological applications requires a reliable method to reproducibly obtain homogenous, high-quality, thickness-controlled, and large-scale samples. Many avenues have been studied to address this issue, including synthesis via atomic layer deposition (ALD) [73], molecular beam epitaxy (MBE) [74], and chemical vapor deposition (CVD) [75].

Compared with bulk TMDs that are characterized by the D_{6h} point symmetry group for stoichiometric compounds, ML TMDs are described by lower symmetry D_{3h} point group due to broken inversion symmetry [76, 77]. The honeycomb lattice structure leads to a hexagonal Brillouin zone in reciprocal space shown in Figure 2.1b. Here, the valence band maximum (VBM) and conduction band minimum (CBM) are located at the inequivalent symmetry K points (K^+ and K^-) of

the first Brillouin zone. In addition to that, charge carriers residing in Γ and Q exhibit non-negligible contributions, making them relevant for the following considerations.

In the context of the crystal structure, it is instructive to discuss lattice vibrations induced by small displacements of the individual atoms. Here, we mainly focus on the material WSe_2, which is most relevant for the subsequent experiments. Lattice vibrations can be classified based on the irreducible presentation of the symmetry group of the crystals [78]. The crystal structure of WSe_2 belongs to the D_{6h} point group. There are 18 lattice dynamical modes (3 acoustic and 15 optical modes) at the center of the Brillouin zone (Γ point) [79, 80]. The zone center phonons can be irreducibly represented as follows [80]: $\Gamma = A_{1g} + 2A_{2u} + B_{1u} + 2B_{2g} + E_{1g} + 2E_{1u} + E_{2u} + 2E_{2g}$, where one A_{2u} and one E_{1u} are acoustic modes, A_{1g}, E_{1g} and E_{2g} are Raman active, another A_{2u} and E_{1u} are infrared active, and B_{2g}, B_{1u} and E_{2u} are optically inactive. The atomic displacement of the four Raman active modes A_{1g}, E_{1g}, E^1_{2g} and E^2_{2g} of ML WSe_2 is shown in Figure 2.1c. The A_{1g} mode is an out-of-plane vibration only relating to the X atoms while the E^1_{2g} mode an in-plane displacement involving both M and X atoms [80, 81]. The E^2_{2g} mode is a shear mode and corresponds to the vibration of two rigid layers relative to each other at very low frequencies (< 50 cm^{-1}) [80]. The E_{1g} mode, which is forbidden in the back scattering Raman configuration, is an in-plane vibration of X atoms only. In particular, ML WSe_2 belongs to the D_{3h} point group and has 9 normal vibrational modes at the Brillouin zone center [78]. The rigid layer shear mode E^2_{2g} is absent. Lattice vibrations are different in ML and multilayer TMDs. Raman spectroscopy is one of the tools that measures the lattice vibrations of TMDs and therefore can be used to define layer numbers, interlayer coupling and layer-stacking configurations [78, 80, 82, 83].

2.1.2 Optoelectronic properties

Most relevant MX_2 undergo an indirect-to-direct optical gap transition from bulk to the ML regime. In bulk TMDs, the indirect-gap transition corresponding to the CBM in Γ point at the center of the first Brillouin zone and VBM in Q point situated nearly halfway along Γ-K direction [84, 85]. In the ML limit, the gap turns into direct and the band extrema are located at the inequivalent K points (K^+ and K^-) due to the broken parity symmetry as shown in Figure 2.2a, and resulting in much stronger light emission [77]. At these extrema, the main contribution to VB and CB stems from d orbitals of the transition metal atoms imposing a strong spin orbit coupling [86]. This spin orbit coupling eliminates the spins degeneracy in both the CB and VB,

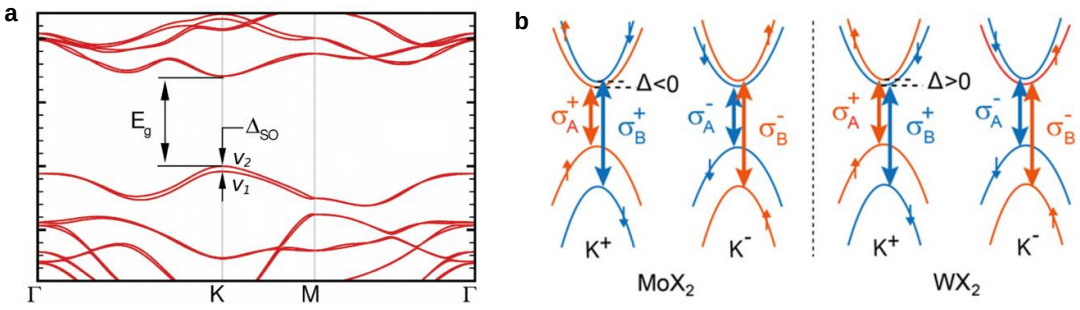

Figure 2.2: a, Typical band structure for MX_2 MLs using density functional theory. **b**, Spin splittings and optical selection rules in MoX_2 and WX_2 MLs. Graphics a and b are reproduced from Ref. [90].

introduces a strong energy splitting between spin up and down states. Together with the broken inversion symmetry, this leads to coupled spin and valley physics in those TMD MLs [87]. In general, the spin splitting in CB is a few to tens of meV and the spin orbit splitting in the VB is several hundred meV [88], allowing control of the electron spin by tuning the excitation laser photon energy [89].

Interestingly, depending on the metal atom (Mo or W), the spin splitting of CB has a different sign and results in an energy separation between the spin-allowed and optically active (bright) transitions and the spin-forbidden and optically inactive transitions (dark) [91], which are indicated in Figure 2.2b. The lowest-energy transition in MoX_2 is expected to be the bright exciton, however, dark excitons in WX_2 materials are predicted to be at lower energies than the bright ones [92, 93]. In addition to spin-orbital splitting, the optical transitions at the gap are also valley selective as σ^+ and σ^- circularly polarized light can couple only to the transition at the K^+ and K^- valleys, respectively [70]. Due to these two properties (spin-valley splitting and optical selection rules), laser photon with specific polarization and energy allows initialization of electronic valley states (K^+ or K^-) and spin states (up or down) [94].

2.2 Properties of WSe_2 homobilayer

THIS SECTION IS PARTLY BASED ON THE PUBLICATION [P1]
Li, Z., Förste, J., Watanabe, K., Taniguchi, T., Urbaszek, B., Baimuratov, A. S., Gerber, I. C., Högele, A. & Bilgin, I. Stacking-dependent exciton multiplicity in WSe_2 bilayers. *Phys. Rev. B* **106,** 045411 (2022)

Homobilayer MX_2, consisting of out-of-plane bonding MLs, is the first TMDs multilayer system involving weak van der Waals interactions. However, these interlayer interactions are strong enough to alter the stacking geometry and modify the measured properties of TMD BLs significantly. Based on the preceding overview of ML physics, we mainly investigate properties of BL WSe_2 in the following sections.

2.2.1 Stacking types of commensurate lattices in homobilayers

Combining ML TMDs into a "lego" building-block fashion with twist angles provides numerous possibilities in tuning the optoelectronic properties of BLs [95, 96]. In homobilayer systems, featuring equal lattice constants by default, there are five possible high-symmetry stacking orders [96, 97], which can be grouped into two stacking geometries H and R. The two layers exhibit a 60° twist angle for H-type stacking, while for R-type stacking, the in-plane crystalline axes of the two layers are along the same direction with a 0° twist angle. These two atomic geometries are depicted in Figure 2.3. We distinguish the two layers by color coding and show the positions of W and Se atoms indicated by large and small spheres, respectively. Vertical dashed lines help identify the individual stacking. The labeling scheme rules for homobilayer WSe_2 are based on hexagonal boron nitride (hBN) [98, 99] and TMD homobilayers and heterostructures [96, 97]. The starting layer is labeled with a capital letter A and subsequent layers are labeled with capital letters A or B, depending on their arrangement and resulting in the following five stacking orders: (i) AA or $\mathrm{R}_\mathrm{h}^\mathrm{h}$ (point group D_{3h}), eclipsed stacking with W over W and Se over Se; (ii) AA' or $\mathrm{H}_\mathrm{h}^\mathrm{h}$ (point group D_{3d}), eclipsed stacking with W over Se, characteristic of the 2H phase; (iii) A'B or $\mathrm{H}_\mathrm{h}^\mathrm{M}$ (point group D_{3d}), staggered stacking with Se over Se; (iv) AB or $\mathrm{H}_\mathrm{h}^\mathrm{X}$ (point group C_{3v}), staggered stacking with Se over W; (v) AB' or $\mathrm{R}_\mathrm{h}^\mathrm{X}$ (or $\mathrm{R}_\mathrm{h}^\mathrm{M}$) (point group D_{3d}), staggered stacking with W over W, characteristic of the 3R phase [96, 97]. The similar labeling rules were applied to heterostacks in Section 2.3.1.

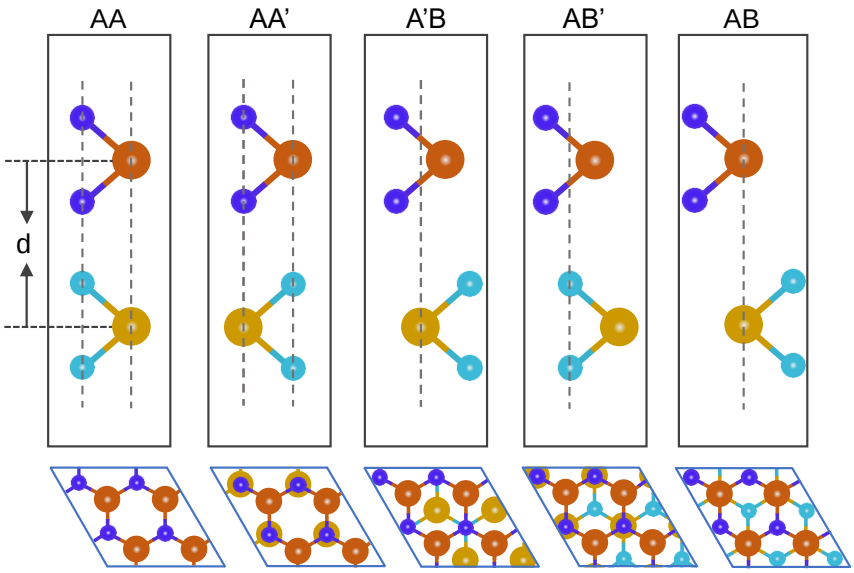

Figure 2.3: High-symmetry stacking orders of R- and H-type homobilayer WSe_2 shown from side (top panel) and top (bottom panel) views. Large and small spheres represent Tungsten and Selenium atoms, respectively. We follow the nomenclature proposed in Ref. [96]. A gray-scale (color coding) is used to distinguish the position of the atoms in the two WSe_2 layers. The full lines demarcate the unit cell.

He, et al. [96] calculated the energies of the geometrical structures and found that AA' is the most stable stacking pattern in H-type geometry and AB' is the most stable in R-type stacking geometry [96], which means that they are optically favorable. Early experimental works largely investigated the natural 2H stacking order based on the reliance of mechanically exfoliating WSe_2 [38–40, 100]. While recent advances in chemical synthesis and sequential stacking processes open the doors to investigations of 3R stacked bilayers and twisted bilayer systems. Having established the most stable structures, the electronic and optical properties of the two most stable phases AA' (2H) and AB' (3R) are discussed in the following section.

2.2.2 Electronic band structure, oscillator strength and exciton Landé g-factors

As already mentioned above in the ML electronic band structure section, MX_2 undergo a direct-to-indirect gap crossover in the BL as well as multilayer systems. In contrast to direct gap ML MX_2 with band edges coinciding at the K point, the

number and locations of CB and VB extrema in BL MX_2 are distinct which depend on the TMD compositions and atomic stacking orders [96]. In BL TMDs, the band structures include the location of the CBM that is found at point Q for all stackings, and the different relative position of the VBM which is situated at either Γ or K depending on the TMDs materials [13, 25, 34, P1, 50, 96]. In MoS_2 and WS_2 the VBM is at Γ, but in $MoSe_2$ and WSe_2 the VBM shifts to K [25, 34, 50, 96]. In the specific case of BL WSe_2 crystals, the CBM is located at Q, while the VBM at K exceeds the one at Γ only by 40 $\pm$ 30 meV [34, 101] resulting in indirect band gap transitions [28]. To get an insight into the actual band structures and further analyze the optical properties of WSe_2, we carried out band structure calculations including excitonic effects via the density functional theory (DFT) + GW approach in collaboration with the Toulouse group. The following paragraph summarizes the most important input parameters in our DFT approach.

Our first-principle calculations were performed with the PBE exchange correlation functional [102, 103] as implemented in the Vienna ab initio simulation package (VASP) [25, 104], where the electron and ion interaction is described within the projector-augmented wave method [105]. The optimized lattice parameter 3.28 Å of WSe_2 [96] was used for all the calculations. Motivated by the fact that 2H and 3R bilayers have very similar lattice parameters and no significant change in the interlayer distance, defined by the separation between the two parallel planes containing W atoms, is observed 6.50 and 6.54 Å respectively [96]. A grid of $15 \times 15 \times 1$ k points was used, in conjunction with a vacuum height of 21.9 Å in order to minimize interactions between periodic images [25, 106]. An energy cutoff of 400 eV and a Gaussian smearing of 0.05 eV width were chosen for partial occupancies [91, 106–108], when a tight electronic minimization tolerance of 10^{-8} eV is set to determine with good precision the corresponding derivative of the orbitals with respect to k needed in quasiparticle band structure calculations [25, 96]. Figure 2.4a and b show the calculated band structures for 2H and 3R stacking, respectively. In both structures, the CBM is located at Q while the VBM at K in consistent with literatures [14, 34, 96], suggesting an indirect band gap for the two atomic registries. Due to the different atomic registries for top and bottom layers in 3R stacking, the band structure for these two layers is distinct, with different transition energies at the K point. This is in stark contrast to 2H stackings, where both layers, and their associate intralayer states, are energetically degenerate [14, P1].

Apart from the effect of the stacking pattern on the band structure, we investigate the effects of stacking orders on the optical absorption and oscillator strength by

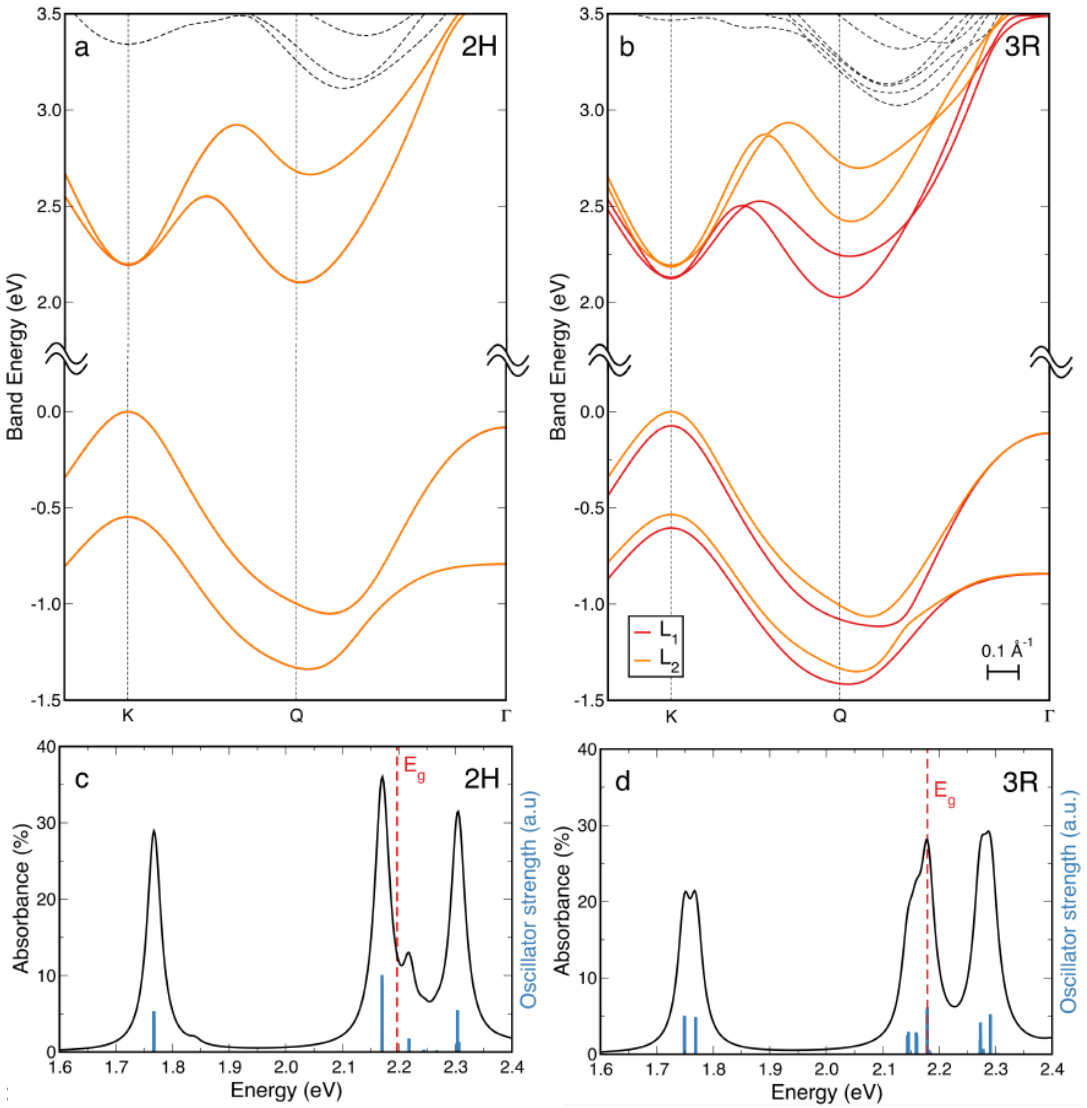

Figure 2.4: Theoretical calculations for 2H and 3R WSe_2 homobilayers. **a** and **b**, Band structure for 2H and 3R WSe_2 homobilayers, respectively. Red and orange colors represent the bottom and top layer, L_1 and L_2. **c** and **d**, Absorption spectra (black) and oscillator strength (blue) for 2H and 3R stacking, respectively, calculated with the GW + BSE method. The red dashed lines indicate the energy gap E_g.

solving BSE shown in Figure 2.4c and d. The main characteristics for the 2H stacking are (i) we find only one transition at about 1.75 eV, which corresponds to the A-exciton and (ii) the feature at 1.85 eV with very low oscillator strength is the interlayer KK exciton with a much lower oscillator strength here than in BL MoS_2 and $MoSe_2$ due to the larger spin orbit coupling in WSe_2 [12, 29, 109, 110]. While for

3R stacking, (i) there are two transitions around 1.75 eV separated by about 20 meV which correspond to A-excitons in the top and bottom layer. Note that a similar lifting of the intralayer exciton degeneracy was anticipated for 3R MoS_2 BLs [12]. (ii) The interlayer exciton feature is completely absent as hybridization of electronic states at the K-point is forbidden by symmetry [29]. In both 2H and 3R stackings, lower-energy momentum-indirect transitions that dominate BL luminescence [111] via phonon-assisted emission are not captured by our absorbance calculation due to the vanishingly small oscillator strength which reflects exciton-photon momentum mismatch in direct dipolar transitions [P1].

In addition to determining the nature of the electronic band structure, DFT can also be used to calculate exciton g-factors [112]. The results of calculated excitonic transitions of BL WSe_2 are presented in Chapter 4. Here, we focus on the derivation of the exciton g-factors from the conducted DFT calculations according to Reference [35, 45, 113].

The starting point is a nonrelativistic band structure Hamiltonian H^0 and its corresponding band energies $\varepsilon^0_{\mathrm{nk}}$ and Bloch state $|n\mathbf{k}\rangle$ [113, 114]

$$H^0 = \frac{\mathbf{p}^2}{2m_0} + V \tag{2.1}$$

$$H^0|n\mathbf{k}\rangle = \varepsilon^0_{n\mathbf{k}}|n\mathbf{k}\rangle \tag{2.2}$$

$$\mathbf{1} = \sum_n |n\mathbf{k}\rangle\langle n\mathbf{k}| \tag{2.3}$$

$\mathbf{p}$ is the momentum operator, m_0 is the electron net mass, V is the effective potential, n and $\mathbf{k}$ are the band number and wave vector [113, 115]. The coupling of these Bloch states to an external magnetic field is described by adding the spin Zeeman term to H^0 and by replacing the momentum operator $\mathbf{p}$ by $\mathbf{p} - \mathrm{q}\mathbf{A}$ (minimal coupling), where $\mathbf{A}$ is the vector potential, $\mathrm{q} = -|e_0|$ the negative electron charge and e_0 is the elementary charge [113, 116, 117]. For a uniform external magnetic field $\mathbf{B}$ it is convenient to choose $\mathbf{A} = (\mathbf{B} \times \mathbf{r})/2$, which satisfies the Coulomb gauge $\nabla \cdot \mathbf{A} = 0$, where $\mathbf{r}$ is the position operator. This leads to the Pauli equation [116–118]

$$H(\mathbf{B}) = H^0 + H^{\mathrm{L}}(\mathbf{B}) + H^{\mathrm{Q}}(\mathbf{B}) = H^0 + \mu_{\mathrm{B}}\mathbf{B} \cdot \left(\mathbf{L} + \frac{g_0}{2}\mathbf{\Sigma}\right) + \frac{e_0^2}{8m_0}(\mathbf{B} \times \mathbf{r})^2 \tag{2.4}$$

where $\mu_B = \hbar e_0/2m_0$ is the Bohr magneton, $\mathbf{L} = (\mathbf{r} \times \mathbf{p})/\hbar$ is the angular momentum operator, $\mathbf{\Sigma} = (\mathbf{\Sigma}^x, \mathbf{\Sigma}^y, \mathbf{\Sigma}^z)$ is the vector of Pauli matrices, and g_0 is the g-factor of the free electron. $H(\mathbf{B})$ in Equation 2.4 is separated into $H^{\mathrm{L}}(\mathbf{B})$ and $H^{\mathrm{Q}}(\mathbf{B})$ that are linearly and quadratically dependent on $\mathbf{B}$ [113, 116, 118, 119], respectively.

It is well known that $H^{\mathrm{L}}(\mathbf{B})$ and $H^{\mathrm{Q}}(\mathbf{B})$ are weak perturbations of the H^0 and the magnetic field shift of the band energies can be evaluated with first-order perturbation theory giving $\varepsilon_{n\mathbf{k}}(\mathbf{B}) = \varepsilon^0_{n\mathbf{k}} + \langle n\mathbf{k}|H^{\mathrm{L}}(\mathbf{B}) + H^{\mathrm{Q}}(\mathbf{B})|n\mathbf{k}\rangle$ [113, 120]. Choosing $\mathbf{B} = (0, 0, \mathbf{B})$ parallel to the Cartesian z-direction and $g_0/2 \sim 1$ and obtaining $\varepsilon_{n\mathbf{k}}(\mathbf{B}) = \varepsilon^0_{n\mathbf{k}} + \mu_B\mathbf{B}(L_{n\mathbf{k}} + \mathbf{\Sigma}_{n\mathbf{k}}) + H^{\mathrm{Q}}_{n\mathbf{k}}$, with the matrix elements $\mathrm{L}_{n\mathbf{k}} = \langle n\mathbf{k}|\mathrm{L}^z|n\mathbf{k}\rangle$, $\mathbf{\Sigma}_{n\mathbf{k}} = \langle n\mathbf{k}|\mathbf{\Sigma}^z|n\mathbf{k}\rangle$ and $H^{\mathrm{Q}}_{n\mathbf{k}} = e_0^2\mathbf{B}^2/8m_0\langle n\mathbf{k}|(r^x)^2 + (r^y)^2|n\mathbf{k}\rangle$. The effective g-factor of the Bloch state $|n\mathbf{k}\rangle$ is thus $g_{n\mathbf{k}} = L_{n\mathbf{k}} + \mathbf{\Sigma}_{n\mathbf{k}}$ [113, 121–123].

The exciton is formed by Coulomb correlations between an occupied state in the CB with the wave vector $\mathbf{k}_c$ and spin z-projection s_c and an empty state in the VB with the wave vector $\mathbf{k}_v$ and spin z-projection s_v. In this spin-valley configuration, the exciton g-factor is given by [35, 112]

$$g^{(cv)}(\mathbf{k}_c, \mathbf{k}_v) = g_c(\mathbf{k}_c) - g_v(\mathbf{k}_v), \tag{2.5}$$

where the g-factor of the electron in band $n = c, v$ is

$$g_n(\mathbf{k}) = g_0 s_n + 2L_n(\mathbf{k}). \tag{2.6}$$

$g_0 = 2$ is the free electron Landé factor, and the z-component of the orbital angular momentum [124–127] is

$$L_n(\mathbf{k}) = \frac{2m_0}{\hbar^2} \sum_{m\neq n} \mathrm{Im}\left[\xi^{(x)}_{nm}(\mathbf{k})\xi^{(y)}_{mn}\mathbf{k}\right](E_{n\mathbf{k}} - E_{m\mathbf{k}}). \tag{2.7}$$

where $\boldsymbol{\xi}_{nm}(\mathbf{k}) = i\langle u_{n\mathbf{k}}|\,\partial/\partial\mathbf{k}\,|u_{m\mathbf{k}}\rangle$ is the interband matrix element of the coordinate operator [128]. $E_{n\mathbf{k}}$ and $u_{n\mathbf{k}}$ are the energy and periodic Bloch amplitude of the electron in band n with wave vector $\mathbf{k}$. Using the energy band structure and interband matrix elements of the coordinate operator obtained from DFT we calculated the g-factor for intra- and interlayer excitons in Chapter 4 and Chapter 5.

2.3 Properties of $MoSe_2$-WSe_2 heterostructures

THIS SECTION IS PARTLY BASED ON THE MANUSCRIPT [P2]
Zhao, S., Li, Z., Huang, X., Rupp, A., Göser, J., Vovk, I., Kruchinin, S., Watanabe, K., Taniguchi, T., Bilgin, I., Baimuratov, A. & Högele, A. Excitons in mesoscopically reconstructed moiré hetersotructures. *arXiv preprint.* arXiv: `2202.11139` (2022)

As the research field of layered quantum materials is moving forward, van der Waals assemblies of 2D semiconducting TMDs become increasingly significant. They are

known to exhibit rich transport and optical phenomena, including correlated electron physics and moiré excitons arising from modulations in layer hybridization on the nanoscale of spatially varying atomic registries. In the subsequent section, we investigate moiré excitons in laterally extended, marginally-twisted $MoSe_2$-WSe_2 HBLs subject to mesoscopic lattice reconstruction.

2.3.1 Ideal moiré superlattice and atomic reconstruction

In ideal case, for TMD HBLs with a small lattice mismatch and/or rotational misalignment, a moiré pattern could be realized naturally with periodic changes in the interlayer atomic registry [64, 129]. The corresponding moiré period varying from several nanometers to tens of nanometers given by $b \approx a/\sqrt{\delta^2 + \theta^2}$, where a is the ML lattice constant, δ is the lattice mismatch, and θ is the relative twist angle [60, 130]. Upon lateral translation through a moiré supercell, each stacking modulates through points of highly symmetric atomic registries ($\mathrm{R}_\mathrm{h}^\mathrm{h}$, $\mathrm{R}_\mathrm{h}^\mathrm{M}$, $\mathrm{R}_\mathrm{h}^\mathrm{X}$ and $\mathrm{H}_\mathrm{h}^\mathrm{h}$, $\mathrm{H}_\mathrm{h}^\mathrm{M}$, $\mathrm{H}_\mathrm{h}^\mathrm{X}$, X: Chalcogen site, M: metal site, and h: hollow center of the hexagon) [53, P2, 60, 131–133] shown schematically in Figure 2.5a for a vertical heterostack of top MX_2 and bottom M'X'$_2$ MLs. $\mathrm{R}_\mathrm{h}^\mathrm{u}$ ($\mathrm{H}_\mathrm{h}^\mathrm{u}$, $u = X, M, h$) means that the u site of the electron layer overlaps vertically with the h site of the hole layer [45, 47, 60].

It is significant to make a clear distinction of the two types of HBLs: near-commensurate and incommensurate HBLs, which depend on whether the chacogen atoms are the same in two layers [134–136]. In near-commensurate HBLs (similar lattice constants) consisting of two TMD MLs that share the same chalcogen atoms, leading to a large range of possible moiré supercell sizes ($\sim 1 - 100$ nm) or decreased supercell densities ($\mathrm{n_{moiré}}$) [96, 137, 138], as shown in the top panel of Figure 2.5b. By contrast, in incommensurate HBLs (substantially different lattice constants) building of two TMD MLs with different chalcogen atoms (for example, MoS_2/WSe_2). The largest possible moiré supercell is ~ 8 nm laterally (bottom panel of Figure 2.5b) [136, 139–141]. Therefore, the distinct tunable range of the moiré supercell size and density in incommensurate and near-commensurate HBLs, leading to different twist-angle-dependent optical properties [134, 136, 142, 143].

Previous work shown that control of the twist angle between layers could have a dramatic effect on HBLs properties, and all of these reports assume that the lattices of the individual layers remain rigid [47, 59, 61, 144, 145]. However, recent theoretical and experimental work on TMDs bilayers indicate that atomic reconstruction, which is rearrangement of atoms within the individual layers, can occur for small twist

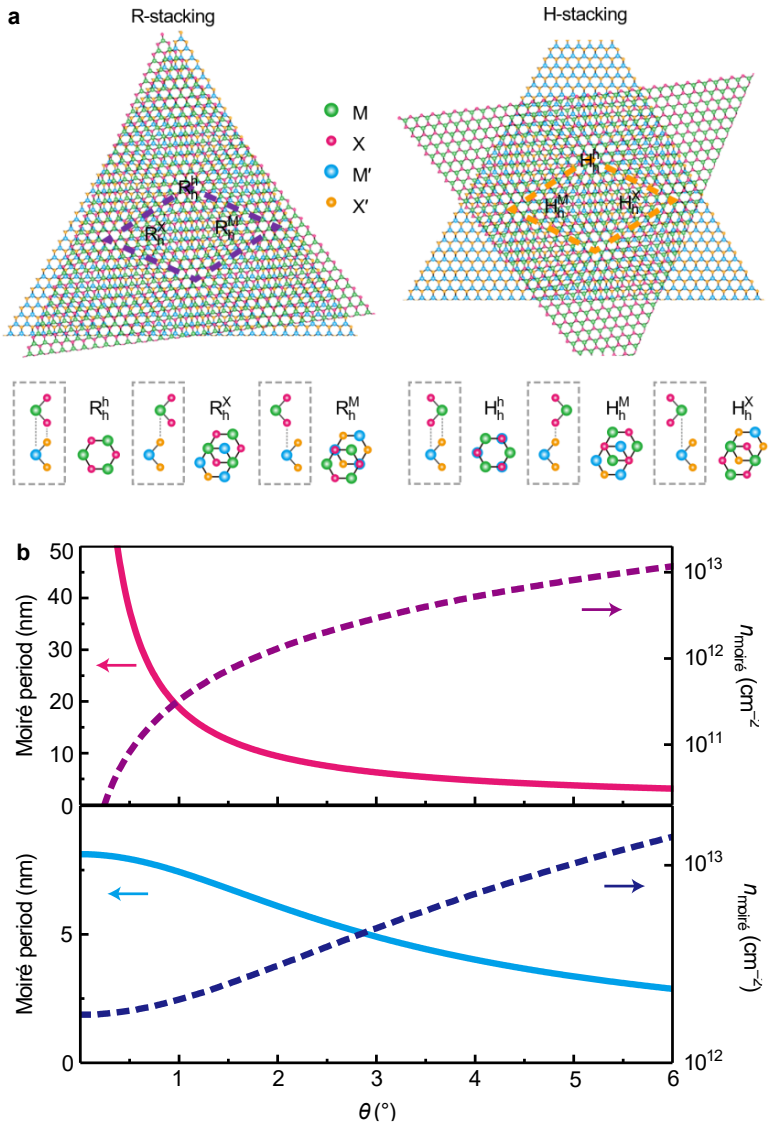

Figure 2.5: a, Schematics of moiré superlattice in marginally twisted R- and H-type HBLs. In both cases, the HBL consists of the electron located layer MX_2 and hole located layer $M'X'_2$, with the M, X, M', and X' atoms in green, magenta, blue and gold colors, respectively. The moiré pattern unit cells of R- and H-type stackings are indicated by purple and orange dashed diamond shapes. **b**, The moiré period and density of the moiré supercells (the number of moiré supercells per square centimetre) as a function of the twist angle in near-commensurate HBL (top panel; for example, $MoSe_2/WSe_2$) and incommensurate HBL (bottom panel; for example, $WS_2/MoSe_2$) with near-R-stacking. Solid (dashed) lines indicate the moiré period (density of the moiré supercells). θ is the twist angle between the top and bottom layers in the HBL. Graphics **a** and **b** are reproduced from Ref. [134].

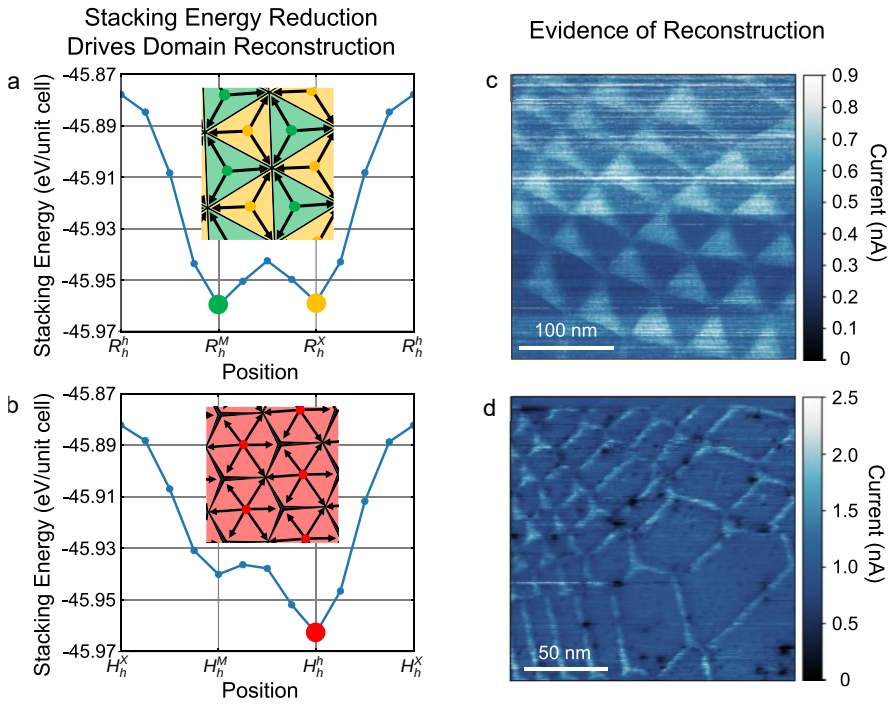

Figure 2.6: **a**, Interlayer stacking energy as a function of stacking orientation along the three high-symmetry points of rigid moiré patterns. R_h^M and R_h^X structures are degenerate global minima, which suggests that the structure will reconstruct in order to maximize the area of R_h^M and R_h^X domains. A diagram indicating the shape of the expected R_h^M and R_h^X domain expansion is shown in the inset. **b**, Interlayer stacking energy as a function of stacking orientation along the three high-symmetry points of rigid moiré patterns. H_h^h structure is the global minimum, which suggests that the structure will reconstruct in order to maximize the area of the H_h^h domains. A diagram indicating the shape of the expected H_h^h domain expansion is shown in the inset. **c** and **d**, Experimental results of the atomic reconstruction in $MoSe_2$/WSe_2 R- and H-type stacking HBLs. Graphics **a**-**d** are reproduced from Ref. [51].

angles [13, 14, 50, 51]. Driven by competition between intralayer strain and interlayer adhesion energy, energetically favored atomic registries expand at the expense of unfavorable registries into periodic domains with areas inversely proportional to the twist angle θ [P2].

Figure 2.6 shows the theoretically calculated stacking energy as a function of position along the three high-symmetry points in one moiré supercell and the evidence of atomic reconstruction from experiments of near-commensurate R- and H-type stackings. In R-type structure there are two degenerate low-energy stacking

arrangements: R_h^M and R_h^X in Figure 2.6a [51]. This spatial variation in stacking energy causes a driving force for atomic reconstruction such that the R_h^M and R_h^X domains expand in order to decrease the overall stacking energy, as depicted in the inset of Figure 2.6a. The R_h^M and R_h^X domains are anticipated to be triangular since each R_h^M domain has three nearest neighbor R_h^X points (and vice versa) [14, 50, 51, 53, 65, 146, 147]. In contrast with the R-type case, the H-type structure exhibits a single low-energy stacking arrangement: H_h^h in Figure 2.6b and this low energy stacking arrangement again provides a driving force for atomic reconstruction but there will only be one domain type [50, 51, 65, 148], as depicted in the inset of Figure 2.6b. The H_h^h domain will be hexagonal since each H_h^h point is surrounded by six nearest H_h^h points [49, 149]. Experimental proof of the significant atomic reconstruction in $MoSe_2$/WSe_2 HBLs at small twist angles ($\delta \leq 1°$) shown in Figure 2.6c and d, exhibiting significant departure from the patterns anticipated from a simple rigid-lattice moiré model (Figure 2.5a) [51].

It is important to note that a moiré superlattice is not certainly formed within a vertical stacking of two MLs [47]. The simplification of near-commensurate lattices is valid for CVD grown $MoSe_2$/WSe_2 HBLs since the lattice mismatch between two adjacent atomic layers is only 0.1% as calculated using $\delta = 1 - a_{M'X'_2}/a_{MX_2}$, with a_{MX_2} being the corresponding lattice constant of MX_2 (M=Mo, W, and X=Se). Such a minor lattice distortion results in a long-range stacking order without a moiré pattern [18, 150].

2.3.2 Optical properties of reconstructed domains

After analyzing the reconstruction domains and energetically favorable atomic-stacking orders, it is instructive to investigate the optical properties of reconstruction domains following Ref. [97, 112]. We start with optical selection rules at K points, which can be deduced from symmetry analysis of the individual atomic registries [151]. Identifying the individual stacking symmetry is the basic step for the purpose of describing the electron Bloch functions at K^+ and K^- with the corresponding irreducible representations Γ_n ($n = 1, ..., 6$) given in the Koster notation [152]. The Bloch amplitudes then can be recast as spinor representations (Γ_4, Γ_5, Γ_6) for the WSe_2 VB and $MoSe_2$ two spin-split CBs combining with spin parts. In the last step, using $\Gamma_c \times \Gamma_v^*$ (the star denotes the time-reversed representation of the corresponding symmetry group), where Γ_c (Γ_v) is the irreducible representation of the CB (VB), three possible optical transitions σ^+, σ^- and z-polarized light are derived [153]. The spinor representations and optical selection rules for all stacking orders in R- and

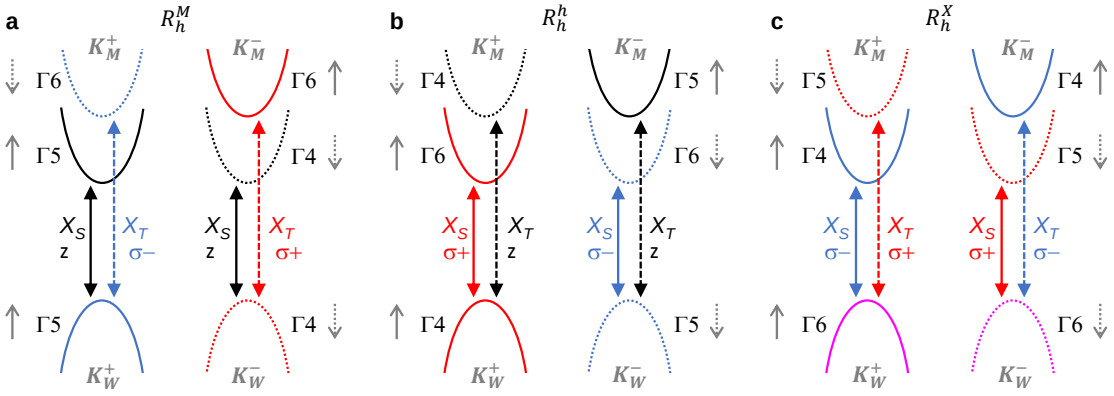

Figure 2.7: Band symmetries and optical selection rules for R-type heterostack. **a**, $MoSe_2$ CB and WSe_2 VB at K^+ and K^- forming the single-particle band diagram of a near-commensurate HBL in $\mathrm{R_h^M}$ atomic registry including band symmetries (Γ_4, Γ_5 and Γ_6 are the spinor representations) and dipolar transitions with σ^+ (red), σ^- (blue) and z (black) polarization. **b** and **c**, Same for respective $\mathrm{R_h^h}$ and $\mathrm{R_h^X}$ atomic registries. Solid (dotted) bands represent spin up (down) electron polarization; solid (dashed) arrows represent spin-allowed (spin-forbidden) optical transitions. The energy bands are colored according to the polarization of the respective optical transitions except for the bands in magenta supporting both σ^+ and σ^- transitions. Graphics **a**-**c** are reproduced from Ref. [151].

H-type HBLs are summarized in Figure 2.7 and Figure 2.8.

In R-type stacked HBLs, the $\mathrm{K_W^+}$ ($\mathrm{K_W^-}$) and $\mathrm{K_M^+}$ ($\mathrm{K_M^-}$) valleys of WSe_2 VB and $MoSe_2$ CBs are at the same position in reciprocal space. While in H-type HBLs, the situation changes due to the $\pi/3$-rotation of the $MoSe_2$ layer relative to the WSe_2 layer [21, 97, 134, 154, 155]. Brillouin zones are also rotated by $\pi/3$ resulting in K^+ and K^- valleys residing on top of each other [28, 97, 155]. Zero-momentum interlayer excitons can be formed by an unoccupied VB state together with two possible CB states leading to singlet IX_S and triplet IX_T excitons with different energetic ordering in the two stackings resulting from the $\pi/3$ rotation [28, 46, 156].

In the last, we use DFT to calculate exciton g-factors and oscillator strengths of interlayer excitons in R- and H-type $MoSe_2$-WSe_2 HBLs as described in detail in Section 2.2.2 and Ref. [35, 45]. In brief, DFT calculations were performed with the PBEsol exchange-correlation functional [103] as implemented in the Vienna ab- initio simulation package (VASP) [157]. Van der Waals interactions were included with the DFT-D_3 method [105] and Becke-Johnson damping [158]. Moreover, spin-orbit

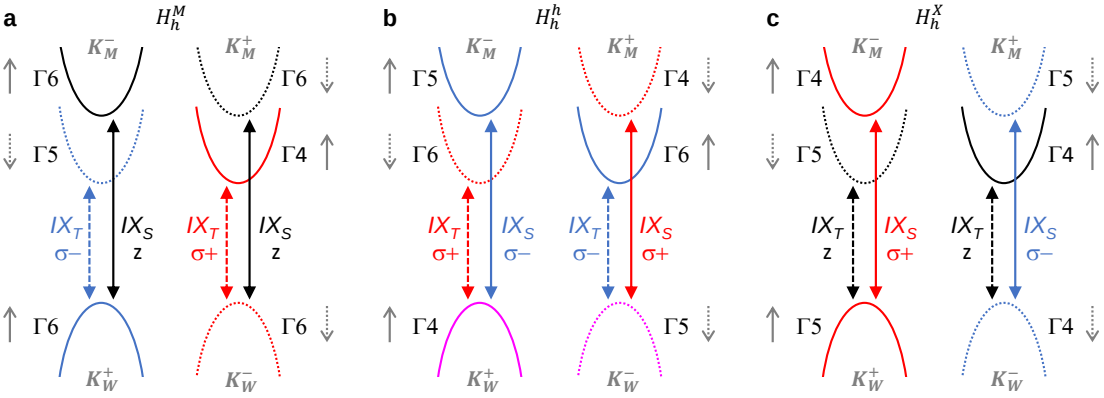

Figure 2.8: Band symmetries and optical selection rules for H-type stacking. The three panels display the relevant properties for H_h^M (**a**), H_h^h (**b**) and H_h^X (**c**) stacking order. Graphics **a**-**c** are reproduced from Ref. [151].

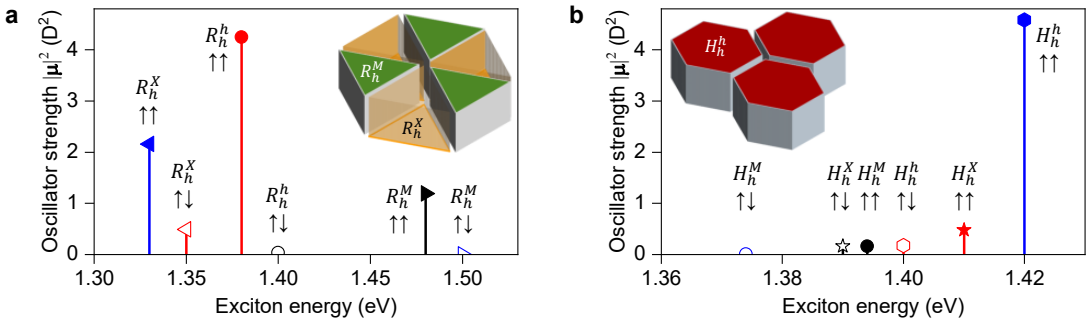

Figure 2.9: a and **b**, Oscillator strengths of interlayer excitons in R- and H-type $MoSe_2$-WSe_2 HBLs. The dipolar selection rules are represented by colors (red: σ^+; blue: σ^-; black: z-polarized in-plane emission), filled and empty symbols indicate the corresponding singlet and triplet exciton states. The inset schematics show the energy landscape in the presence of periodic reconstruction, with excitons in triangular R_h^X domains confined by the poential walls of R_h^M domains, and hexagonal H_h^h domains with highest-energy excitons.

interactions were included at all stages. Elementary cells with thickness of 35 Å in the z-direction were used to minimize the interactions between periodic images. The atomic positions were relaxed with a cutoff energy of 400 eV until the total energy change was less than 10^{-6} eV. Calculations were performed for high-symmetry points of HBL moiré patterns in R- and H-type stackings on the Γ-centered **k** grid of 6×6 divisions with 600 bands and the cutoff energy of 300 eV. Figure 2.9 gives a graphical representation of the energetic ordering of singlet and triplet interlayer exciton states with respective dipolar selection rules and oscillator strengths, labelled

by the according spin configuration and atomic registry of high symmetry stackings in R- and H-type HBLs [P2]. The insets of Figure 2.9a and b show the exciton energy landscape in R- and H-type stacking in the presence of periodic reconstruction, with excitons in triangular $\mathrm{R}_\mathrm{h}^\mathrm{X}$ domains confined by the surrounding potential walls of $\mathrm{R}_\mathrm{h}^\mathrm{M}$ domains, and domains of highest-energy $\mathrm{H}_\mathrm{h}^\mathrm{h}$ excitons in hexagonal tiling. Note that in such potential landscapes, the energy of $\mathrm{R}_\mathrm{h}^\mathrm{X}$ excitons will increase in nanosized domains due to quantum confinement, whereas a decrease is expected for $\mathrm{H}_\mathrm{h}^\mathrm{h}$ excitons due to decreasing potential energy in the surrounding domains. In contrast to singlet excitons, IX_S, where the parallel spin configuration promotes radiative decay, triplet excitons, IX_T, have smaller oscillator strength due to the antiparallel aligned spins [133]. The observation of singlet and triplet exciton manifolds along with their optical recombinations allows to identify individual atomic registries in the experimental chapters.

Chapter 3

Experimental methods

Starting with the CVD grown TMDs this chapter describes the experimental methods used in the scope of this thesis. CVD growth theory, setup, and parameters were introduced with exhibiting optical micrographs of TMDs monolayers and bilayers. The sample fabrication process via the state-of-the-art dry-transfer method was described with giving examples of fabricated samples in the second part of this chapter. The last part of this chapter focused on the confocal microscope used for optical measurements performed under cryogenic conditions.

3.1 Chemical vapor deposition synthesis of transition metal dichalcogenides

3.1.1 Introduction

2D compound materials are regarded as promising candidates in many applications, including electronics [159], optoelectronics [160], flexible devices [161], etc, since they have high carrier mobility, tunable bandgaps, large specific surface area, atomic-level thickness, and lots of other properties [P2, 161]. Moreover, 2D TMDs based bilayers combining two individual ML TMDs provide unique platforms to create an almost virtually unlimited number of materials and show exotic physical phenomena as well as new properties and applications [162]. To achieve these high expectations, materials preparation is the first prerequisite.

In general, mechanical exfoliation, liquid exfoliation, and vapor phase growth are common strategies for the preparation of 2D materials. For example, mechanical exfoliation based on the scotch-tape technique led to the discovery of graphene [1, 163–165], which remains an important method for preparing any other 2D materials [166–168]. However, it always turns out 2D TMD flakes of random thickness, small size, and limited orientation [35, 169], and the technique is also time-consuming, making it challenging to achieve mass production [170]. In addition, liquid phase

exfoliation is the critical method to produce 2D material with a good balance between quantity and cost [171–173]. However, the flake size and quality of solution-prepared TMDs are of concern for some applications [171, 174]. By comparison, the vapor phase based direct growth approaches especially CVD and physical vapor deposition (PVD), is not only a high sample throughput and cost-efficient production [175, 176], in the case of homo- and heterobilayers it ensures clean residue-free interlayer and inherently aligned layers with atomically sharp interfaces both in lateral and vertical geometries [P1, 170, 177–179].

So far, most of the CVD growth process is based on the reaction between transition metal oxide precursors and chalcogen precursors, where both solid metal oxides and chalcogen powders are heated separately into the vapor phase and transported to and react on the substrate surface to form 2D TMDs crystals [175]; and PVD based on vapor phase transport and recrystallization of TMDs, where TMD powders serve as the precursors which are vaporized and transported to the low-temperature substrate region and recrystallize to 2D crystals [136, 180].

3.1.2 CVD growth theory and setup

CVD is a synthesis process in which thin solid films are deposited on the substrates by a chemical reaction of vapor phase precursors [175]. The chemical reactions occur homogeneously in the gas phase and/or heterogeneously on the substrate [181]. Basically, the key steps are that various precursors are transported in the gas phase by sublimation through heating and introduced into the reaction chamber by carrier gas [182]. As the gas flows over a heated substrate, surface reactions may occur to form interesting material in the gas phase during the period of the precursors further decomposition in order to avoid formation of unwanted species which could result in poor film coverage and adhesion [183]. The properties of TMDs are largely dependent on their size, morphology, phase, any interfaces present, etc [184], which can be controlled by playing with the growth parameters such as precursor [185–187], temperature [188, 189], chamber pressure [190, 191], substrate [192, 193], carrier gas flow rate and relative amounts of source materials [194–197]. CVD allows the tuning of the structures and properties of the resulting products, and a variety of advanced CVD systems and their variants have been developed, such as plasma-enhanced CVD (PECVD) [198] and metal organic CVD (MOCVD) [199, 200]. Usually, CVD does not require high vacuum working environments, making it a popular technique for practical applications [201].

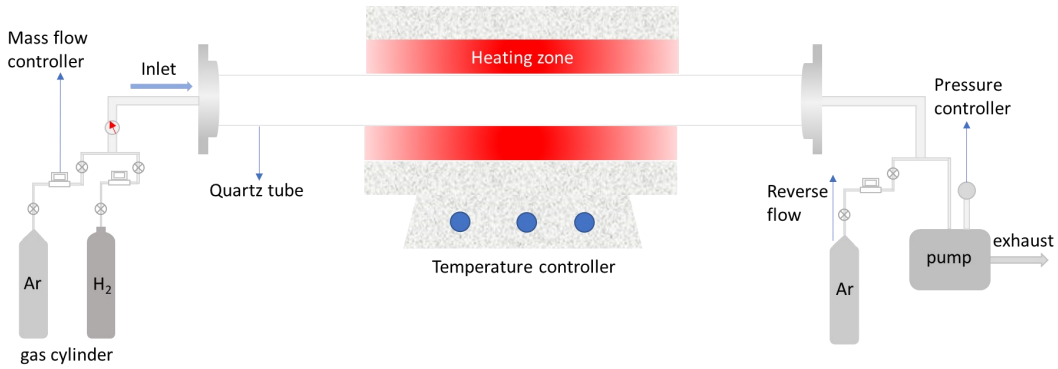

Figure 3.1: Schematic of the solid-precursors based CVD growth equipment employed for the production of TMDs.

To obtain high-quality 2D materials by CVD, suitable equipment is necessary. A CVD system must meet the following basic requirements: controllable manner for delivering the gas-phase reactants; providing sealed reaction chamber; evacuating the gases and controlling the reaction pressure; energy source supplementary for the chemical reactions; treating the exhaust gases safely and harmlessly; and improving the stability of the deposition process with automatic process control [175]. Figure 3.1 shows the schematic of our three-zone furnace CVD system equipped with a 1-inch quartz tube used for 2D TMDs synthesis under atmospheric pressure; ultrahigh purity gases, mass flow controllers (MFCs), a high temperature tube furnace, and pressure control systems are at the heart of the synthesis apparatus. silicon (Si) wafers with 285 nm silicon dioxide (SiO_2) deposited on top are ideal substrates for TMDs synthesis due to their highest optical contrast.

3.1.3 Controlled growth results of single crystals and bilayer TMDs

After a brief introduction to the CVD growth theory and setup, it is instructive to move forward to the real growth experiment of different TMD materials from MLs to homo- and hetero-bilayers.

Synthesis of ML $MoSe_2$. The $MoSe_2$ MLs were grown with parameters relative throughout the literature [202]. In brief, an aluminum boat with molybdenum dioxide (MoO_2) powder (99%, Sigma Aldrich) was placed at the center of the first heating zone and a SiO_2/Si substrate, acting as a deposition acceptor, was suspended face-down on top of it. Here, we use MoO_2 rather than molybdenum trioxide

(MoO_3) because of the single-step chemical reaction, which circumvents the need for any intermediate chemistry and leads to samples of higher quality [186]. Another aluminum boat with selenium (Se) powder (99.99%, Sigma Aldrich) was placed at the upstream side of the quartz tube at a distance of 10 cm to the MoO_2 powder. The furnace temperature was raised up to 750 °C at a rate of 10 °C/min and maintained for 15 min for the growth. During the entire process, 300 standard cubic centimeters per minute (sccm) of untra-high purity argon was flowed into the chamber to act as a carrier gas and protect inert atmosphere. In addition, 0.75 sccm of H_2 was introduced as reductant gas when the temperature reached to 750 °C. The system was cooled down naturally to room temperature after the growth.

Synthesis of ML and homobilayer WSe_2. Tungsten-based 2D TMDs are difficult to produce relying only on the tungsten oxides and chalcogenides as precursors because of the high melting points of its metal oxide precursors [185, 203]. Recent reports on vapor transport and CVD growth of monolayer WSe_2 and tungsten disulfide (WS_2) have shown that the growth requires both high temperature and low pressure [18], however, this approach prevents controllable deposition of uniform large-area films. To this end, alkali metal halides have been enormously used as the growth promoters to facilitate the growth of monolayer WSe_2 at relatively low temperature and atmospheric pressure [22, P1, 187].

In our case, monolayer and homobilayer WSe_2 crystals were synthesized using tungsten dioxide (WO_2) and Se powders (99.99%, Sigma-Aldrich) as precursors and the vapor phase chalcogenization method to obtain high-quality crystalline samples with assistance of sodium chloride (NaCl). An alumina boat containing mixed powder of WO_2 (40 mg) and NaCl (5 mg) was placed at the center of the first zone and a SiO_2/Si substrate was located face-down above the WO_2 powder. Another crucible boat containing Se was placed 25 cm upstream from the center of the first zone. After the tube was evacuated to 10 mTorr several times to remove air and moisture, the reaction chamber pressure was increased to ambient pressure through 500 sccm argon gas flow. Then, 140 sccm pure argon was used during the furnace heated to the target growth temperature with a ramping rate of 50 °C/min. Upon reaching the target temperature, 10 sccm H_2 was added to the Ar flow before cooling down. In general, the yields of single crystals and 3R stacked crystals were the highest at 960 °C for 3 min and 5 min, respectively, while 2H stackings were obtained at higher temperatures such as 975 °C for our results.

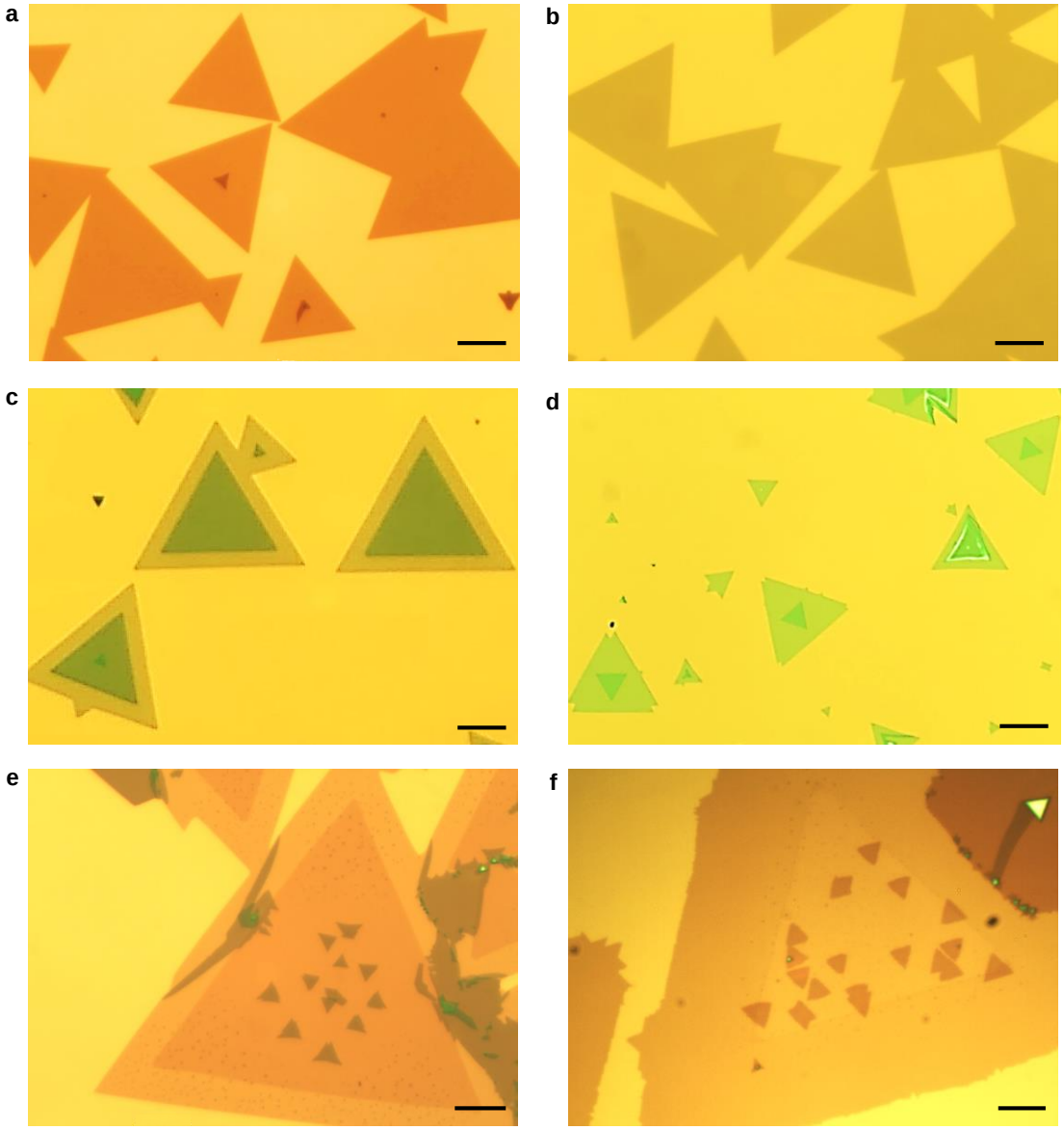

Figure 3.2: Optical microscope images of CVD grown TMDs. **a** and **b**, ML $MoSe_2$ and WSe_2. Scale bars: 30 μm. **c** and **d**, 3R and 2H BLs of WSe_2. Scale bars: 20 μm. **e** and **f**, $MoSe_2$/WSe_2 and WS_2/WSe_2 HBLs. Scale bars: 10 μm.

Synthesis of heterobilayer WSe_2/$MoSe_2$ and WSe_2/WS_2. The WSe_2/$MoSe_2$ and WSe_2/WS_2 HBL samples were grown by a modified two-step CVD method, with the first growth of an atomic $MoSe_2$ or WS_2 layer and then WSe_2 single layers on top. The as-prepared $MoSe_2$ monolayers were used as the new substrate for the vertically

growth of the WSe_2 monolayers. The tungsten diselenide powder (99.8%, Alfa Aesar) and the substrate with the $MoSe_2$ monolayers were placed at the center and downstream of the quartz tube respectively. During the temperature-increasing stage, a reverse flow of 100 sccm cold argon gas was used to cool the existing $MoSe_2$ nanosheets and restrain thermal degradation. The center zone of the furnace was heated to 1090 °C with a ramping rate of 30 °C/min under atmospheric pressure. After reaching the desired temperature for WSe_2, the reverse gas was switched to a mixture of 200 sccm Ar/H_2 (with 2% H_2) forward gas flow used to carry the vaporized WSe_2 source to the substrate. Here, H_2 was used to accelerate the deposition to get larger flakes at short growth time. Then the growth temperature was maintained for 3 min for the epitaxial growth of WSe_2. After the growth, the furnace was cooled down to the room temperature quickly. All the CVD grown results are included in Figure 3.2.

3.2 Sample fabracation

All of our CVD synthesized TMDs using SiO_2/Si as the growth substrates. However, because of the amorphous nature of the SiO_2/Si substrate and its relatively high surface roughness, the optical transition linewidths even at low temperature are typically as large as a few tens of meV and contain homogeneous and inhomogeneous contributions, which prevents in-depth studies [18, 204]. As demonstrated in many reports that encapsulation of TMDs in hBN can efficiently suppress the inhomogeneous contribution to the exciton linewidth [204], indicating that surface protection and substrate flatness are key ingredients for obtaining stable, high-quality samples. Therefore, it is instructive to give a detailed introduction of how to fabricate high-quality samples, which includes stamp preparation and transfer technique.

Stamp preparation. In order to pick up and transfer the flakes we use a stamp consisting of a layer of poly-Bisphenol A-carbonat (PC) film mounted on a block of polydimethylsiloxane (PDMS) for mechanical support [205]. A PC film is prepared by drop casting a solution in chloroform (6% weight) onto a glass slide. A second slide is then used to sandwich and spread the solution between the two slides. The slides are immediately slid apart, and left to allow the chloroform to evaporate. After drying, the resultant film is picked up and mounted on a PDMS block to complete the stamp. A detailed description of the stamp preparation is reported in Figure 3.3.

Transfer process. Step 1: Pick up of the top hBN from the SiO_2 surface. A piece of

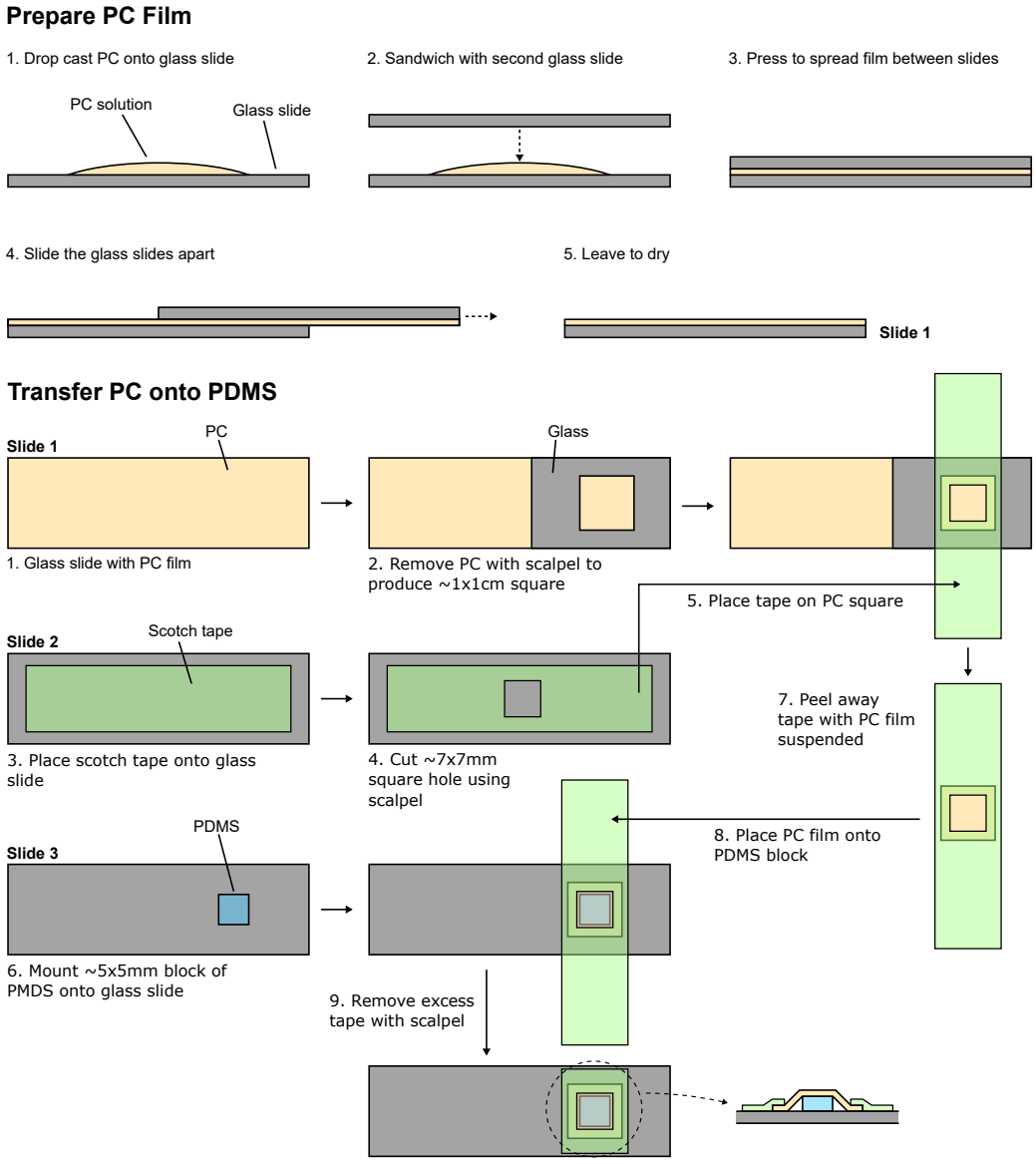

Figure 3.3: Schematic diagram of the PC/PDMS stamp preparation process. The PC solution is prepared by dissolving 6%-8% by weight polycarbonate in chloroform. The method for preparing the transfer stamp is outlined in the figure above. The PC is drop cast onto a glass slide, and another glass slide is then used to sandwich and spread the solution between the two slides. The slides are immediately slid apart, and left to allow the chloroform to evaporate. A 1×1 cm window is cut into a piece of scotch tape, which is then used to pick up the PC film from the glass slide. The tape is then used to place the PC onto a block of PDMS (a few mm thick), and excess tape is removed by a scalpel. Adapted from Ref. [205].

SiO_2/Si with exfoliated hBN is placed on a microscope hot plate stage. The glass slide is attached to a micromanipulator and kept approximately horizontal above the sample, with the polymer facing down. The PDMS/PC stamp is placed in contact with the hBN flake by lowering the glass slide along the z-axis of the micromanipulator. When the polymer contacts with SiO_2/Si surface, the temperature is raised to a range of 50-60 °C with a ramping rate of 3 °C/step to let the polymer move forward to completely cover the hBN. Keeping the contact at this temperature for 3 min, then withdrawing. Step 2: Pick up TMDs using hBN attached stamp. A SiO_2/Si substrate with CVD grown flakes is placed on the heating stage. The temperature is raised to 100 °C. A previously picked-up hBN flake is aligned over a chosen TMD flake with some separation between the surfaces. The glass slide is lowered until the polymer comes into contact with the SiO_2 surface. By further increasing the temperature to 110-120 °C, the hBN flake proceeds until reaching full contact with the TMD. It is important to proceed as slow as possible, in order to avoid bubbles between hBN and TMD. When fully in contact, keeping at this temperature for 5 min and then withdrawing again by lifting the glass slide very slowly. For direct comparison of $MoSe_2$/WSe_2 heterostructures, we also prepare samples from mechanically exfoliated ML $MoSe_2$ and WSe_2, which can be easily picked up at low temperature around 50 °C. Step 3: Encapsulation of TMDs by picking up bottom hBN. The polymer with hBN and TMDs is aligned over a chosen hBN on SiO_2 surface. Then the procedure is repeated in 'Step 1' to pick up hBN. Step 4: Releasing and annealing. During the final step of the cleaning process, where the PC is brought into contact with the substrate and the temperature is raised to 170 °C, the edges of the PC tear, releasing it from the scotch tape, allowing the stamp to be withdrawn while the PC remains on the substrate surface. In order to promote the adhesion among the hBN and TMDs flakes, the SiO_2/Si substrate with the stack is baked on a hot plate (in air) at 200 °C for 10 min. Then soaked in chloroform solution for 20 min to remove PC residues, cleaned by acetone and isopropanol and annealed at 200 °C under ultrahigh vacuum for 15 hours. All the samples we studied are shown in Figure 3.4.

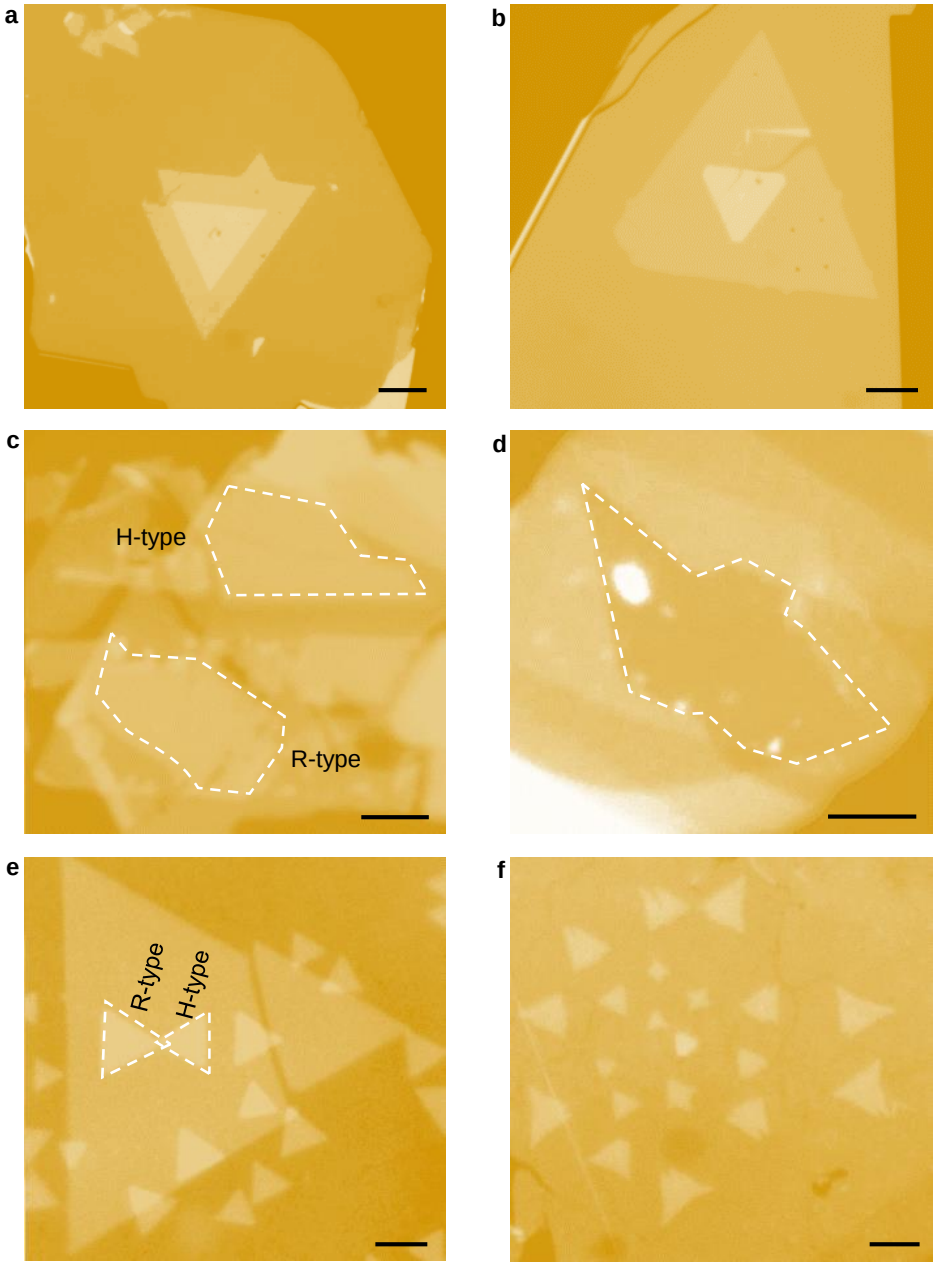

Figure 3.4: Optical microscope images of hBN encapsulated samples studied in our work. **a** and **b**, hBN encapsulated CVD grown homobilayer 3R and 2H WSe_2. Scale bars: 10 μm. **c** and **d**, hBN encapsulated well twist aligned and twist angle 3° $MoSe_2/WSe_2$ HBLs build of exfoliated MLs. **e** and **f**, hBN encapsulated $MoSe_2/WSe_2$ HBLs consisting of CVD grown MLs and from directly CVD growth. Scale bars: 5 μm in **c**-**f**.

3.3 Cryogenic confocal microscope

After the sample preparations, we mainly investigate their optical properties perfromed with a lab-built confocal microscope in back-scattering geometry (Figure 3.5 Measurement setup) at cryogenic temperature [P1, 45, P2]. The samples were loaded into a closed-cycle cryostat (attocube systems, attoDRY 1000) with a base temperature 3.2 K. The cryostat was equipped with a superconducting magnet providing magnetic fields of up to 9 T in Faraday configuration. Piezo-stepping and scanning units (attocube systems, ANPxy101, ANPz101, and ANSxy100) were used for sample positioning with respect to a low-temperature apochromatic objective (attocube systems, LT-APO/NIR/0.81). PL spectroscopy measurements of homobilayer WSe_2 were conducted with a lab-built continuous-wave (CW) laser at 670 nm. For optical studies of $WSe_2/MoSe_2$ heterostructures, a Ti: sapphire laser (Coherent, Mira) in CW mode was employed to excite the samples and was tuned to the resonance of intralayer exciton transition in ML WSe_2 at 730 nm. A stabilized Tungsten-Halogen lamp (Thorlabs, SLS201L) was used as a broadband light source to measure differential reflectance (DR). The PL or reflection signal were spectrally dispersed by a monochromator (Roper Scientific, Acton SP2500 or Acton SpectraPro 300i with a 300 grooves/mm grating) and detected by a liquid nitrogen cooled or Peltier cooled charge-coupled device (Roper Scientific, Spec-10: 100BR or Andor, iDus 416). A set of linear polarizers (Thorlabs, LPVIS), half- and quarter-waveplates (B. Halle, 310-1100 nm achromatic) mounted on piezo-rotators (attocube systems, ANR240) were used to control the polarization in excitation and detection. The DR spectra were obtained by normalizing the reflected spectra from the HBL region (R_0) to that from the sample region without $MoSe_2$ and WSe_2 layers (R) as DR = (R-R_0)/R_0. Time-resolved PL was excited with a wavelength-tunable supercontinuum laser (NKT Photonics, SuperK Extreme and SuperK Varia) at 730 nm with a pulse duration of 6 ps and repetition rates down to 0.625 MHz, detected with a silicon avalanche photodiode (PerkinElmer, SPCM-AQRH-15) and correlated with a time-correlating single-photon counting module (PicoQuant, PicoHarp 300).

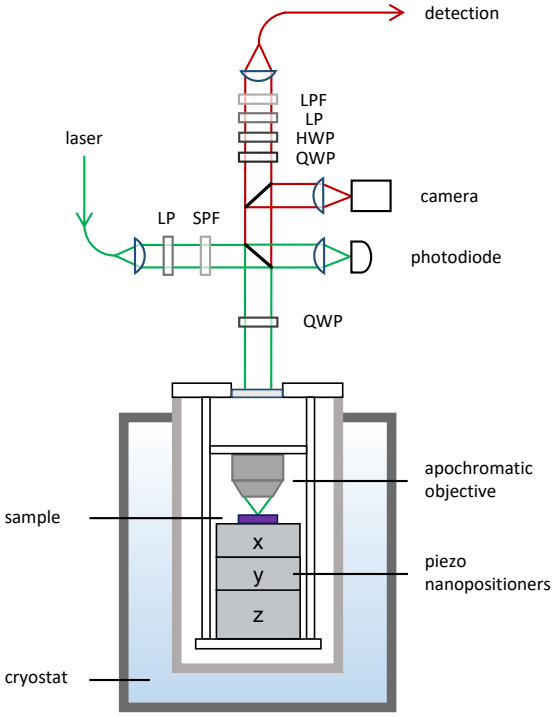

Figure 3.5: Schematic of the cryogenic confocal system used for photoluminescence and differential reflection experiments. A single-mode fiber-coupled laser light was passed through a linear polarizer (LP), a short-pass filter (SPF), and then was reflected off a beam splitter and guided to the sample through a focusing objective. In between, a quarter wave plate (QWP) was used for circularly polarized excitation control. The luminescence from the sample was collected by the microscope objective and transmitted through two cross-aligned beam splitters for unaltered polarization analysis by the optional upper QWP, HWP (half wave plate), and LP, which also corrected the polarization modifications by the lower QWP. A long-pass filter (LPF) was used to eliminate reflected laser light from the luminescence signal, which was coupled into a single-mode fiber. The laser light, reflected off the upper BS and focused onto a charge-coupled device (CCD), was used for sample orientation. The measurement systems used for detection of the luminescence were either a grating spectrometer or an avalanche photodiode (APD). Adopted from Ref. [112].

Chapter 4

Stacking-dependent properties of CVD-grown WSe_2 homobilayers

THIS CHAPTER IS BASED ON THE PUBLICATION [P1]
Li, Z., Förste, J., Watanabe, K., Taniguchi, T., Urbaszek, B., Baimuratov, A. S., Gerber, I. C., Högele, A. & Bilgin, I. Stacking-dependent exciton multiplicity in WSe_2 bilayers. *Phys. Rev. B* **106,** 045411 (2022)

The following chapter describes the results of spectroscopic studies on CVD-grown WSe_2 homobilayers. Beginning with characterizations of the 2H and 3R registries by atomic force micrographs (AFM) and Raman spectroscopy. Subsequent cryogenic PL measurements of ML with variations in excitation power confirms the high quality of our crystals. PL and DR measurements reveal different intralayer and interlayer transitions between 2H and 3R stackings. An interpretation of the optical transitions is supported by measurements of mageto-luminescence and very self-consistent theoretical calculations.

4.1 Introduction

The optical properties of TMD semocondoctors are governed by excitons in different spin, valley and layer configurations [24, 38]. Among possible realizations of TMD systems, heterobilayers and homobilayers stand out as hosts of excitons with layer-indirect character. Initial studies of homobilayers were limited to natural 2H layer stacking [27, 206, 207], extracted by exfoliation from native crystals and structurally different from 3R stacking. Variations of the twist angle in WSe_2 bilayers away from 2H and 3R stacking revealed novel phenomena ranging from correlated electronic phases [208] to moiré exciton physics [14, 100] with angle-controlled exciton coherence and dynamics [14, 29, 37], Coulomb correlations in effectively flat moiré exciton bands [209] or optical nonlinearities [83]. A particularly attractive

feature of interlayer excitons in related homobilayer systems is provided by the permanent dipole moment of layer-indirect excitons [25, 210, 211] which promotes exciton-exciton dipolar interactions, allows employing electric fields to tune the optical properties via the Stark effect [37–40, 212–214] or implementing exciton trapping and routing [215]. The electrostatic dipole moment depends on the degree of exciton layer delocalization, which in turn is sensitive to the interlayer coupling and thus to the stacking order, as was shown recently by optical absorption for 2H and 3R MoS_2 BLs for transitions involving momentum direct KK excitons [12, 216]. In contrast to absorption probing zero-momentum exciton transitions, the PL of BLs is dominated by momentum-indirect excitons [9, 33] via luminescence phonon sidebands [34–36] which exhibit shift linear energy shifts in perpendicular electric fields according to the Stark effect [37–40]. The most recent observation of two different slopes in the energy dispersion of phonon sideband emission from 2H WSe_2 BL in electric field [39, 40] indicates the presence of two degrees of electron-hole layer separation, with respective dipole moments attributed to excitons in distinct QK and $Q\Gamma$ reservoirs [39, 40]. Experiments employing strain tuning [41] and magnetic fields [35], on the other hand, suggest that the PL sidebands stem exclusively from QK excitons, indicating shortcomings in the present understanding of the underlying lowest-energy exciton reservoirs with finite center-of-mass momenta.

To provide comprehensive insight into the nature of exciton reservoirs in BL WSe_2 with different spin, momentum and layer character, we performed experimental and theoretical studies of 2H and 3R stackings with contrasting spectroscopic responses. To access spectrally narrow exciton transitions, we synthesized high-quality WSe_2 crystals by CVD, yielding 2H and 3R as two stable limits of the relative layer orientation. As opposed to BL crystals of MoS_2 [12, 217, 218] and WS_2 [219, 220] synthesized by CVD, studies of WSe_2 BLs in 3R stacking have remained elusive due to the challenge of perfect layer alignment. The only realization of nominal zero-angle twist so far has been obtained from exfoliation stacking [37], which can only approximate the ideal 3R layer order inherent to CVD growth. Moreover, the spectral features of BLs aligned near zero twist can be compromised by marginal-angle reconstruction [14, 48–50] with interfacial ferroelectricity effects [221].

In the following, we present a comprehensive study of excitons in 2H and 3R WSe_2 BLs, performed with cryogenic optical spectroscopy on CVD-synthesized high-quality crystals. With a set of complementary spectroscopy techniques, we identify contrasting responses of 2H and 3R BL configurations and observe rich

exciton multiplicity in the 3R case. We relate the differences between the optical spectra of 2H and 3R BL stackings to the nature of excitons in different spin, valley and layer configurations. Our interpretation is based on first-principles calculations of the band structure, optical absorption and exciton g-factors. Theory analysis shows that in contrast to 2H stacking, the top and bottom layers in 3R stacking differ in their band structure and exhibit different optical bandgaps. This insight resolves the recent puzzle of two distinct intralayer KK exciton transitions observed in absorption on nearly aligned WSe_2 BLs [37]. Moreover, our theoretical analysis highlights the multiplicity and degree of layer delocalization for interlayer excitons in both 2H and 3R stackings, thus providing an intuitive explanation for different electrostatic dipole moments of QK excitons without the requirement of involving $Q\Gamma$ states [39, 40].

4.2 Sample characterization with Raman spectroscopy

WSe_2 BL crystals in 2H and 3R stackings were obtained from CVD synthesis. AFM results in Figure 6.2a and b show respective WSe_2 crystals with ML and BL regions in 2H and 3R configurations with 60° and 0° rotational alignment of the two WSe_2 MLs, as can be deduced directly from the edges of CVD flakes with the same edge termination. The corresponding atomic registries are illustrated in the bottom panels of Figure 6.2a and b, showing side (left) and top (right) views and the BL unit cell by dashed boxes. The 2H and 3R stacked BL configurations are the two energetically most favorable, which is the reason they are commonly observed in CVD grown samples with ML and BL regions of the same crystal [222].

Initial characterization of the two distinct crystal configurations was performed with Raman spectroscopy at ambient conditions. A typical Raman spectrum from a ML region is shown in Figure 6.2c. It features degenerate in-plane E' and out-of-plane A_1' first-order Raman modes around 249 cm^{-1}, the double resonance 2LA mode at 257 cm^{-1}, and a series of multi-phonon modes at 358, 372, and 395 cm^{-1}, all of which are consistent with ML features [80, 223–227]. The degeneracy of the E' and A_1' modes, characteristic of MLs [226, 227], is lifted in the Raman spectra of both 2H and 3R BLs shown in Figure 6.2d. We determined by using Lorentzian fit in Figure 6.2e and f that in both BL stackings the respective E^1_{2g} and A_{1g} modes exhibit the same frequency splitting of ~ 2 cm^{-1} due to interactions between the layers, with a factor of 10 higher ratio of the E^1_{2g} to A_{1g} peak intensities in the 3R case as compared to 2H. Experimental values from fitting are summarized in Table 4.1. We also observe a red-shift of the E'/E^1_{2g} and a blue shift of the A_1'/A_{1g}

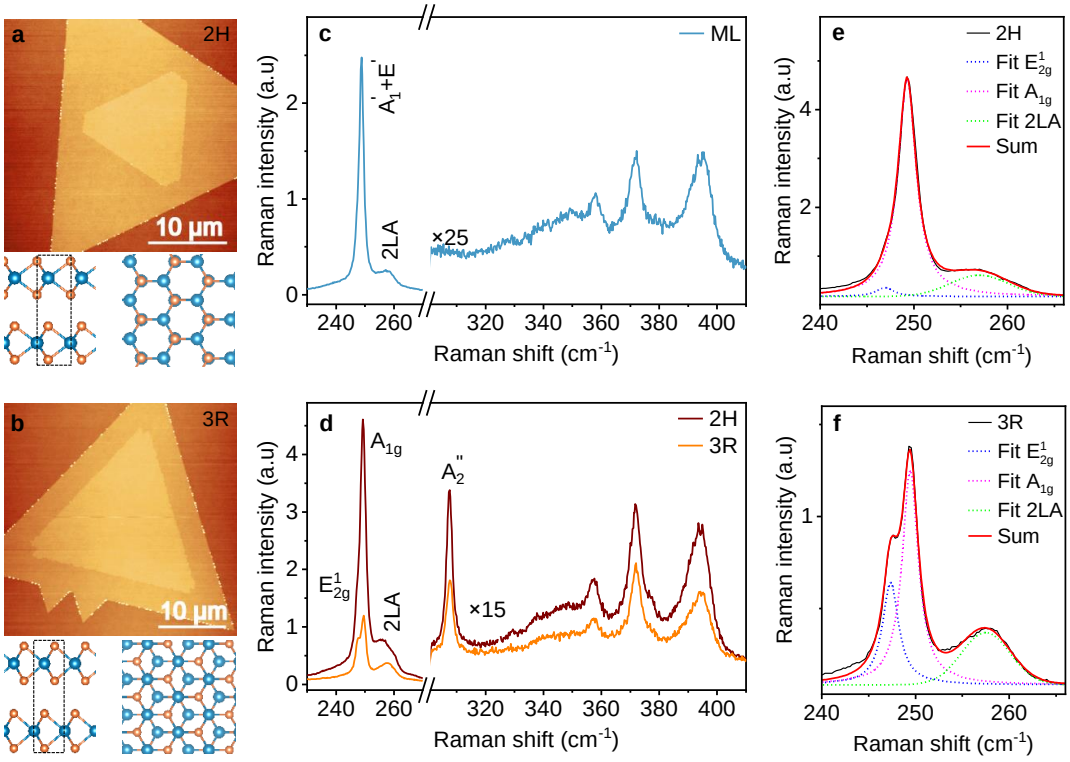

Figure 4.1: a and **b**, Atomic force micrographs of 2H and 3R homobilayer WSe_2 on SiO_2/Si, respectively, with side and top view illustrations of the respective stacking orientations shown below (blue and orange spheres represent W and Se atoms, respectively, dashed rectangles indicate the unit cell). **c** and **d**, Room temperature Raman spectra of ML and BL WSe_2 in 2H and 3R stacking (the spectra were recorded with excitation at 532 nm and normalized to the peak intensity of the Si phonon mode at 520 cm^{-1}; note that the intensity of higher-order Raman modes associated with multi-phonon processes were scaled for increased visibility). The in-plane and out-of-plane phonon modes, E' and A_1', are degenerate in the ML but split by 2 cm^{-1} both in 2H and 3R homobilayer WSe_2. **e** and **f**, Lorentzian fitting of the in-plane (E^1_{2g}) and out-of-plane (A_{1g}) Raman modes for 2H and 3R stacking.

modes for both stackings [228]. The peak at 308 cm^{-1}, labelled as A_2'', is absent in the ML limit but very pronounced in the Raman spectra of both 2H and 3R stackings as a hallmark of BL regions [80, 223, 226, 227]. The spectra of multi-phonon modes at frequencies above 350 cm^{-1} are similar in ML and BLs.

Stacking	Peak	FWHM (Γ)	Intensity	Frequency ω(cm^{-1})	$\Delta\omega$ (cm^{-1})
2H	E^1_{2g}	2.35	0.18 ± 0.04	246.91 ± 0.30	2.37
2H	A_{1g}	2.35	4.44 ± 0.04	249.28 ± 0.01	
2H	LA	7.35	0.44	256.98 ± 0.14	
3R	E^1_{2g}	2.11	0.56 ± 0.01	247.34 ± 0.03	2.1
3R	A_{1g}	2.11	1.16 ± 0.01	249.44 ± 0.01	
3R	$2LA$	6.13	0.28	257.50 ± 0.06	

Table 4.1: The peak positions and intensities of the main Raman modes in the bilayers WSe_2 with two different stacking configurations.

4.3 Differential reflectivity and photoluminescence spectroscopy

Having identified 2H and 3R BL crystals by AFM and Raman spectroscopy, we performed cryogenic micro-PL and DR spectroscopy experiments. Intensities of PL spectra are a convolution of oscillator strength and exciton population, and measurements of DR probe the direct radiative transition pathway. Therefore, DR spectroscopy is a complementary tool in identifying the zero-momentum radiation processes used for ML [229] as well as for BL TMDs [230]. To this end, the CVD-grown crystals were encapsulated in hBN by standard lift-off and exfoliation and transferred onto a SiO_2/Si substrate. Typical PL and DR spectra of ML regions, recorded at 3.2 K, are shown in Figure 4.2a. Both spectra feature the resonance of the fundamental exciton transition (X) around 1.71 eV with a spectrally narrow full-width at half-maximum (FWHM) linewidth of 4 meV, exceeding the transform-limited linewidth of 1 meV in best hBN-encapsulated MLs obtained from native crystals [204, 231–233] yet slightly narrower than 5.2 meV reported for CVD-grown MoS_2 ML in hBN [233]. The second pronounced peak in the PL spectrum at 1.69 eV corresponds to the biexciton (denoted by XX) emission with a characteristic 20 meV red-shift [234–238] and superlinear dependence on the excitation power shown in Figure 4.2b. All of the main ML features in PL and DR confirm the overall high quality of our CVD-grown crystals.

The cryogenic PL and DR of BL regions with 2H and 3R stackings are shown in

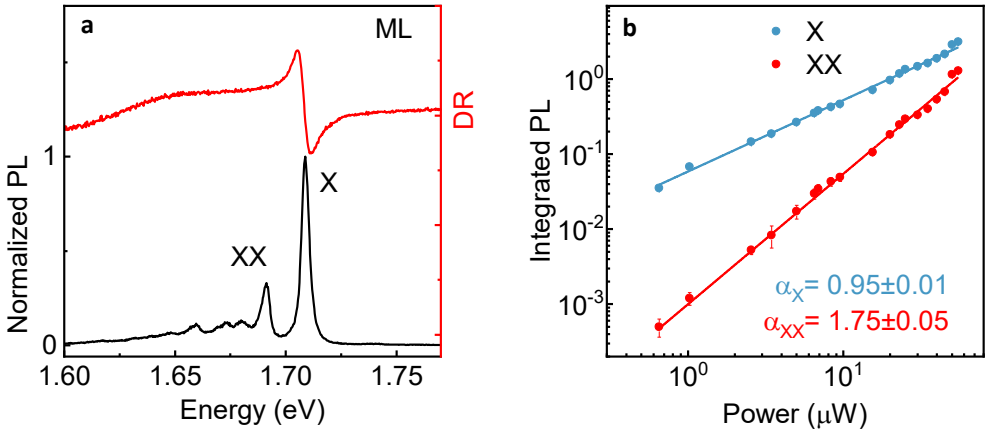

Figure 4.2: a, Normalized photoluminescence (black) and differential reflectivity (red) spectra at 3.2 K, recorded in the ML region of hBN-encapsulated BL WSe_2 crystals. The ML exciton (X) and biexciton (XX) peaks exhibit characteristic linear and superlinear scaling of the integrated PL intensity as a function of the excitation power, as evident from data and respective power-law fits I_{PL}/P^{α} by solid lines in **b**.

Figure 4.3a and b with pronounced differences in the spectral characteristics. The 2H spectra in Figure 4.3a agree with the results of previous studies on exfoliated BLs from bulk WSe_2 [34–37, 41, 239], with the neutral exciton resonance X at around 1.72 eV associated with momentum direct transitions between conduction and valence band states at K, as well as a series of PL peaks between 1.55 and 1.61 eV we label as P_1 to P_4 with increasing red-shift. Consistent with the indirect band gap of WSe_2 BL between the conduction band minima at the six inequivalent Q-points of the first Brillouin zone and the valence band maximum at K [227, 240], the lowest energy exciton states form as QK and $Q'K$ with finite center-of-mass momentum and characteristic phonon sideband luminescence into the peaks P_1 through P_4 [35, 36]. As on ML regions, the high-quality of our CVD-synthesized crystals is reflected by spectrally narrow features of BLs in both stackings.

The characteristic features of 2H WSe_2 BL are contrasted by the spectra from 3R stacking. First, the peak multiplicity increases both in PL and DR spectra of Figure 4.3b. We observe two distinct exciton resonances X_1 and X_2 around 1.70 and 1.68 eV with an energy splitting of 17 meV and spot-to-spot variations between 16 and 20 meV, which is very different from the single transition observed throughout the 2H stacked sample. This is in very good agreement with our band

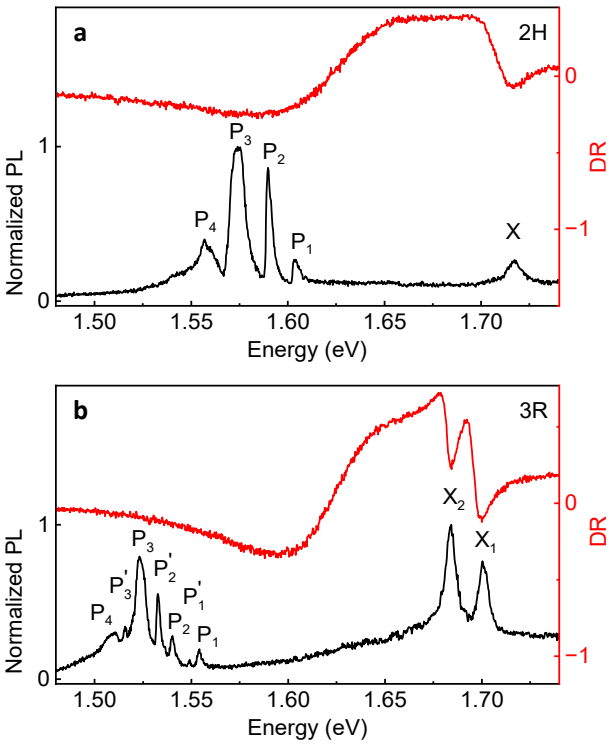

Figure 4.3: a and **b**, Normalized photoluminescence (PL, black) and differential reflectivity (DR, red) spectra of 2H and 3R WSe_2 at 3.2 K. In contrast to 2H with only one resonance of the fundamental exciton X, the spectra of 3R exhibit two exciton peaks X_1 and X_2 with a splitting of 17 meV both in PL and DR. Moreover, the series of phonon sideband PL peaks P_1 to P_4 in 2H red-shifts by 50 meV in 3R and features additional peaks P_1' to P_3'. The contrast change in DR between the phonon sideband groups and the main exciton resonances are presumably due to phonon-assisted excitation of momentum-indirect states.

structure calculations in Chapter 2 and we infer that the two transitions correspond to A-excitons in the top and bottom layer. As a second important observation, we find in the range of phonon sidebands between 1.50 and 1.55 eV three additional peaks emerging in between P_1 through P_4, which we label as P_1', P_2' and P_3'. Moreover, we note the red-shift of 16 meV from the KK exciton resonance X in 2H to X_1 in 3R, as well as a larger red-shift to the first phonon sideband P_1 of QK exciton states, increasing from 100 meV in 2H to 150 meV in 3R as a consequence of stronger interlayer hybridization in the latter case.

4.4 Exciton g-factors from experiment and theory

To get further insight into the momentum transitions of exciton multiplicity in 2H and 3R WSe_2 BLs, we determined the exciton g-factors from magneto-luminescence measurements and correlated them with theoretically calculated values in different spin, valley and layer configurations [35, 45]. Out-of-plane magnetic field breaks the time-reversal symmetry and lift the valley degeneracy between σ^+ and σ^- polarized PL peaks with energies E^+ and E^- to induce a valley Zeeman splitting $\Delta = E^+ - E^- = g\mu_B B$ proportional to the exciton g-factor, the Bohr magneton μ_B, and the magnetic field B [116, 241–243]. Polarization-resolved magneto-luminescence spectra of 2H and 3R WSe_2 BLs, recorded at $B = -8$ T with σ^+ and σ^- circular detection under linearly polarized (π) excitation, are shown in Figure 4.4a and b. The exciton g-factors follow from linear fits to the data shown by a solid lines in Figure 4.4c and d and grouped in color according to the g-factor values.

For 2H BL(Figure 4.4c), we found for the fundamental exciton peak X the characteristic g-factor of -4.3, as well as g-factors of momentum-indirect QK excitons (i.e. Coulomb-correlated states of the conduction band electron in the Q-valley and valence band vacancy in the K-valley) in the range from -9.3 to -10.9 (peak P_1 through P_4), consistent with previous findings for exfoliated WSe_2 BLs in 2H stacking [35]. In 3R stacking, our high-quality sample with spectrally narrow PL emission allows us to quantify two distinct g-factors of -4.3 and -4.8 for momentum-direct KK exciton doublet X_1 and X_2 (Figure 4.4d). For the emission peaks at lower energy between 1.50 and 1.55 eV, we determined g-factors of about -11 as in 2H (peak P_1 through P_4) and an additional group of peaks (peak P'_1 through P'_3) with a g-factor close to -14. According to our understanding of the band structure and exciton g-factors in 2H WSe_2 BL, the peak P_1 through P_4 stem from phonon-assisted recombination of QK excitons, without contribution of $Q\Gamma$ states with small g-factors between 0 and 4 [35].

To interpret the origin of additional peaks in 3R stacking with distinct magneto-luminescence features as well as their difference to the 2H configuration, we calculated the exciton g-factors from first principles [35, 45, 244–246]. The results for both stackings are presented in Table 4.2 and pictorially also in Figure 4.4e and f. In the case of 2H, the g-factor of X corresponds to spin-like (upup) KK transition, whereas momentum-indirect exciton peaks (P_1 to P_4) relate to spin-like intralayer QK and interlayer $Q'K$ transitions with $g = -9.51$. For transitions in 3R, our results also identify spin-like KK excitons X_1 and X_2 with two different g-factors of -4.18

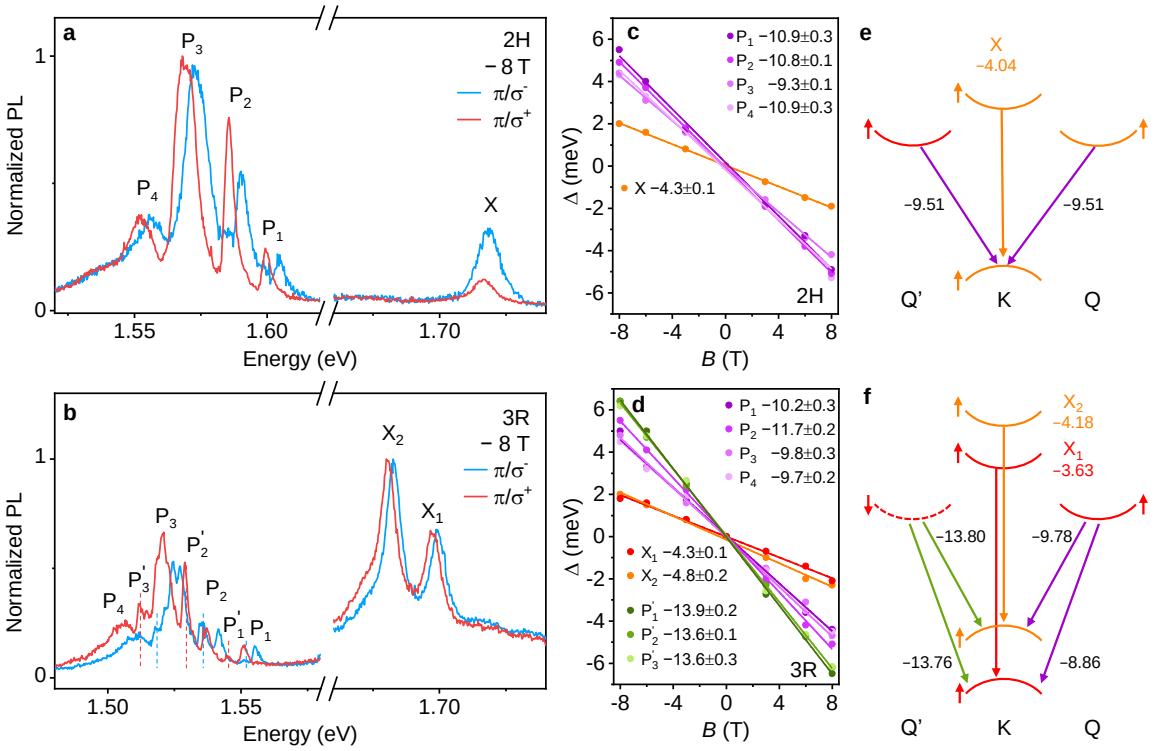

Figure 4.4: **a** and **b**, Photoluminescence spectra of 2H and 3R WSe_2 in a magnetic field of -8 T recorded with σ^+ (red) and σ^- (blue) polarized detection under linearly polarized excitation (π). Magneto-induced splittings of peaks in 3R WSe_2 are indicated in **b** by dashed lines. **c** and **d**, Valley Zeeman splitting Δ of all peaks identified in 2H and 3R WSe_2 magneto-luminescence as a function of magnetic field. The respective exciton g-factors were extracted from linear fits (solid lines) to the data and grouped by colors. **e** and **f**, Schematic illustration of momentum-direct and phonon-assisted transitions in 2H and 3R, tagged with theoretical exciton g-factor values (solid and dashed lines denote spin-up and spin-down bands; orange and red colors indicate the bands of the first and second layer degenerate in 2H but split in 3R stacking).

and -3.63. This difference in the theoretical values arises from different g-factors of the conduction bands at K in the top and bottom layer L_1 and L_2.

Momentum-indirect excitons with peaks P_1 to P_4 in 3R with similar g-factors to the corresponding peaks in 2H stem from spin-like intralayer and interlayer QK transitions with $g = -8.86$ and $g = -9.78$, respectively. Additional 3R peaks with relatively large g-factors (P'_1 to P'_3), on the other hand, originate from spin-unlike intralayer and interlayer $Q'K$ transitions with g-factors of -13.80 and -13.76. We note that in 2H, spin-unlike intralayer $Q'K$ and interlayer QK transitions with

Table 4.2: Theoretical exciton g-factors in 2H and 3R WSe_2 bilayers. We distinguish between intra- and interlayer excitons and show for momentum-direct KK transitions only the g-factors of intralayer excitons. For momentum-indirect QK and $Q'K$ transitions, we select spin-valley configurations of intra- and interlayer excitons with lowest energies. The transition column ($L_{\text{cb}} \rightarrow L_{\text{vb}}$) indicates the layers with conduction and valence band electrons involved in phonon-assisted recombination.

Exciton				g-factors	
Intralayer	Interlayer	Spin	Transition	2H	3R
KK		$\uparrow\uparrow$	$L_1 \rightarrow L_1$	-4.04	-3.63
KK		$\uparrow\uparrow$	$L_2 \rightarrow L_2$		-4.18
QK		$\uparrow\uparrow$	$L_1 \rightarrow L_1$	-9.51	-8.86
	QK	$\uparrow\uparrow$	$L_1 \rightarrow L_2$	-9.78	
	$Q'K$	$\uparrow\uparrow$	$L_1 \rightarrow L_2$	-9.51	
Q'K		$\downarrow\uparrow$	$L_1 \rightarrow L_1$	-13.71	-13.76
	$Q'K$	$\downarrow\uparrow$	$L_1 \rightarrow L_2$		-13.80
	QK	$\downarrow\uparrow$	$L_1 \rightarrow L_2$		

$g = -13.71$ from Table 4.2 are not observed within the signal-to-noise ratio of our experiment. Theses states are degenerate with the two respective spin-like interlayer $Q'K$ and intralayer QK transitions, yet their exciton population seems to be vanishingly small, presumably due to spin-conserving relaxation [37]. However, once the degeneracy of the states is removed by the lack of inversion symmetry in 3R stacking, our analysis shows that spin-unlike $Q'K$ excitons light up in the PL of peaks P'_1 to P'_3.

4.5 Conclusions

In conclusion, we carried out extensive experimental and theoretical studies of BL WSe_2 to identify stacking-dependent optical response of 2H and 3R crystals. We find the marked differences arise from distinct multiplicity of intralayer and interlayer excitons in the two different stable realizations of BL stackings. Using high-quality samples of both stacking configurations by CVD crystal synthesis and hBN-encapsulation, we obtain spectrally narrow resonances which allow us to identify in great detail the characteristics of momentum-direct excitons in absorption and momentum-indirect excitons in emission of 2H and 3R BLs. For both stackings

we find that the lowest-energy PL is dominated by momentum-indirect QK and $Q'K$ excitons with intralayer and interlayer character. The different degrees of layer delocalization give rise to two different electrostatic dipoles, providing an explanation for the recent observations of two distinct slopes in the first-order Stark effect. Moreover, our results demonstrate that exciton state multiplicity, transition energies and oscillator strengths sensitively depend on the BL stacking order, and highlight how layer-degenerate excitons in inversion symmetric 2H BLs split into exciton doublet in 3R stacking with broken inversion symmetry and different atomic registries for the top and bottom layers. Our findings are relevant for the understanding of other TMD homobilayer systems as well as semiconductor van der Waals heterobilayers with varying degrees of symmetry, twist and interlayer hybridization.

Chapter 5

Excitons in reconstructed $MoSe_2$-WSe_2 heterostructures

THIS CHAPTER IS BASED ON THE MANUSCRIPT [P2]
Zhao, S., Li, Z., Huang, X., Rupp, A., Göser, J., Vovk, I., Kruchinin, S., Watanabe, K., Taniguchi, T., Bilgin, I., Baimuratov, A. & Högele, A. Excitons in mesoscopically reconstructed moiré hetersotructures. *arXiv preprint.* arXiv: 2202.11139 (2022)

Based on the theoretical model of atomic reconstruction in marginally-twisted $MoSe_2$/WSe_2 heterobilayers. This chapter focuses on the expansion of nanoscale lattice reconstruction to the mesoscopic scale of extended samples and demonstrates rich consequences in optical studies of excitons in $MoSe_2$-WSe_2 heterostructures with parallel and antiparallel alignment. It explains consistently the coexistence of spectra characteristics of zero-, one- and two-dimensional domains consisting of just one atomic registry in one and the same sample by the correlation of cryogenic optical measurements and SEM images. In addition, this chapter demonstrates that there are non-reconstructed moiré patterns in samples with large twist angles.

5.1 Introduction

Vertical assemblies of twisted or lattice-mismatched HBLs of 2D TMDs with modulated van der Waals interlayer coupling in moiré superlattices give rise to correlated Hubbard model physics [130, 247] with signatures of collective phases in transport [208, 248–250] and optical experiments [247, 251–253]. Periodic moiré interference patterns on the length scale of a few nanometers [254] have profound effects on the electronic band structure via the formation of flat mini-bands which enhance many-body correlations and induce emergent magnetism [247], correlated insulating states [208, 248, 249, 251–253] or Wigner crystals [251] with periodic order in spatial charge distribution [255]. Moiré effects also result in rich

optical signatures of intralayer [256] and interlayer [19, 47] excitons formed by Coulomb attraction among layer-locked and layer-separated electrons and holes, with angle-controlled exciton valley coherence and dynamics [14, 29, 37].

Despite extensive optical studies of moiré interference effects in TMD heterobilayers as in $MoSe_2$-WSe_2 [24], a consolidated picture of the rich and partly conflicting experimental features remains elusive [67]. The experiments report inconsistent results for peak energies of interlayer exciton PL [257, 258], g-factors [46, 258], and degree of polarization [46, 47], and even in the same sample the PL spectra can differ substantially from spot to spot [259]. The diversity of models invoked to explain the plethora of experimental signatures is not inherent to the theory of moiré excitons [59, 60, 130] but rather related to variations in actual real-world samples. For TMD bilayers with small twist angles away from parallel and antiparallel configurations, in particular, canonical moiré superlattices are known to transform into periodic domains of distinct atomic registries in triangular and hexagonal tiling [13, 14, 50, 51, 260], as dictated by the competition between intralayer strain and interlayer adhesion energies [48, 49, 52]. However, correlative studies of exciton features and reconstructed domains are mainly limited to twisted $MoSe_2$ homobilayers [13], providing only limited insight into exciton landscapes of mesoscopically reconstructed moiré heterostructures.

Here, we demonstrate theoretically and experimentally how atomic reconstruction in extended HBL samples with inhomogeneous strain and finite-size boundary conditions impacts the optical signatures of excitons. Driven by competition between intralayer strain and interlayer adhesion energy, energetically favored registries expand at the expense of unfavorable registries into periodic domains with areas inversely proportional to the twist angle θ. Theoretical and experimental results [48, 50] indicate for H-type HBLs that only the $\mathrm{H}_\mathrm{h}^\mathrm{h}$ stacking prevails in hexagonal domains after reconstruction, whereas $\mathrm{R}_\mathrm{h}^\mathrm{X}$ and $\mathrm{R}_\mathrm{h}^\mathrm{M}$ consolidate in tessellated triangular domains as two equally optimal registries in R-type heterostacks. Utilizing distinct PL characteristics of interlayer excitons in atomic registries of $MoSe_2$-WSe_2 HBLs calculated from DFT theory and summarized in Table 5.1, we infer the contribution from each domain present in the optical spot. By virtue of different spin-valley configurations, stacking symmetries and related degrees of interlayer coupling, R and H interlayer excitons exhibit distinct transition energies [45, 52, 60, 130], oscillator strengths [15, 45] and dipolar selection rules [60, 97, 130] accessible with optical spectroscopy. Moreover, magneto-luminescence experiments allow the assignment of interlayer exciton PL to domains of specific registries using

first-principles calculations of exciton Landé g-factors [45] and experimental values with sample-to-sample variations in the order of 10-20%.

5.2 Characteristics of $MoSe_2$-WSe_2 HBLs in H- and R-type stacking

Experimental studies were mainly performed on the sample based on CVD-grown MLs, we placed single-crystal $MoSe_2$ triangles on top of a large WSe_2 triangular ML by standard dry-transfer method [205, 261]. The resulting HBL triangles with small-twist H and R stacking configurations are delimited by dashed lines in the optical micrograph of the top panel in Figure 5.1a. We also prepared three additional samples fabricated from $MoSe_2$ and WSe_2 MLs exfoliated from native crystals as supplements. To access narrow exciton linewidths in cryogenic spectroscopy, all the HBLs were encapsulated in hBN.

The bottom panel of Figure 5.1a shows the characteristics of cryogenic PL recorded in the spectral bandwidth of interlayer excitons. The laterally extended maps recorded at 3.2 K show from left to right the integrated PL intensity and the degrees of its circular and linear polarizations, P_c and P_l, defined as the ratio of emission intensities $P = (I_{Co} - I_{Cross})/(I_{Co} + I_{Cross})$ detected in co-polarized (I_{co}) and cross-polarized (I_{cross}) configurations with a circularly (σ) or linearly (π) polarized excitation laser [262]. The PL map exhibits sizable intensity variations on micrometer scales across the H and R stacking regions, with an overall much brighter emission from R stacking, consistent with the reversed energetic ordering of singlet and triplet interlayer exciton states. Sizable variations in the PL intensity across a given stacking, on the other hand, could be attributed to sample imperfections yielding dark spots as regions of suppressed layer interactions. This scenario, however, conflicts with absorption characteristics of intralayer excitons in the regions of low PL with multi-peak resonances reminiscent of layer hybridization [19, 263]. Thus, sample imperfections alone are insufficient to explain the pronounced inhomogeneities in the PL map of Figure 5.1a.

The variations in PL intensity upon lateral displacement of the observation spot by a few microns are accompanied by changes in the spectral characteristics shown representatively in Figure 5.1b. In the upper right and lower left bright corners of H- and R-type triangles marked by diamonds, the respective red and orange PL spectra in Figure 5.1b feature only one peak at 1.40 eV and 1.32 eV, with highest degrees of circular polarization and opposite signs in the P_c map of Figure 5.1a. These spectral

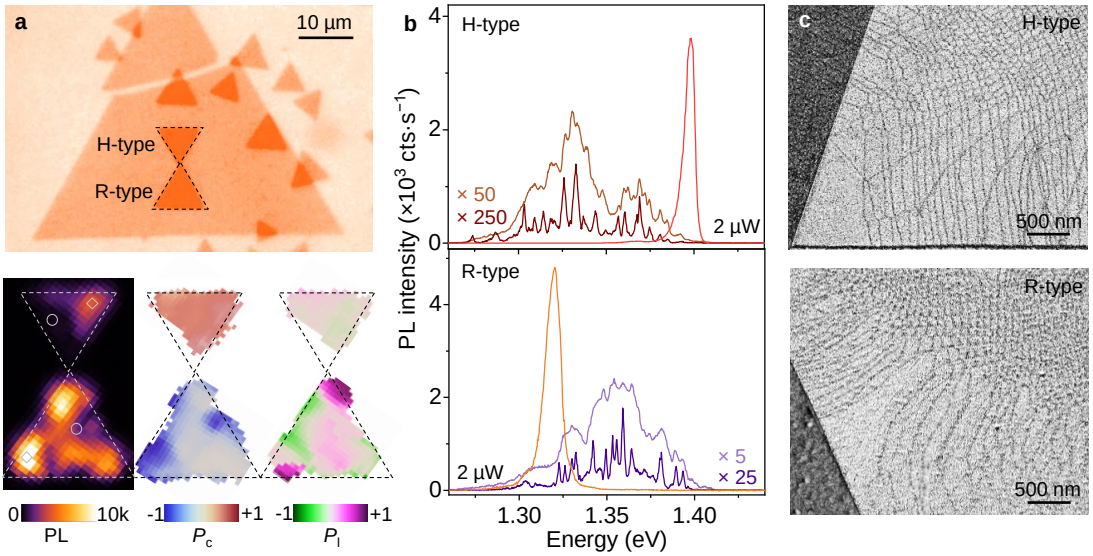

Figure 5.1: Characteristics of $MoSe_2$-WSe_2 HBLs in H- and R-type stacking. **a**, Top panel: Optical micrograph of sample 1 with H and R HBLs (indicated by dashed lines) obtained as stacks of CVD-grown $MoSe_2$ (small triangles) and WSe_2 (large triangle). Bottom panel, from left to right: Maps of interlayer exciton PL, degrees of circular and linear polarization, P_c and P_l. **b**, PL spectra in bright and dark spots marked by diamonds and circles in the map. Red and orange spectra are representative for regions with a single bright peak, whereas light brown and purple spectra (recorded at the same excitation power of 2 μW and scaled by 50 and 5) are characteristics of dark regions with broad and structured PL which evolves into narrow peaks (dark brown and purple spectra, scaled by 250 and 25) at low excitation with 0.01 μW. All spectroscopy data were recorded on sample 1. **c**, Scanning electron micrographs of H and R HBLs (top and bottom) recorded with secondary electron imaging.

signatures jointly suggest that both H and R triangles exhibit areas that can be at least as large as the optical spot yet entirely dominated by the respective triplet and singlet interlayer excitons in $\mathrm{H}_\mathrm{h}^\mathrm{h}$ and $\mathrm{R}_\mathrm{h}^\mathrm{X}$ registries. Given the finite twist angle in our sample, the absence of PL contributions from all other registries is striking.

The signatures of bright spots are contrasted on sample positions with low PL intensity, labelled by circles in the PL map and shown as brown and purple traces in Figure 5.1b. At the expense of simple single-peak spectra, the PL is structured and spectrally dispersed over 100 meV on the low and high energy sides of the solitary peaks of triplet $\mathrm{H}_\mathrm{h}^\mathrm{h}$ and singlet $\mathrm{R}_\mathrm{h}^\mathrm{X}$ interlayer excitons. On dark spots and under identical excitation conditions, the integrated PL is typically much lower (note the scaling factor of 50 and 5 for H- and R-type spectra), and P_c is reduced in its absolute

value though preserved in sign. These characteristics, indicative of moiré effects [47, 259], evolve into a series of spectrally narrow peaks at reduced excitation powers, signifying interlayer exciton localization in moiré quantum dots [46, 259]. This scenario of energy-reducing moiré pockets in H-type HBL is in stark conflict with quantum-dot features on the high energy side of $\mathrm{R}_{\mathrm{h}}^{\mathrm{X}}$.

Additional confusion arises from the observation of finite degree of linear polarization with variations across the P_l map of Figure 5.1a. According to Table 5.1, the dipolar selection rules of spin-valley specific states of KK interlayer excitons dictate valley contrasting circularly polarized optical transitions perpendicular to the HBL plane as well as z-polarized in-plane transitions [P2, 60, 130]. Whereas the former constitute predominantly positive and negative degree of circular polarization (P_c) values of H- and R-type stackings in the map of Figure 5.1a, the latter should exhibit neither circular nor linear degrees of polarization when probed in black-scattering configuration. In contrast to this expectation, the degree of linear polarization (P_l) map of Figure 5.1a features regions with high degrees of linear polarization (note the upper and lower left corner of the R-type triangle), reminiscent of uniaxially strained moiré landscapes [54] or HBL samples with transfer-induced layer corrugation [264]. This observation implies the presence of moiré quantum

Table 5.1: Theoretical parameters of interlayer excitons in distinct atomic registries of $MoSe_2$-WSe_2 HBLs. Transition energy (in eV, estimated from Ref. [52]), oscillator strength (proportional to the square of dipole moment $|\boldsymbol{\mu}|$ in Debye), polarization selection rule and g-factor for zero-momentum KK or $K'K$ interlayer excitons in R- and H-stacking in spin-singlet (electron and hole with antiparallel spin) and spin-triplet (electron and hole with parallel spin) configurations. Note that singlet (triplet) interlayer excitons are the lowest-energy states in R (H).

	Singlet				Triplet			
Stacking	Energy	$\lvert\boldsymbol{\mu}\rvert$	Polar.	g-factor	Energy	$\lvert\boldsymbol{\mu}\rvert$	Polar.	g-factor
R_h^X (optimal)	1.33	1.47	σ^-	$+5.8$	1.35	0.70	σ^+	-10.5
R_h^h	1.38	2.06	σ^+	-6.4	1.40	0.19	z	11.0
R_h^M (optimal)	1.48	1.09	z	6.3	1.50	0.02	σ^-	$+10.9$
H_h^M	1.39	0.40	z	13.1	1.37	0.10	σ^-	$+17.6$
H_h^X	1.41	0.69	σ^+	-13.2	1.39	0.40	z	17.7
H_h^h (optimal)	1.42	2.14	σ^-	$+12.9$	1.40	0.42	σ^+	-17.6

wires in our sample.

The key to the understanding of such drastic spatial variations in the PL characteristics of interlayer excitons is provided by mesoscopic reconstruction. To visualize the phenomena of micron-scale reconstruction in our samples, we performed secondary electron imaging in scanning electron microscopy (SEM) [14]. The respective SEM images of H- and R-stacked HBL near the triangle tip and edge, shown in the top and bottom panels of Figure 5.1c with stacking-sensitive contrast, provide evidence for the formation of large domains of one atomic registry separated by thin lines of domain walls. The domain networks observed in different samples exhibit common patterns on the mesoscopic scales: large, micron-sized 2D domains at HBL tips and edges are surrounded by elongated 1D stripes that merge in the sample core into a network of finely structured domains with dimensions well below 100 nm, forming quasi zero-dimensional (0D) arrays with hexagonal and triangular tiling for H and R stackings.

All the above features manifest consistently across all samples of our studies shown in Figure 5.2. Despite different geometries, all samples show two common features. First, aligned R-type HBLs are generally brighter than their H-type counterparts (as in sample 1 and 2 with nearly aligned R- and H-type HBLs), consistent with a factor of 10 difference in oscillator strengths of the respective spin-singlet and triplet interlayer exciton transitions. Second, all four samples exhibit substantial variations in PL intensity on micron scales across H- and R-type regions despite rather clean interfaces with only few interfacial bubbles. Moreover, spots of bright interlayer exciton PL are predominantly observed near HBL tips and edges, whereas sample cores are relatively dark. Based on observations in SEM and our reconstruction model, we interpret these spatial variations as arising from mesoscopic domain networks with extended 2D domains, 1D stripes and 0D domain arrays.

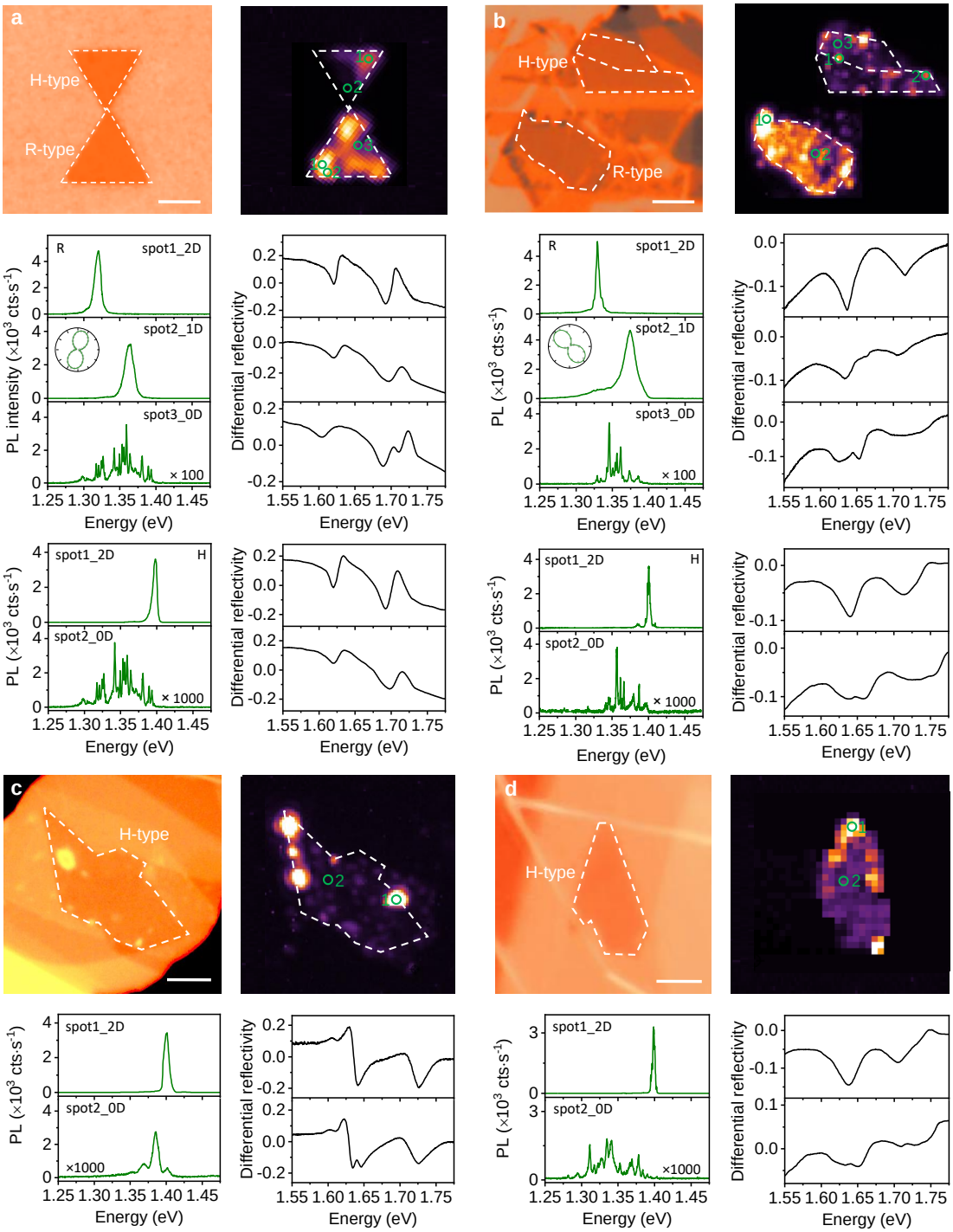

Figure 5.2: Overview of hBN-encapsulated $MoSe_2$-WSe_2 HBL samples. **a-d** Top panels, optical micrographs (left) and PL intensity maps at 3.2 K within the interlayer exciton emission excited with a laser at 725 nm and 2 μW power (right). Scale bars: 4 μm for samples $1-3$ in **a-c** and 2 μm for sample 4 in **d**. **a-d** Bottom panels, PL from selected spots (left) and corresponding DR (right). For regions assigned to 1D stripes, the orientation of linearly polarized PL is specified by the insets. For 0D arrays, additional spectra at 0.01 μW excitation power are shown and scaled for better visibility (factors of 100 for R-type, 1000 for H-type).

The cryogenic PL and DR of the positions representative of 2D domains, 1D stripes and 0D domain arrays in each sample are shown in Figure 5.2. Note that the signatures of 1D stripes with a high degree of linear polarization were observed only in R-type HBLs (sample 1 and 2 in Figure 5.2a and b, respectively). Bright PL spots were consistently observed near line defects such as cracks and edges, whereas dark PL regions dominate the sample cores. In H-type samples, the PL characteristics of dark regions differ for nearly-aligned samples (samples 1, 2 and 4) and the sample with a twist angle of $\sim 3°$: Whereas the former exhibit quantum dot type features of localized excitons, the latter shows consistent exciton-polaron characteristics on different sample positions. The DR spectra of intralayer excitons in Figure 5.2, which probe the evolution of intralayer exciton absorption as the observation spot is displaced from bright to dark PL areas. Upon displacement, the DR resonances of intralayer excitons at 1.64 and 1.71 eV on bright spots (top spectrum) gradually develop into two well-resolved resonances and a broadening around $MoSe_2$ and WSe_2 intralayer exciton transitions which become most pronounced in the darkest areas (bottom spectrum). This evolution reflects the presence of only one registry in bright spots and modulation of the intralayer exciton energy by alternating stackings in dark-most spots. This splitting of intralayer exciton transitions is not to be confused with band hybridization effects in homobilayers [13, 14] or heterobilayers with near-resonant conduction [263] or valence [19] bands. As resonant hybridization in $MoSe_2$-WSe_2 heterostacks is strongly inhibited by large band offset, multi-peak DR spectra result from different intralayer exciton energies within the different registries present in the optical spot, convincingly assigning sample areas with dark PL to areas of 0D arrays and not to regions of local layer-separating imperfections such as bubbles or folds.

5.3 Model of mesoscopic reconstruction

The mesoscopic reconstruction is driven by the interplay of intralayer strain and interlayer adhesion energy. Recent theoretical work [48, 49, 52] pointed out that moiré lattices of marginally twisted or incommensurate bilayers relax on the nanoscale into periodic domains by rearranging lattice atoms in each layer according to a vectorial 2D displacement field that overcompensates the associated strain cost by the gain in interlayer adhesion. To provide intuition for the domain formation on scales ranging from a few nanometers to a few microns, we adopt the theoretical model of lattice reconstruction [49] and account for finite-size effects as well as

singular point rotations that can grow to large-area 2D domains of optimal stacking. In brief, we model the tip of a marginally twisted HBL by an equilateral triangle with micron-sized base connecting to the rest of the HBL triangle with ideal moiré periodicity. On the line bisecting the triangular tip into two equal halves, we place a point of zero-twist deformation to create an initial lattice displacement field which is modified in consecutive iterations to obtain a stacking configuration from the final displacement field that minimizes the sum of intralayer strain and interlayer adhesion energies in the tip area. This procedure yields series of reconstructed landscapes, characterized by their respective initial displacement fields.

The results of our numerical simulations are shown in Figure 5.3a and d for R- and H-type HBLs with a twist angle of $\theta = 0.4°$. The two topmost maps illustrate the ideal moiré and periodically reconstructed patterns. The four maps below show reconstruction patterns obtained after optimization of initial displacement fields that untwist the HBL around a rotation center indicated by black points and labeled by a dimensionless coordinate $\alpha = 1, 0.5, 0.25, 0$. In all cases, optimization yields mesoscopic reconstruction into large 2D domains of energetically favored stackings at the triangle tip ($\mathrm{R}_\mathrm{h}^\mathrm{X}$ or $\mathrm{R}_\mathrm{h}^\mathrm{M}$ and $\mathrm{H}_\mathrm{h}^\mathrm{h}$ in R- and H-type HBLs) with characteristic domain sizes on the micron scale and orders of magnitude lager areas than in periodically reconstructed lattices. The extended domains are flanked by 1D stripes which merge into 0D domain arrays. These different domain types and length scales predicted by our model comply with the global reconstruction picture observed experimentally in SEM images as in Figure 5.1c, suggesting that mesoscale domain formation is the most favorable at sample edges.

As expected, optimality reconstructed patterns minimize the total energy of the system according to our simulation results shown in Figure 5.3b and c for R-type and Figure 5.3e and f for H-type HBLs. For $\theta = 0.4°$, the total energy (normalized by the triangle area) in both stackings is reduced by a factor of 10 and 2 below the energies of ideal moiré and periodic limits (solid lines in Figure 5.3b and e upon reconstruction after optimal rotation at $\alpha = 0$. The global energy minimum, obtained for the rotation point at the borderline between the HBL moiré core and the triangle base, features the most direct transition from 2D domain through 1D stripes to the core. As the rotation point is moved towards the tip (via $0 < \alpha < 1$), 0D regions emerge at the border and the energy gain decreases, passing the threshold of periodic reconstruction at $\alpha \cong 0.5$ (0.75) in R (H) twisted HBL but remaining well below the moiré lattice energy throughout. Remarkably, for the optimally relaxed tip around $\alpha = 0$, mesoscopic reconstruction remains energetically favorable for twist angles up to $\theta = 3°$ for both

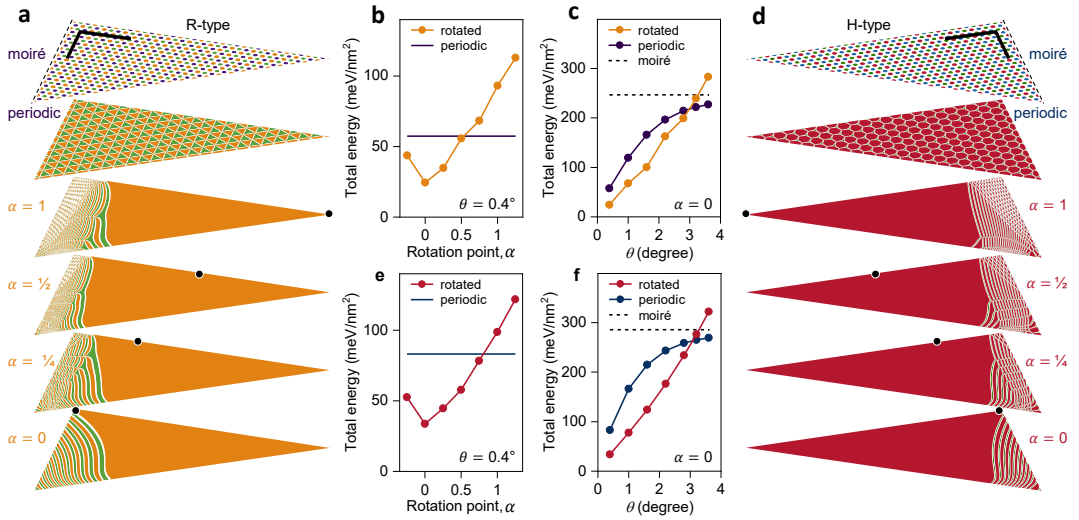

Figure 5.3: Mesoscopic reconstruction in finite-size simulations. **a** and **d**, Maps of reconstructed domains in triangular tips of R and H HBLs with a twist angle $\theta = 0.4°$ (only triangle halves are shown in the projections; the scale bars are 200 nm). The topmost maps show moiré patterns without reconstruction, delimited by dashed lines from the moiré core of the HBL. The maps below show periodic reconstruction and mesoscopically reconstructed domain patterns obtained for different zero-twist deformations around points marked by black dots at dimensionless positions α (note that orange R_h^X and green R_h^M domains can interconvert because of same adhesion energy [49]). **b** and **e**, Total areal energy for R and H at $\theta = 0.4°$ and different untwisting points α (the energy of the respective periodic patterns is shown by solid lines). **c** and **f**, Total areal energy of periodic and optimally reconstructed (for $\alpha = 0$) patterns for different twist angles θ in R and H (the energy of the respective moiré patterns is shown by dashed lines).

stacking (Figure 5.3e and f), in accord with the recent Raman spectroscopy results [265]. Detailed calculations shown in supplementary information of manuscript [P2].

With this intuition for mesoscopic reconstruction from theory and SEM experiment, we revisit the main spectroscopic features of distinct sample regions in R- and H-stacking to provide a unifying interpretation of diverse optical signatures observed in $MoSe_2$-WSe_2 HBLs.

5.4 Spectral characteristics of excitons in reconstructed domains

5.4.1 Degree of polarization and g-factor in R-type

Bearing in mind the absence of peak multiplicity in the DR spectra of bright spots, the corresponding characteristics of interlayer exciton PL in Figure 5.4a are straightforwardly explained. Due to complete local reconstruction into domains exceeding the optical spot size, only lowest-energy spin-singlet excitons of $\mathrm{R}_\mathrm{h}^\mathrm{X}$ registry with sizable oscillator strength contribute to PL (top panel) with a single peak at 1.32 eV and FWHM linewidth of 6 meV, negative P_c (Figure 5.4b) and a positive g-factor ~ 6.9 (bottom panel) shown in Figure 5.4c in agreement with previous report for aligned HBLs [257]. Such characteristics are frequently observed at sample edges and tips (as in Figure 5.1a) where large-scale reconstruction is energetically most favorable (as in reconstructed maps of Figure 5.3a).

The PL emission from spatially neighboring regions exhibits blue-shifted emission around 1.36 eV paired with a high degree of linear polarization in Figure 5.5a and vanishing P_c as well as g-factor values in Figure 5.5b and c, which are indicatives of quantum wires [54]. As suggested by our theory, these quantum wires are formed by alternating optically bright $\mathrm{R}_\mathrm{h}^\mathrm{X}$ and dark $\mathrm{R}_\mathrm{h}^\mathrm{M}$ domains. This 1D confinement not only breaks the threefold rotational symmetry of the exciton wave functions, thereby admixing K and K' valleys and obliterating both P_c and g-factors in perpendicular magnetic field, it is also responsible for the blue-shift in the PL energy as a consequence of quantum confinement of interlayer exciton states in stripes of lower-energy $\mathrm{R}_\mathrm{h}^\mathrm{X}$ domains flanked by potential walls of higher-energy $\mathrm{R}_\mathrm{h}^\mathrm{M}$ states. Spot-to-spot variations in the PL characteristics of sample regions with high P_l and varying orientations of the respective polarization axes are consistent with the diversity in stripe geometries observed both in SEM and our mesoscale reconstruction model. A prominent example is the left corner of the R-type triangle in Figure 5.1a where the bright spot of a large $\mathrm{R}_\mathrm{h}^\mathrm{X}$ domain with $P_\mathrm{c} \simeq -1$ is encompassed by regions with $P_\mathrm{l} \simeq \pm 1$ stemming from quantum wire ensembles with nearly orthogonal orientation.

Quantum confinement is also prominent in R-type regions of 0D arrays with much reduced PL intensity and spectrally narrow lines of quantum dots at low excitation power (note the scaling factors of 5 and 25 for the spectra at 2 and 0.01 μW excitation

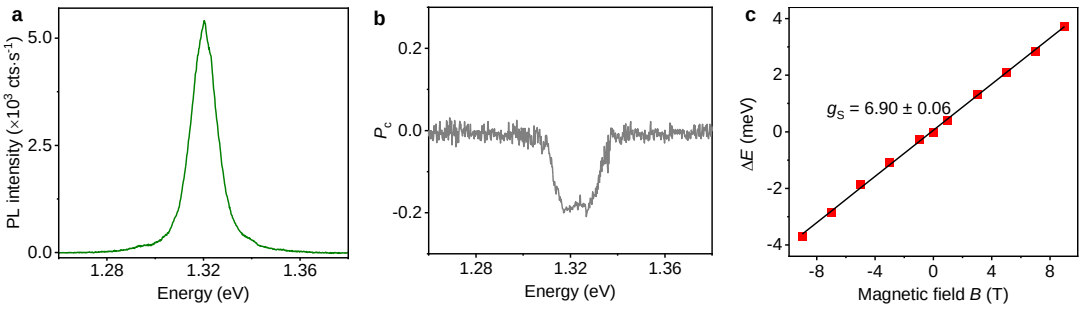

Figure 5.4: a, PL of interlayer exciton in a R-type bright spot with emission around 1.32 eV. **b**, Valley polarization of interlayer exciton under σ^+ excitation at 0 T. **c**, Valley Zeeman splitting ΔE as a function of magnetic field. The solid lines are linear fits to the data with g-factors and error bars obtained from least-square best fits. All data were recorded with excitation powers of 20 μW.

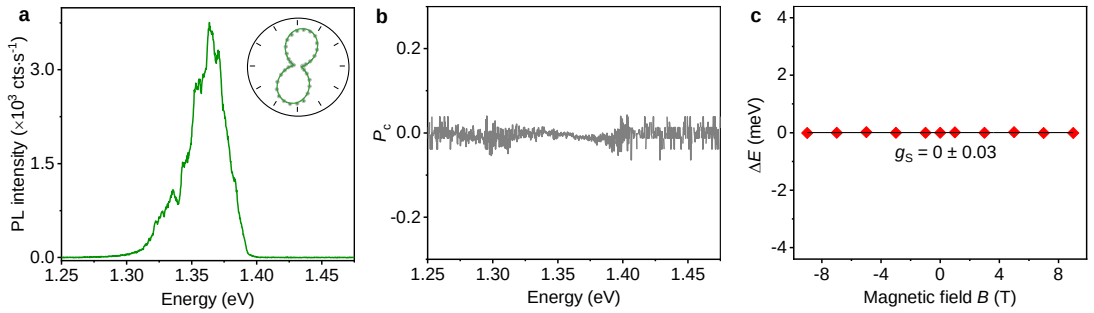

Figure 5.5: a, Interlayer exciton PL in R-type bright regions with emission around 1.36 eV and degree of linear polarization inset, corresponding to regions with 1D stripes. **b**, Degree of circular polarization P_c. **c**, Valley Zeeman splitting ΔE as a function of magnetic field. The solid lines are linear fits to the data with g-factors and error bars obtained from least-square best fits. All data were recorded with excitation powers of 20 μW.

powers in Figure 5.6a) with characteristic negative P_c (Figure 5.6b) and positive g-factors of 6.8 (Figure 5.6c). Depending on the actual sample spot of dark PL, such quantum dot lines with a FWHM well below 1 meV can be observed within spectrally broad or narrow windows of 100 and 10 meV (as in Figure 5.6a and d, respectively) energetically above the single peak of extended R_h^X domains at 1.32 eV. These blue-shifts are in stark contrast to the common notion of exciton localization in energy-reducing moiré potentials [46, 47]. In fact, regions of 0D reconstructed arrays increase the energy of interlayer excitons by quantum confinement in triangular boxes of R_h^X stacking with potential barriers formed by adjacent R_h^M triangles. Unlike in

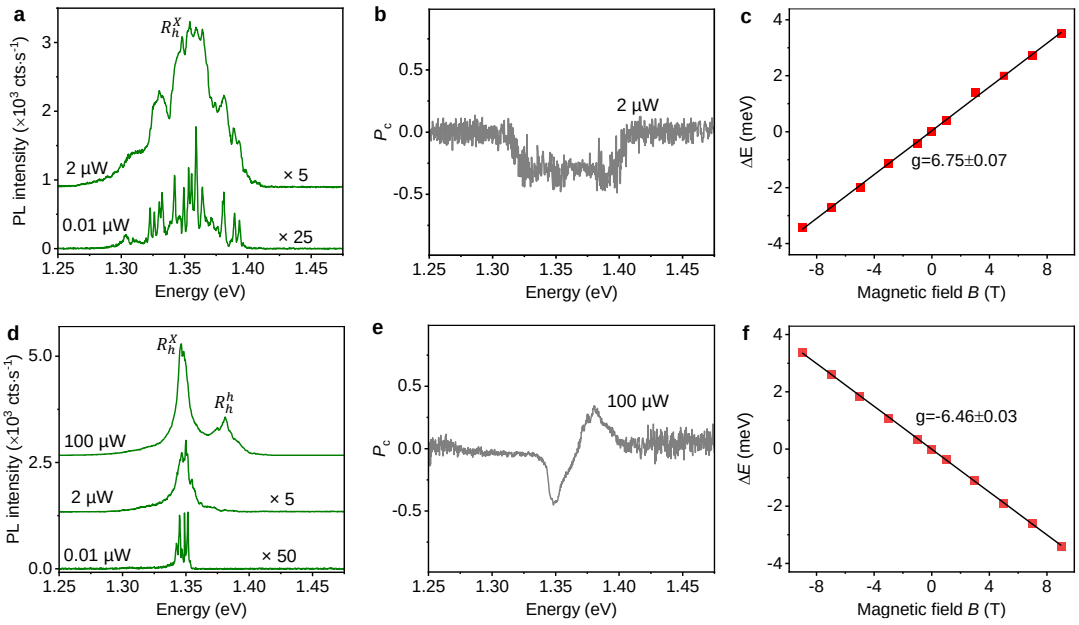

Figure 5.6: a-c, Broad interlayer exciton PL, degree of circular polarization P_c and Valley Zeeman splitting ΔE as a function of magnetic field B in a dark sample region with 0D domains. **d-f**, Narrow interlayer exciton PL, P_c and dispersion in perpendicular magnetic field B (shown with offsets and different scaling for excitation powers of 100, 2 and 0.01 μW).

ideal moiré patterns, the potential boundaries in periodically reconstructed R-type arrays are steep, and the variations in the quantum dot PL energies reflect different strengths of confinement in quantum boxes of varying size in the triangular tiling.

Since the optical spot samples a large number of non-identically reconstructed arrays, the PL from quantum-confined interlayer excitons is spectrally dispersed and merges at higher excitation powers into structured PL peaks of sub-ensembles grouped by similar characteristic scales. Periodically reconstructed 0D arrays with lateral homogeneity on the scale of the optical spot give rise to a narrow ensemble of similar emission energies (within 10 meV as in Figure 5.6d recorded on Sample 2) which allow to observe a hot luminescence peak with positive P_c and negative g-factor of -6.5 (Figure 5.6e and f at 100μW excitation power). These features, absent in the spectra of 1D and 2D domains, correspond to spin-singlet states of interlayer excitons in R^h_h stacking ~ 50 meV above R^X_h states with similar oscillator strength. Such a prominent contribution of R^h_h stacking to the PL is surprising as theoretical considerations predict vanishingly small point-like areas for this non-optimal stacking [48, 49, 52]. Recent experiments observed related PL features of R^h_h energetically

below R_h^X exciton emission in $MoSe_2$-WSe_2 HBLs with a twist angle of $4°$ [45] where piezo- and ferroelectric effects are predicted to swap the energetic ordering of R_h^h and R_h^X exciton states [52]. However, in all present considerations of reconstruction [48, 49, 52], R_h^h domains are predicted to exhibit vanishingly small areas, such that sizable PL with R_h^h characteristics from small-twist $MoSe_2$-WSe_2 HBLs implies either areas of R_h^h domains that are larger than anticipated from theory, or strongly imbalanced exciton population feeding of R_h^h and R_h^X states via polarization-contrasting relaxation pathways.

5.4.2 Degree of polarization and g-factor in H-type

Despite many similarities, the picture of mesoscopic reconstruction in H-type $MoSe_2$-WSe_2 HBLs and the consequences for local optical properties is different and thus requires a dedicated consideration.

The atomic registry of large-scale reconstructed 2D domains is H_h^h, unrivaled by other registries in terms of energy-optimizing stacking [48, 49, 51]. Thus, the respective PL spectrum of interlayer excitons (Figure 5.7a) is rather simple, featuring only the emission peaks of spin-triplet and spin-singlet configurations with respective positive and negative P_c values (Figure 5.7b) and g-factors of -16.4 and 12.3 (Figure 5.7c) [155, 257, 266]. In agreement with our reconstruction model, such characteristics were observed in the top-right corner of the H-type triangle in Figure 5.1a and at HBL edges of other samples prone to reconstruction. Note that the double-peak PL structure of H_h^h reconstructed domains has no counterpart in the R_h^X case (Figure 5.4a) due to reversed energetic ordering of singlet and triplet states: despite a factor of 25 smaller oscillator strength estimated from Table 5.1, the PL from lower-energy spin-triplet exciton transition in H_h^h is two orders of magnitude brighter than the hot-luminescence from spin-singlet state due to thermal population imbalance dictated by the spin-orbit splitting of 25 meV.

In the respective PL spectra (Figure 5.8a) we again observe for low and moderate excitation powers (0.01 and 2 μW) that sharp quantum dot peaks develop into a multi-peak ensemble spectrum characteristic of 0D domain arrays with an inhomogeneous size distribution of hexagonal domains in optimal H_h^h stacking illustrated in Figure 5.3d. The positive degree of circular polarization (Figure 5.8b) and the g-factor values (Figure 5.8c) confirm the H_h^h stacking as the origin of the quantum-dot PL. For this stacking, theoretical estimates place its optically bright interlayer exciton states at the top of the energy hierarchy, well above optically dark

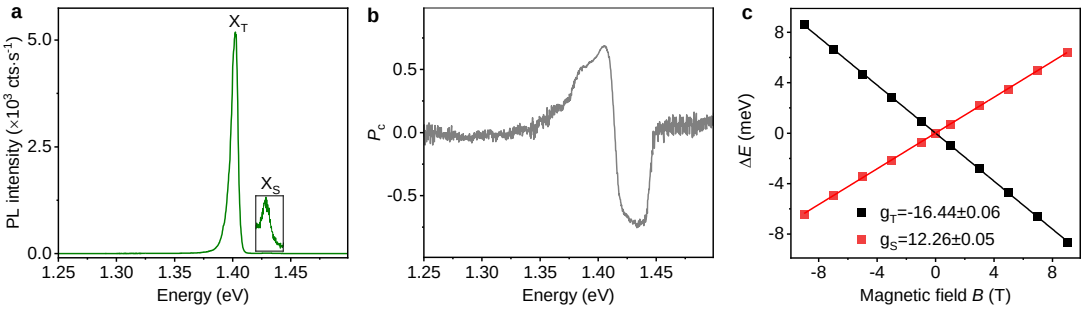

Figure 5.7: a, PL of interlayer exciton in a H-type bright spot with emission above 1.40 eV. **b**, Valley polarization of interlayer exciton under σ^+ excitation at 0 T. **c**, Valley Zeeman splitting ΔE as a function of magnetic field. The solid lines are linear fits to the data with g-factors and error bars obtained from least-square best fits. All data were recorded with excitation powers of 20 μW.

$\mathrm{H}_\mathrm{h}^\mathrm{M}$ and $\mathrm{H}_\mathrm{h}^\mathrm{X}$ states.

This energetic ordering of interlayer excitons in H stacking is responsible for the absence of PL characteristics ascribed to stripes in R-type HBLs: Excitons in reconstructed $\mathrm{H}_\mathrm{h}^\mathrm{h}$ domains are not bound by potential barriers that would mix K and K' states as in 1D quantum wires of R-type samples (note the absence of areas with high degree of in-plane linear polarization throughout the P_l map of H-type triangles in Figure 5.1a). This is contrasted by reports of quantum wire signatures in H-type stacks subjected to sizable uniaxial tensile strain [54] which could give rise to reversal of energetic ordering of interlayer excitons in different atomic registries of H-type stacking, facilitating quantum wire formation similar to R-type heterostructures. In the absence of such strain-induced effects, our theory predicts that reconstructed $\mathrm{H}_\mathrm{h}^\mathrm{h}$ domains preserve exciton population on spatially extended optically bright plateaus, whereas in regions of 0D arrays the PL intensity decreases (note the scaling factors of 50 and 500 in Figure 5.8a) due to population drain into lower-energy valleys of the surrounding $\mathrm{H}_\mathrm{h}^\mathrm{M}$ and $\mathrm{H}_\mathrm{h}^\mathrm{X}$ domain network with much reduced optical activity of vanishingly small domain areas. Consistently, nanoscale domain formation in regions of 0D arrays is accompanied by size-dependent PL red-shifts of up to 100 meV below the $\mathrm{H}_\mathrm{h}^\mathrm{h}$ triplet peak at 1.4 eV.

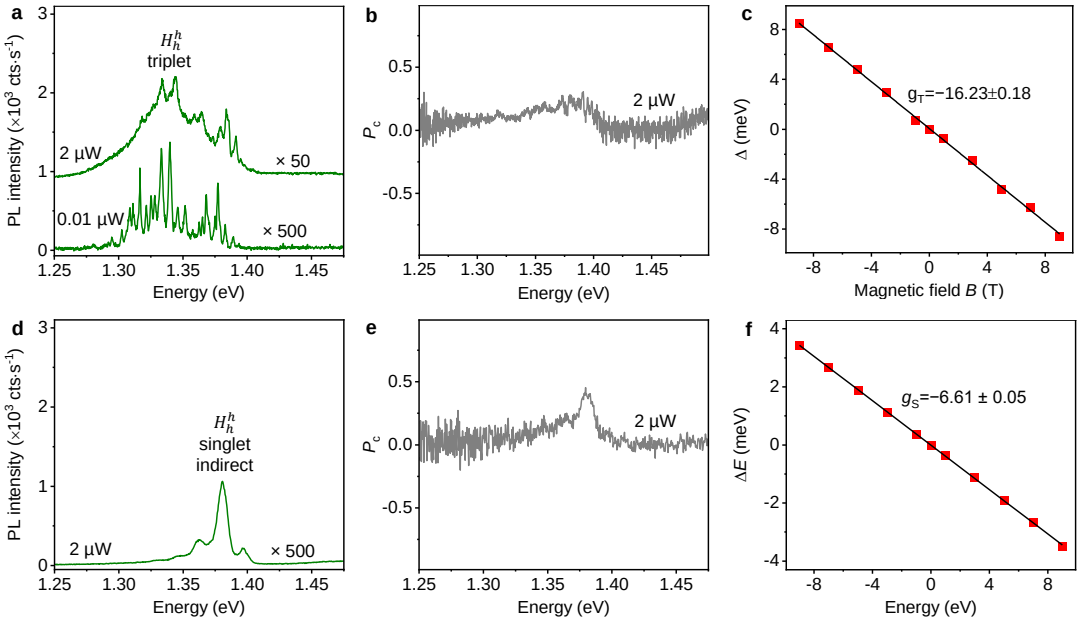

Figure 5.8: a-c, Interlayer exciton PL, degree of circular polarization P_c, and Valley Zeeman splitting ΔE as a function of magnetic field in a H-type dark spot. **d-f**, Interlayer exciton PL, P_c, and Valley Zeeman splitting ΔE as a function of magnetic field in a H-type dark area from sample 3 about 3° twist.

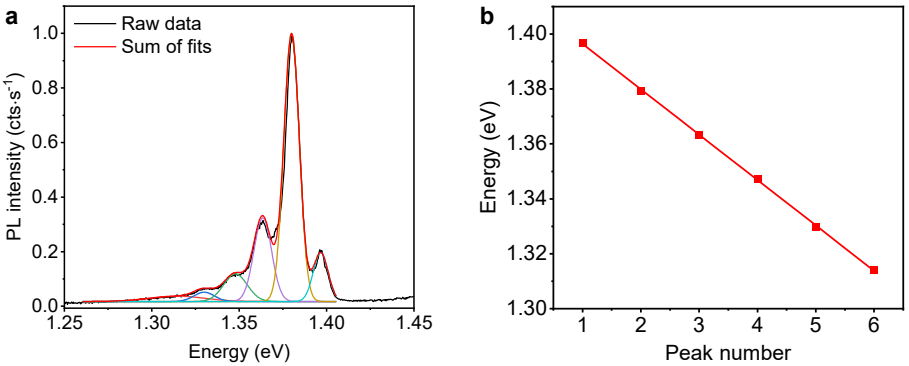

Figure 5.9: a, Representative PL spectrum from a dark region in H-type HBL moiré superlattice with 3° twist angle. In contrast to 0D arrays of nearly-aligned samples, the spectrum is characterized by a series of six peaks shown together with Gaussian fits. **b**, Energy of six Gaussian peaks in a plotted as a function of the peak number. The linear fit indicates equidistant peak spacing of 16 meV.

		R-type			H-type		
Exciton	Spin configuration	R_h^X	R_h^h	R_h^M	H_h^M	H_h^X	H_h^h
$K'K$ (KK)	singlet	13.1	13.0	13.0	6.5	6.4	5.7
$K'K$ (KK)	triplet	17.8	17.6	17.6	11.1	11.0	10.4
QK	singlet	8.6	9.0	8.7	10.4	10.0	9.6
QK	triplet	13.0	13.3	12.9	13.9	13.6	13.2
$Q'K$	singlet	10.6	10.7	11.0	10.3	10.5	10.0
$Q'K$	triplet	14.9	15.0	15.3	13.8	14.2	13.7
$K\Gamma$	singlet	4.0	3.6	3.7	3.0	3.1	3.3
$K\Gamma$	triplet	0.7	1.0	1.0	7.6	7.6	7.9
$K'\Gamma$	singlet	3.3	3.0	3.0	3.6	3.6	3.9
$K'\Gamma$	triplet	8.0	7.6	7.7	1.0	0.9	0.7
$Q\Gamma$	singlet	1.1	1.0	1.3	0.3	0.1	0.0
$Q\Gamma$	triplet	3.2	3.3	2.9	3.8	3.5	3.6
$Q'\Gamma$	singlet	0.8	0.7	1.1	0.2	0.5	0.4
$Q'\Gamma$	triplet	5.1	5.0	5.3	3.7	4.1	4.0

Table 5.2: Landé g-factor values of momentum-indirect interlayer excitons in R- and H-type HBL calculated from DFT. We restrict the table to lowest-energy interlayer exciton states formed between conduction band electrons in K, K', Q or Q' valleys of $MoSe_2$ and valence band holes at K in WSe_2 or at Γ in the hybrid band of $MoSe_2$-WSe_2 according to the electronic band structure [15]. For each state, the absolute g-factor values of both singlet and triplet spin configurations are listed for distinct atomic registries. Note that due to different symmetry in R- and H-type $MoSe_2$-WSe_2 HBLs, the spin-valley configurations are distinct [97]: In R-type (H-type), KK ($K'K$) interlayer exciton states are momentum-direct with lowest energy states in singlet (triplet) configuration, whereas $K'K$ (KK) states are momentum-indirect with triplet (singlet) lowest-energy states.

For completeness, we show the PL characteristics of a dark area in an H-type sample of about 3° in Figure 5.8d-f. The heterostack is not entirely prone to reconstruction, with tips and edges exhibiting signatures of bright H_h^h domains. However, the dark areas of the sample exhibit very different features than reconstructed 0D arrays, implying that the HBL largely maintains its moiré structure. The PL at 2 μW excitation power is reduced by another factor of 10 (note the scaling factor of 500 in Figure 5.8d), with positive P_c (Figure 5.8e) and negative g-factor of -6.6 (Figure 5.8f) that has no counterpart in the realm of zero-momentum $K'K$ interlayer excitons of H-type registries yet is characteristic of finite-momentum KK

exciton states as shown in Table 5.2. The peaks with equidistant energy spacing of 16 meV up to 6th order (see Figure 5.9) are indictive of interlayer exciton-polaron formation [267]. In this regime, the heterostructure with layer and valley-separated excitons dressed by strong exciton-phonon coupling is momentum-dark, with population decay of exciton-polaron states mediated by a series of phonon replica in luminescence.

5.4.3 Exciton decay dynamics

The PL decay of interlayer excitons in different domain types was studied with time-resolved PL spectroscopy shown in Figure 5.10 and Table 5.3 for an excitation power of 0.05 μW at 725 nm excitation wavelength. The set of data is complemented by power-dependent lifetime measurements of $\mathrm{R}_\mathrm{h}^\mathrm{X}$ singlet and $\mathrm{H}_\mathrm{h}^\mathrm{h}$ triplet interlayer excitons in Figure 5.11. Focusing first on reconstructed 2D domains, where interlayer exciton reservoirs are limited to zero-momentum and momentum-dark exciton states in $\mathrm{H}_\mathrm{h}^\mathrm{h}$ and $\mathrm{R}_\mathrm{h}^\mathrm{X}$ registries due to the absence of other stackings, we determine from best-fit analysis (taking into account the instrument response function) two decay channels for the $\mathrm{H}_\mathrm{h}^\mathrm{h}$ singlet exciton and three decay channels for both the $\mathrm{H}_\mathrm{h}^\mathrm{h}$ triplet and $\mathrm{R}_\mathrm{h}^\mathrm{X}$ singlet excitons. According to Table 5.3, the $\mathrm{H}_\mathrm{h}^\mathrm{h}$ singlet PL is characterized by two decay times - one below the resolution limit of 0.2 ns and one with a decay time of 2.5 ns. We ascribe the primary decay time to population loss of $\mathrm{H}_\mathrm{h}^\mathrm{h}$ singlet excitons by rapid relaxation into the energetically lower reservoir of $\mathrm{H}_\mathrm{h}^\mathrm{h}$ triplet excitons and other non-radiative decay processes including Auger-mediated population loss. The secondary decay channel with 2.5 ns decay time reflects the characteristic lifetime of $\mathrm{H}_\mathrm{h}^\mathrm{h}$ singlet interlayer exciton state which is proportional to the oscillator strength of the respective radiative transition.

Domain	Stacking	Spin config.	τ_1	A_1	τ_2	A_2	τ_3	A_3
2D	R_h^X	singlet	1.1 ns	34%	5 ns	30%	45 ns	36%
1D	R_h^X	singlet	1.5 ns	25%	13 ns	37%	70 ns	38%
0D	R_h^X	singlet	2.2 ns	32%	34 ns	40%	335 ns	28%
2D	H_h^h	singlet	< 0.2 ns	98%	2.5 ns	2%		
2D	H_h^h	triplet	2.4 ns	29%	48 ns	24%	440 ns	47%
0D	H_h^h	triplet	1.7 ns	52%	29 ns	22%	305 ns	26%

Table 5.3: Best-fit parameters obtained for the data in Figure 5.10 using tri-exponential decay with characteristic lifetime (τ_i) and amplitude (A_i) of each decay channel.

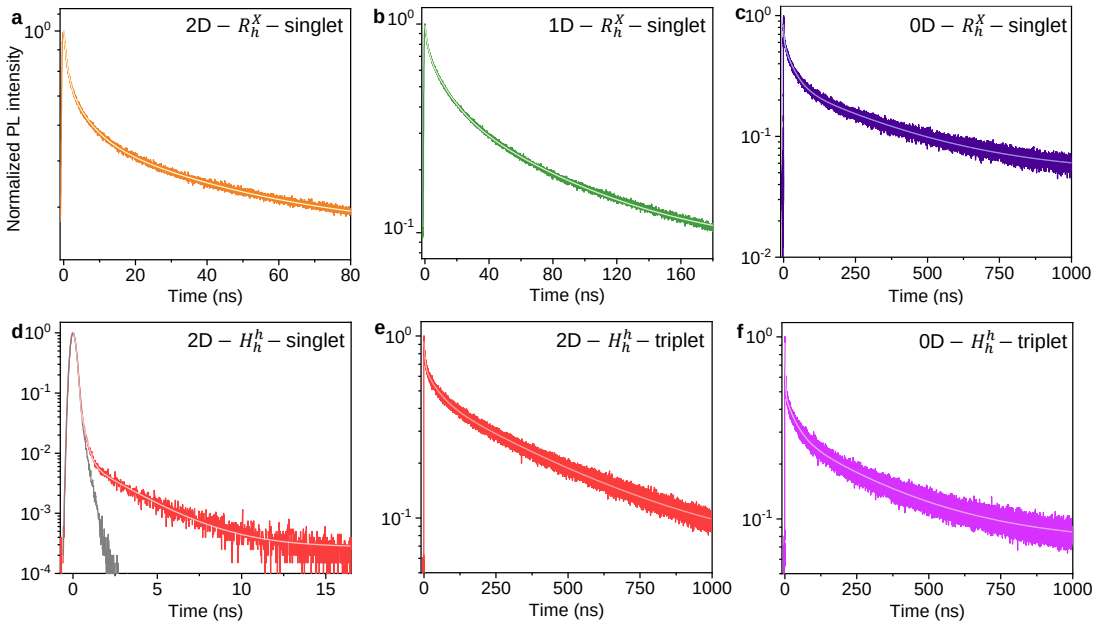

Figure 5.10: Time-resolved PL of interlayer excitons in different types of domain. **a-c**, Time-resolved PL decay of $\mathrm{R_h^X}$ singlet exciton in a 2D domain, regions of 1D stripes and 0D arrays. **d-f**, Time-resolved PL decay of $\mathrm{H_h^h}$ singlet exciton and triplet exciton in a 2D domain region, as well as $\mathrm{H_h^h}$ triplet exciton in a 0D domain region. The instrument response function (IRF) is shown in **d** in gray. The solid lines show in each panel best fits to the data obtained by a convolution of the IRF and a tri-exponential decay.

Using 2.5 ns as the radiative lifetime of the $\mathrm{H_h^h}$ singlet exciton reservoir, we estimate by scaling of oscillator strengths from Table 5.1 the radiative PL lifetimes of 65 ns for the $\mathrm{H_h^h}$ triplet interlayer exciton reservoir, as well as 5.3 and 23 ns for the $\mathrm{R_h^X}$ singlet and triplet exciton reservoirs, respectively. Experimentally, the secondary decay component of the $\mathrm{H_h^h}$ triplet reservoir and the $\mathrm{R_h^X}$ singlet reservoir are determined to 48 ns and 5 ns, respectively, in good agreement with the scaling anticipated from theory, whereas the PL from the $\mathrm{R_h^X}$ triplet state is insufficient for time-resolved measurements. The contribution of Auger decay to the primary decay channel is evident for the $\mathrm{H_h^h}$ triplet and $\mathrm{R_h^X}$ singlet PL decay from power-dependent data in Figure 5.11, where the amplitude of the primary component dominates at high excitation powers over the amplitudes of the two complementary channels with power-independent ratio.

With this assignment of primary and secondary PL decay components to non-radiative population loss processes (including Auger) and radiative decay,

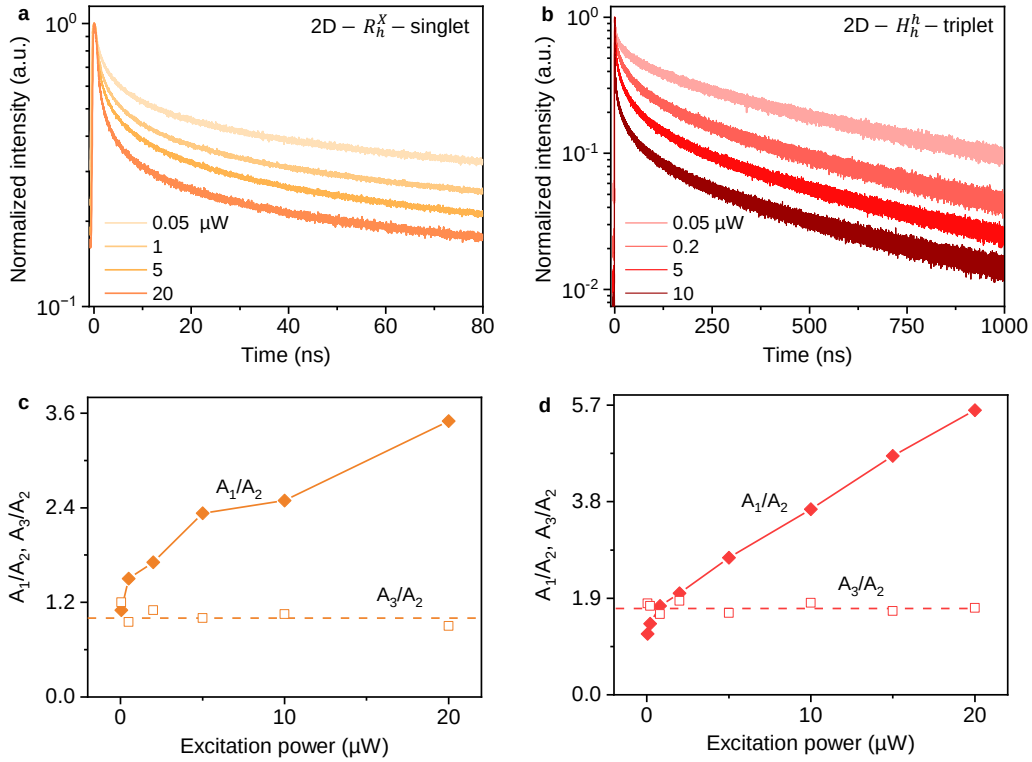

Figure 5.11: Power dependent PL decay. **a** and **b**, Time-resolved PL decay of $\mathrm{R_h^X}$ singlet and $\mathrm{H_h^h}$ triplet interlayer exciton in 2D domains for different excitation powers. **c** and **d**, The amplitude ratios between the fast and intermediate decay components (A_1/A_2, shown by filled diamonds) and between the intermediate and long decay components (A_2/A_3, shown by empty squares) as a function of excitation power. According to best-fits, the three characteristic decay times are independent of the excitation power. However, the fast decay component becomes dominant at high excitation powers as A_1/A_2 increases but A_2/A_3 remains constant, ascribing the fast decay channel to Auger-mediated processes.

respectively, we attribute the third channel of $\mathrm{H_h^h}$ triplet exciton PL decay on 440 ns timescale and $\mathrm{R_h^X}$ singlet exciton state with 45 ns decay time to population feeding from energetically higher-lying long-lived reservoirs, presumably constituted by momentum-dark configurations of valence band holes in WSe_2 and conduction band electrons in $MoSe_2$. Note that the absence of such reservoirs could explain the lack of the third channel in the PL decay of the $\mathrm{H_h^h}$ singlet state that is the top-most energy level according to our calculations summarized in Table 5.1.

For domains with reduced dimensionality, we observe similar behavior in

time-resolved PL. With increasing quantum confinement effects due to reduced system dimensionality, R_h^X states show the trend of prolonged lifetimes for 1D stripe and 0D array regions. The overall ratio of the three components shows no strong dependence on dimensionality. The trend is opposite in 0D arrays of H_h^h triplet excitons, where all decay components decrease as compared to the 2D domain limit, consistent with the absence of quantum confinement effects in reconstructed domains of H_h^h stacking and potentially related to population loss into surrounding H_h^M and H_h^X domain walls with lower-energy interlayer exciton states.

5.4.4 Power- and temperature-dependent photoluminescence

We investigated power-dependent interlayer exciton PL of different types of domain and temperature-dependent of interlayer excitons in 2D domains. Figure 5.12 shows (normalized) low to high powers PL spectra of R-type structures at 4 K. At 10 nW excitation, a Lorentzian fit to the PL spectra of 2D and 1D domains yield FWHMs of 4 meV and 11 meV. At high power, the PL lineshapes broaden asymmetrically to higher energy and the narrow and sharp PL peaks of 0D domain merge into a broad peak. We attribute this broadening to the filling of higher-energy interlayer exciton states that are localized to the moiré traps. This effect is more prominent for the R-type due to the deeper moiré potential [P2, 60]. In H-type stacking, we observe similar power-dependent interlayer exciton PL results that the PL linewidths become broader of 2D domain and the structured PL peaks merge into a broad peak of 0D arrays along with increasing powers depicted in Figure 5.13. Moreover, the PL intensity of H_h^h singlet increased significantly along with increasing excitation power.

Our first observation from temperature-dependence measurements is that interlayer exciton peaks in both R- and H-type heterostructures broaden as temperature increased accompnied with red-shift to lower energy in Figure 5.14a and b. The second observation is that in both cases, the PL intensity of 2D domains starts to decrease from 25 K shown in Figure 5.14c and d. This can be explained by the thermal activation of the interlayer shear Raman mode ($\sim$ 17 cm^{-1}), which only exists in commensurate (reconstructed) region [265]. We note that the temperature dependence of H-type samples showed that the relative PL intensity of the singlet to the triplet increases with temperature [155] in Figure 5.14e. The red line represents the simple two-level model following Boltzman distribution with the energy splitting between singlet and triplet exciton $\Delta = 25$ meV.

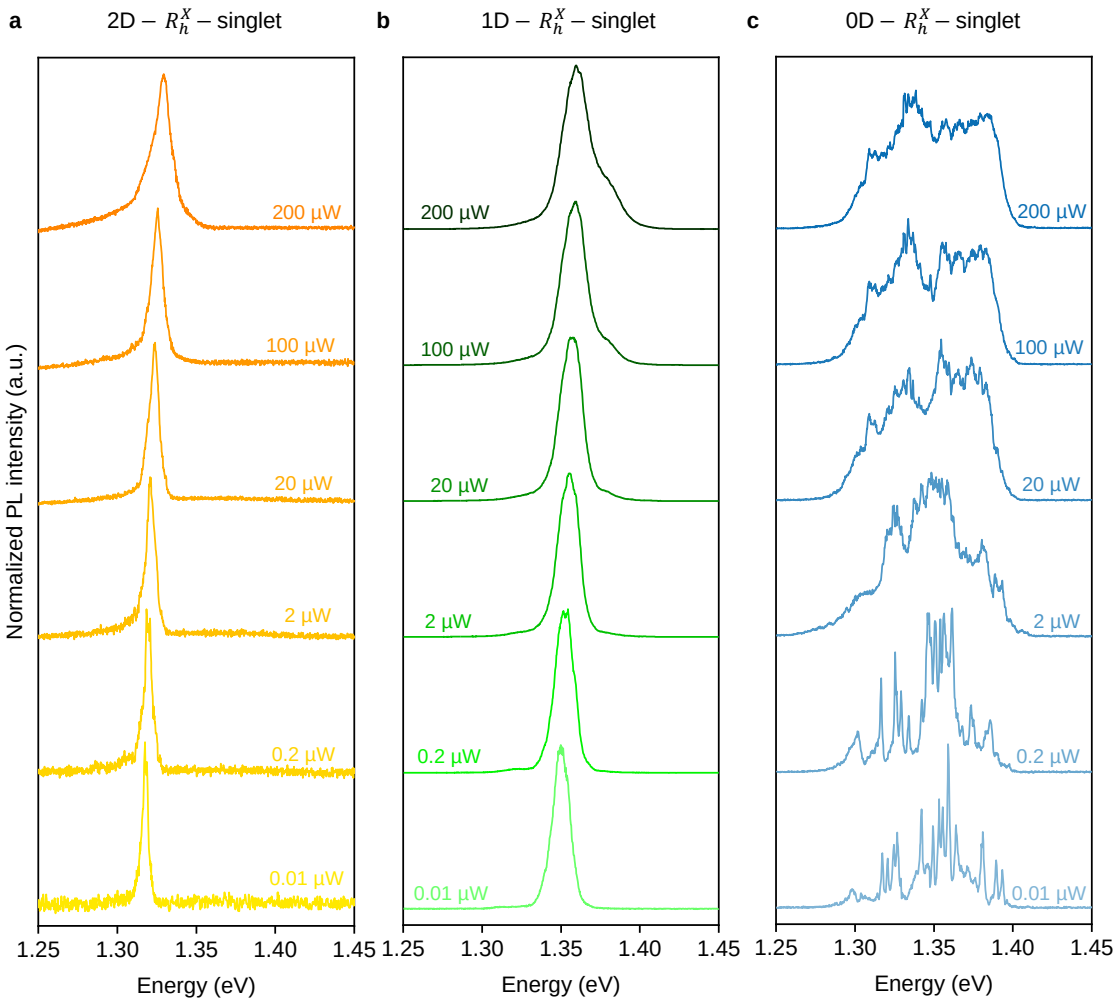

Figure 5.12: Power-dependent interlayer exciton PL of different types of domain in a aligned R-type HBL. **a**-**c**, Normalized PL spectra at selected excitation powers for 2D domain, 1D stripe and 0D domain regions. All the data was acquired with excitation wavelength of 725 nm. For 1D stripe case, a blue shoulder eventually emerges in the PL spectrum when the exciation power increases. Considering the interlayer exciton in a 1D confined system, we assign the blue shoulder to the transverse mode, while the main peak corresponds to the longitudinal mode [268].

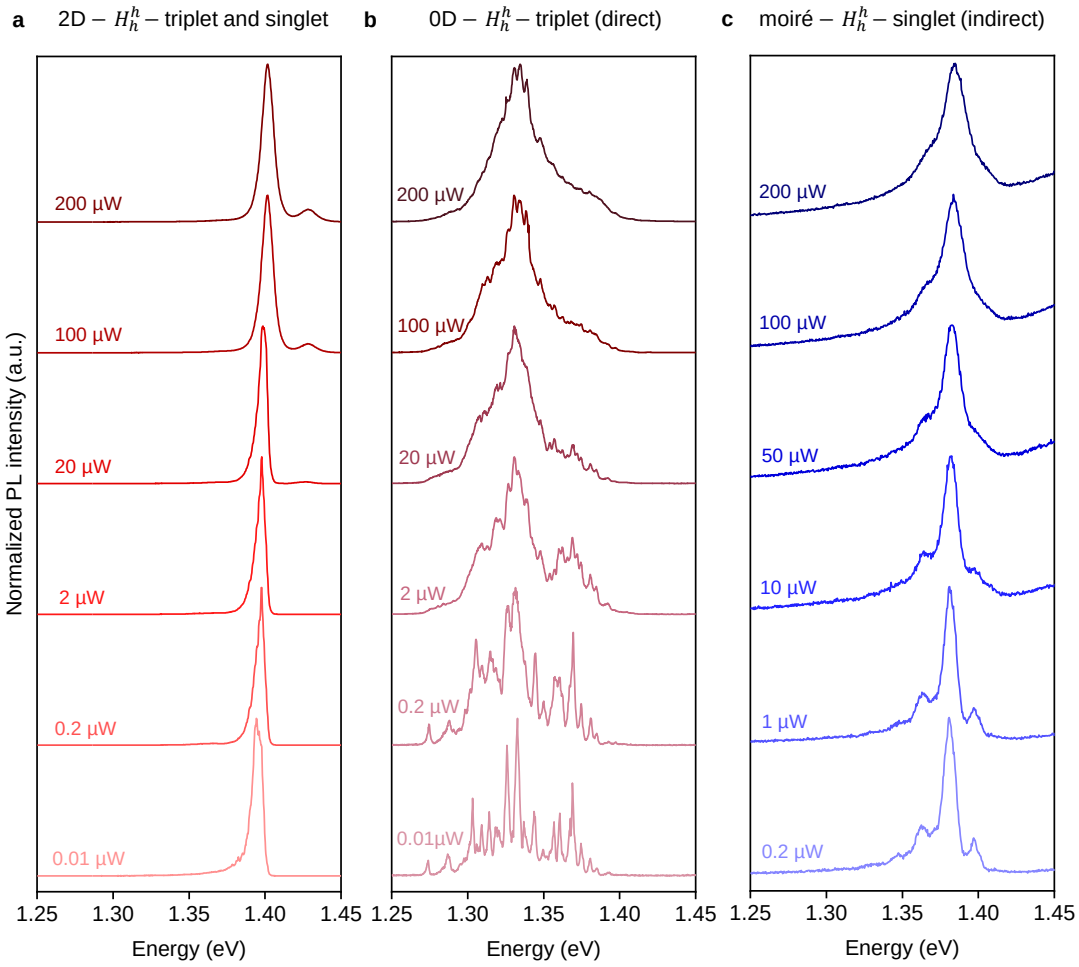

Figure 5.13: Power-dependent interlayer exciton PL of different domain types in H-type HBLs. **a-c**, Normalized PL spectra at selected excitation powers for a 2D domain, domains of 0D arrays, and a dark region in a HBL moiré superlattice with 3° twist angle. For all data, the excitation wavelength was 725 nm.

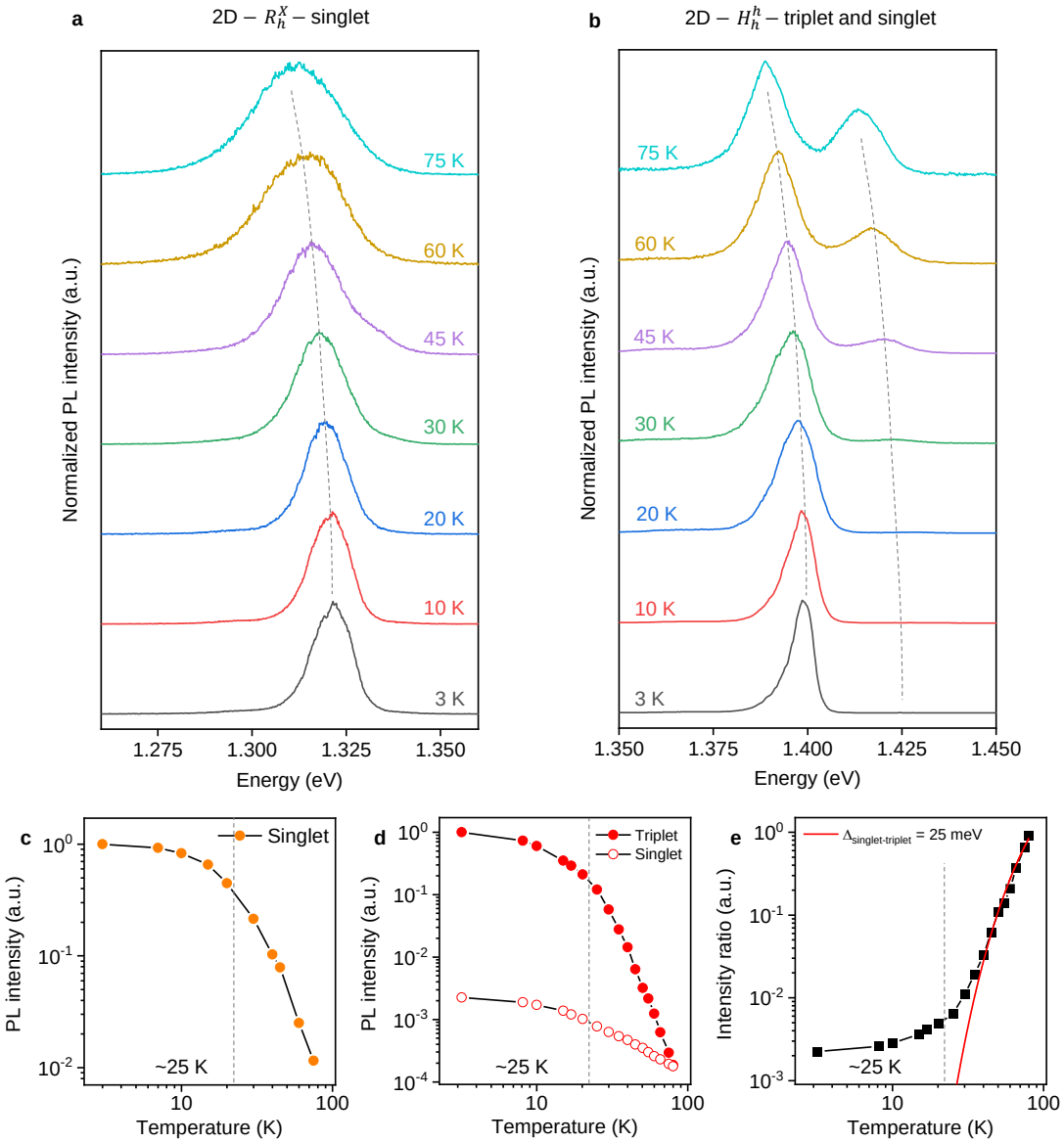

Figure 5.14: Temperature dependent of interlayer excitons PL in 2D domains. **a** and **b**, Normalize PL spectra at selected sample temperatures for 2D domain regions in R- and H-type HBLs. The dashed lines highlight the shift of the peaks. **c** and **d**, Integrated PL intensity as a function of temperature for the peaks of 2D domain in R- and H-type stacking. **e**, PL intensity ratio between singlet and triplet as a function of temperature in 2D domain of H-type.

5.5 Correlation of reconstruction and optical spectroscopy in one sample

To provide a direct evidence for correlations between mesoscopically reconstructed domain dimensionality and respective optical features, we performed SEM imaging and cryogenic optical spectroscopy on the same sample. We fabricated a fully hBN encapsulated H-type sample with a thin layer top hBN below 5 nm to ensure sufficient transparency for secndary electrons. More details about the sample preparation method are shown in supplementary information of manuscript [P2]. Figure 5.15a and b show the secondary electron modulated SEM image and interlayer exciton PL intensity map of the H-type heterostack. The SEM shows coexisting 2D, 1D and 0D domains. Consistently, the PL map exhibits sizable intensity variations across the sample. By co-aligning the PL map and the SEM image (Figure 5.15c), we correlate the spectral features with the local characteristics of domain geometry. All observations and conclusions from direct correlation are shown in Figure 5.16 and Figure 5.17.

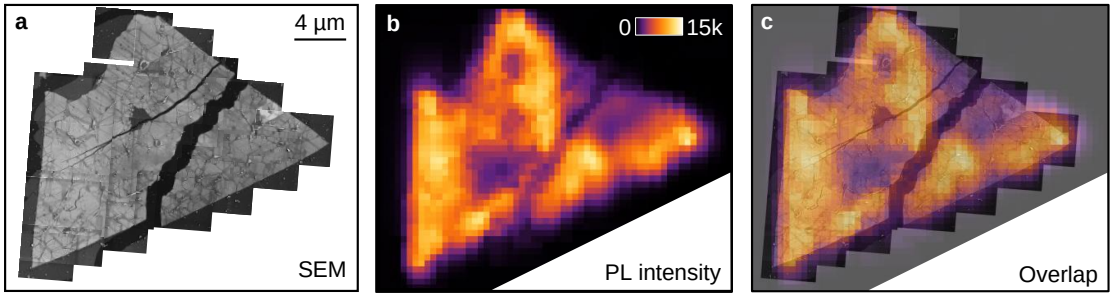

Figure 5.15: a, Secondary electron micrograph, composed of individual small-area images, with characteristic features of sample imperfections and mesoscopic reconstruction. **b**, PL intensity map in the spectral band of interlayer excitons at 3.2 K. **c**, Overlay of the SEM image in **a** and the PL map in **b**.

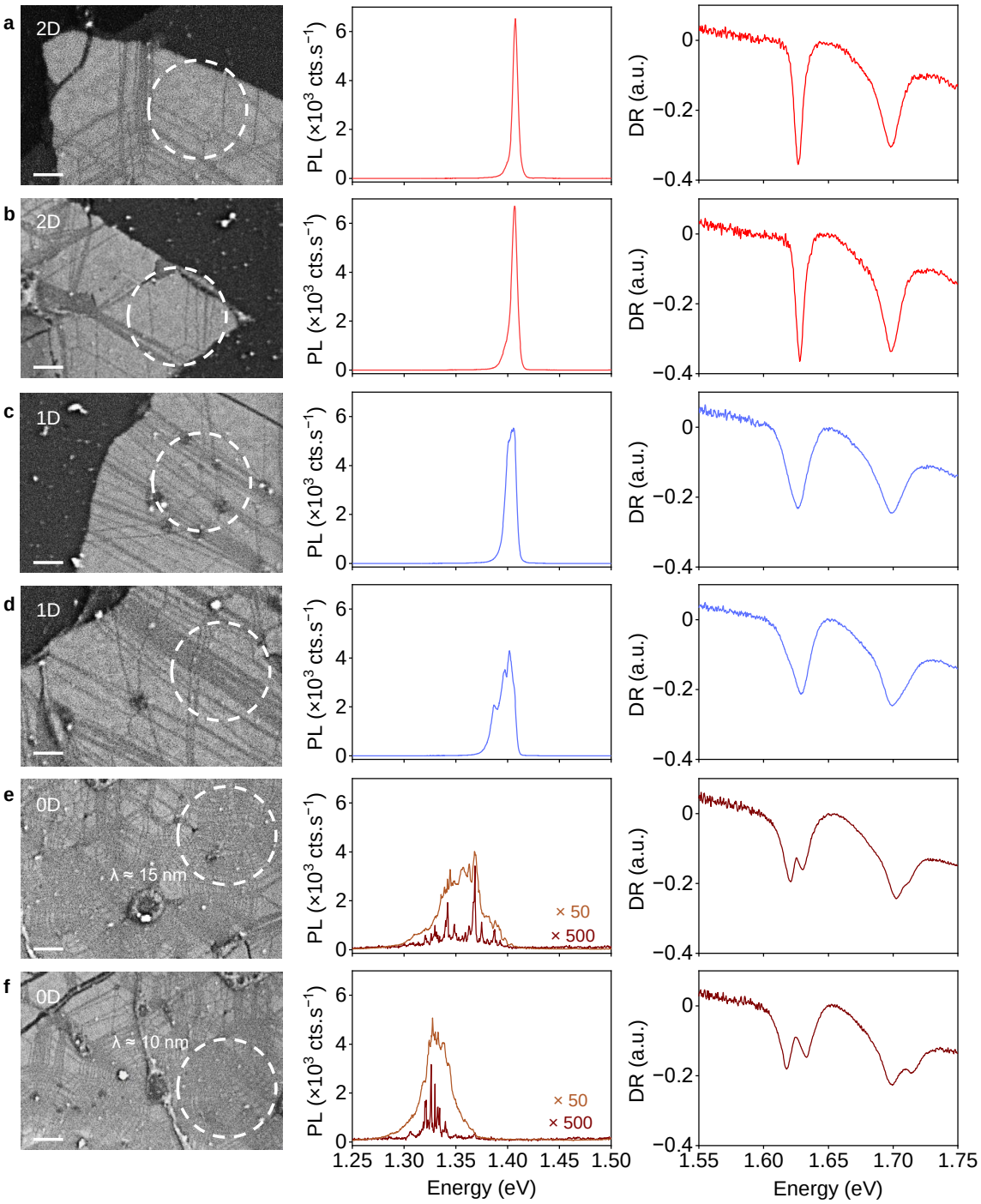

Figure 5.16: a-f, Left panels show representative areas of 2D (**a** and **b**), 1D (**c** and **d**) and 0D (**e** and **f**) domains identified in SEM imaging (the scale bars are 200 nm). Central and right panels show the corresponding PL and DR spectra within the optical spot delimited by dashed circles. The PL spectra were excited with 2 μW laser power. For 0D domains, the PL spectra at 0.01 μW are shown (dark brown) with respective scaling factors in addition to the spectra recorded at 2 μW (light brown).

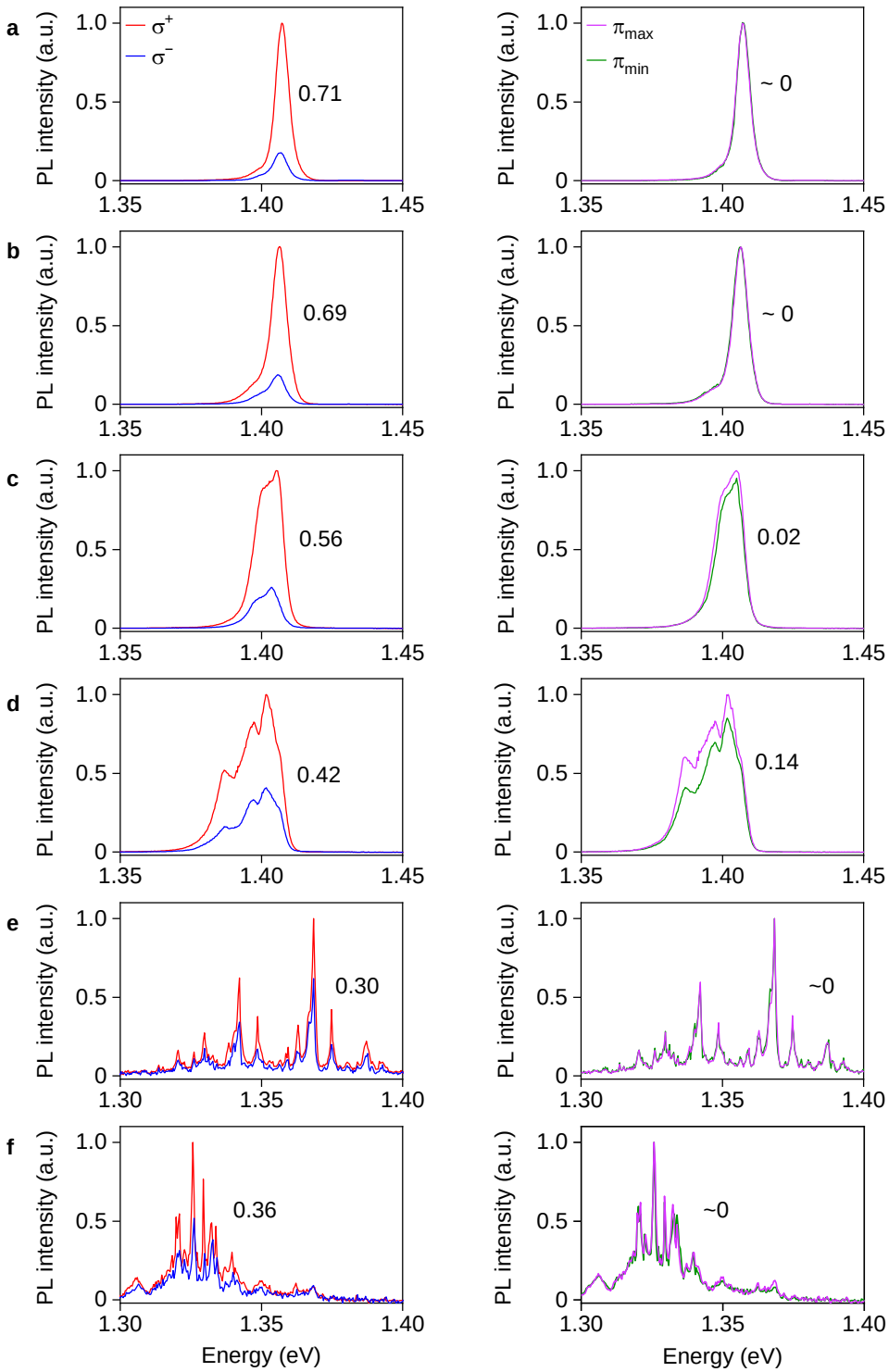

Figure 5.17: a-f, PL spectra recorded in circular (left panels, with σ^+ and σ^- polarized detection shown in red and blue, respectively) and linear (right panels, with two orthogonal orientations of linear polarization for maximum and minimum PL intensity shown in purple and green, respectively) basis from the same regions as in Fig. 5.16 **a-f**. The numbers in each panel denote the respective degrees of circular and linear polarization, P_c and P_l.

5.6 Conclusions

In summary, our insight into mesoscopic reconstruction in $MoSe_2$-WSe_2 HBLs identifies coexisting domains of different dimensionality with distinct exciton regimes. Extended HBLs with small twist feature brightly luminescent, micron-sized 2D domains of energetically favorable $\mathrm{R}_{\mathrm{h}}^{\mathrm{X}}$ and $\mathrm{H}_{\mathrm{h}}^{\mathrm{h}}$ registries which occur mainly at sample edges or line defects and exhibit signatures of 2D singlet and triplet interlayer excitons. Stripes of 1D domains connect 2D domain areas to arrays of nanometer-sized 0D domains characterized by split intralayer exciton resonances and spectrally narrow lines of interlayer excitons. In contrast, HBLs with relatively large twist angles locked in moiré patterns, have received only limited attention in optical spectroscopy due to the dark nature of exciton-polarons. The broad evidence for mesoscopic reconstruction in bilayer graphene, hBN, CrI_3 ferromagnets and TMD semiconductors suggests that the phenomenon is universal across samples and devices of layered van der Waals heterostructures. Ultimately, both understanding and control of mesoscale reconstruction will facilitate further developments of van der Waals quantum materials with tailored electronic, optical and magnetic properties.

Chapter 6

Optical properties of CVD grown $MoSe_2$-WSe_2 heterostructures

THIS CHAPTER IS BASED ON THE MANUSCRIPT [P3]
Li, Z., Tabataba-Vakili, F., Zhao, S., Rupp, A., Bilgin, I., Herdegen, Z., März, B., Watanabe, K., Taniguchi, T., Schleder, G. R., Baimuratov, A. S., Kaxiras, E., Müller-Caspary, K. & Högele, A. Lattice reconstruction in $MoSe_2$-WSe_2 heterobilayers synthesized by chemical vapor deposition. *arXiv preprint.* arXiv: 2212.07686 (2022)

Expanding the survey of $MoSe_2$-WSe_2 HBLs the following chapter describes the results of cryogenic spectroscopy studies on hBN encapsulated CVD-grown $MoSe_2$-WSe_2 HBLs in twisted configurations. The exploration of CVD-grown $MoSe_2$-WSe_2 HBLs still stays on the absence of lateral moiré potentials signified by one atomic registry extending laterally over large sample areas with simple room-temperature PL spectra. Therefore, it is instructive to investigate CVD-grown HBLs at low temperature. We started with characterizations of AFM, SEM and Raman spectroscopy to discriminate the thickness and configuration of H- and R-type stackings. With subsequent optical spectroscopy methods we elucidate the role of atomic reconstruction in samples and identify the coexistence of moiré-like 0D array cores and extended moiré-free 2D domain regions in heterostacks with parallel and antiparallel alignment. The high PL intensity and narrow optical transition linewidth spectra indicate our high-quality samples. Our work highlights the potential of chemical vapor deposition for applications requiring moiré-free uniform systems and moiré-like exciton-confining arrays.

6.1 Introduction

Vertical HBLs of TMD semiconductors manifest in two contrasting regimes. On the one hand, exfoliation-stacked heterobilayers with finite lattice mismatch or twist angle give rise to periodic 2D moiré patterns, which in turn result in flat moiré minibands of charge carriers with rich phenomena of correlated Hubbard model physics [130, 247, 251–253, 269]. Moiré potentials also profoundly affect strongly bound electron-hole pairs in the form of intralayer [256, 270] and interlayer [19, 46, 47, 263] excitons formed by Coulomb correlations within or across individual layers. This scenario is contrasted by moiré-free HBLs on the other hand, obtained from CVD synthesis [18, 150, 271], where the absence of lateral moiré potentials is signified by one atomic registry extending laterally over large sample areas [271] with simple PL spectra [18] or enhanced diffusion of interlayer excitons [150].

HBL systems with diffusive interlayer excitons represent an ideal material platform for integrated dipolar exciton circuits [272], as demonstrated recently in exfoliation-stacked heterostructures with an additional interfacial layer of hBN, which mitigates the exciton-confining moiré potential [273, 274]. Even more promising are CVD-synthesized heterobilayers free of moiré effects, featuring enhanced diffusivity of dipolar interlayer excitons [150], unaffected by diffusion-inhibiting moiré confinement [136, 141, 150]. Such moiré-free heterostructures are not only ideal for integrated exciton circuits with external control by electrostatic gates [275, 276], they could also enable deterministically imprinting arbitrary, tunable potential landscapes via patterned gate-electrodes [274, 277] or dielectric superlattices [278].

Moiré-free domains on micron length scales also emerge in heterostructures with small lattice mismatch and marginal twist subject to mesoscopic lattice reconstruction, where the driving mechanism behind atom rearrangement into energetically favorable registries is provided by the competition between intralayer strain and interlayer adhesion energy [48, 49, 51], yielding mesoscopic 2D domains of only one registry in $MoSe_2$-WSe_2 stamping-assembled heterostacks [P2]. For practical applications, however, such non-deterministic fabrication methods with resulting spatial inhomogeneities in morphology and optical properties [P2] limit the required uniformity and scalability, rendering CVD-based approaches to large-area moiré-free systems a promising alternative.

In this work, we present an elaborate study of CVD-synthesized vertical $MoSe_2$-WSe_2 heterobilayers with evidence for extended reconstruction into domains of one or two atomic registries, enclosing a central region of reconstructed nanoscale domains [48, 49, P2]. Our studies cover both high-symmetry stacking configurations

with 0° (R-type) and 180° (H-type) twist angle, and employ complementary imaging and optical spectroscopy methods to identify the diversity in local configurations of the reconstructed crystal lattice and the respective signatures of exciton transitions. Our work highlights the potential of CVD synthesis for obtaining both extended moiré-free domains and exciton-confining arrays of reconstructed moiré regions, realizing the limits of dipolar excitons with and without a spatially varying potential landscape.

6.2 Characterizations of CVD-grown HBLs

Our CVD-based $MoSe_2$-WSe_2 samples consist of R- and H-type stackings on the same large $MoSe_2$ ML flake were grown on SiO_2/Si substrates via a two-step method, which can be easily identified by comparing the twist angle between top layer WSe_2 and bottom layer $MoSe_2$. In general, the samples consist of vertical HBLs and lateral heterojunction formed by a large inner ML $MoSe_2$ with some small triangle WSe_2 MLs on top and meanwhile ML WSe_2 grown at the edges of $MoSe_2$. Figure 6.1a depicts an optical image of as-grown HBL flakes with both H- and R-type stackings. We examined another HBL sample sythesized in the same growth run by AFM represented in Figure 6.1b with thickness of ~ 0.8 nm top layer WSe_2. To further access the structures of HBL flakes, SEM characterization is needed as a powerful tool. In Figure 6.1c, there is a small-size triangle in the center of both H- and R-type stackings, which exhibit different optical properties from those of the outer regions and will be discussed in the following sections.

We confirm the structural composition of the sample by performing Raman spectroscopy (Figure 6.2). The monolayer regions clearly show the three characteristic peaks, a sharp one at 238 cm^{-1} assigned to the out-of-plane vibration of Se atoms A_{1g} mode, and two broad ones with higher wavenumber ($\sim$ 285 cm^{-1}) and ($\sim$ 358 cm^{-1}) corresponding to the E^1_{2g} and B^1_{2g} modes associated with the in-plane vibration of Mo and Se atoms for ML $MoSe_2$ [142, 271, 279]. For ML WSe_2, it features degenerate in-plane E^1_{2g} and out-of-plane A_{1g} first-order Raman modes around 249 cm^{-1}, the double resonance 2LA mode at 257 cm^{-1}, and a series of multi-phonon modes in the region 358-395 cm^{-1}. All Raman modes are consistent with the ML features [142, 271, 279], and the HBL regions clearly show both peaks, which unambiguously confirms the composition of the $MoSe_2$-WSe_2 HBLs.

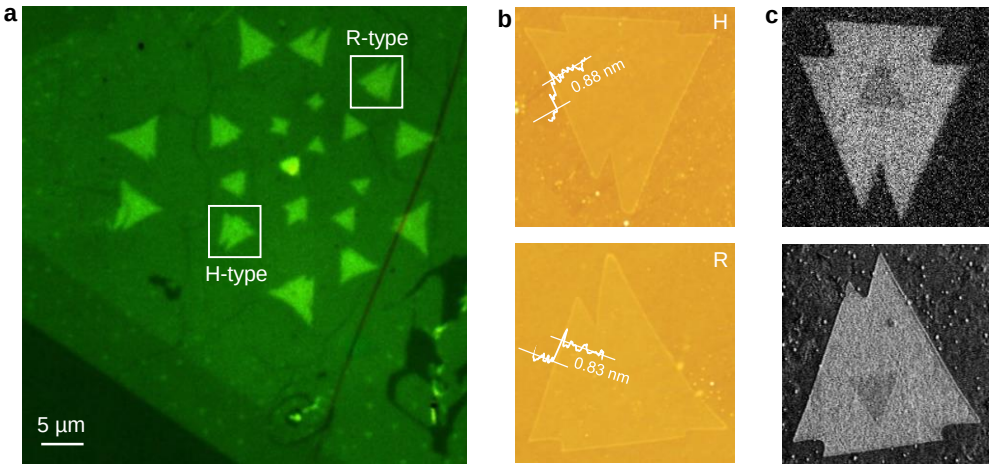

Figure 6.1: Characteristics of CVD grown $MoSe_2$-WSe_2 HBLs in H- and R-type stacking. **a**, Optical micrograph of HBLs with H and R-type geometries. **b**, AFM images with height profiles of typical H and R HBLs (top and bottom), showing a step height of $\sim$ 0.8 nm corresponds to ML WSe_2 thickness. **c**, SEM images of typical H and R HBLs (top and bottom) showing sharp edges recorded with secondary electron imaging, which imply good crystallinity of prepared samples.

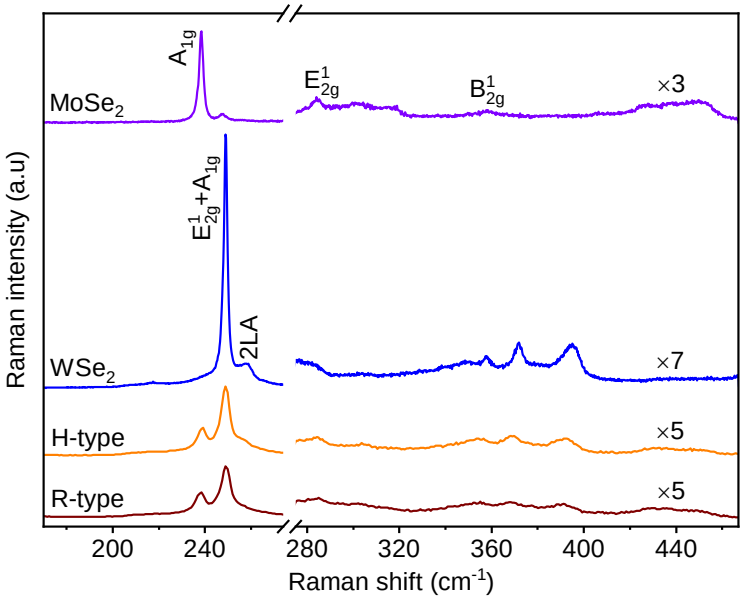

Figure 6.2: Room temperature Raman spectra of ML $MoSe_2$, WSe_2, H- and R-type HBLs. The spectra were recorded with excitation at 532 nm and normalized to the peak intensity of the Si phonon mode at 520 cm^{-1} (note that the intensity of higher-order Raman modes associated with multi-phonon processes were scaled for increased visibility).

Having identified H- and R-type structures by AFM, SEM and Raman spectroscopy, we performed cryogenic micro-PL, degree of polarization and DR spectroscopy in Section 6.3 and Section 6.4. To this end, CVD-grown crystals were encapsulated in hBN by standard lift-off and exfoliation and transferred onto the SiO_2/Si substrate.

6.3 Photoluminescence, differential reflectivity and degree of polarization in H-type HBLs

Starting with H-type HBL, Figure 6.3a shows the characteristics of cryogenic PL recorded in the spectral bandwidth of interlayer excitons. The laterally extended maps recorded at 4 K shown from left to right the maximum PL intensity, degree of circular polarization, P_c and differential reflectivity, DR. Each atomic registry uniquely determines the combination of transition energies [P2, 60, 61], optical selection rules [60, 61, 97], and oscillator strengths [15, 45] of interlayer excitons, and thus provides means for spectroscopic characterisization [P3]. The PL map exhibits extended bright emission at the outer area but dark emission near the center of the flake. The variations in PL intensity upon lateral displacement of the observation spot by a few microns are accompanied by changes in the spectral characteristics shown representatively in Figure 6.3d. The respective PL spectra of one bright spot (top panel of Figure 6.3d) marked by diamond features two peaks at 1.40 eV and 1.42 eV, with the highest degree of circular polarization in Figure 6.3b and opposite signs in the P_c values in Figure 6.3e, which correspond to the triplet and singlet interlayer exciton transitions in extended H_h^h domains of reconstructed mechanically stacked samples [18, 44, P2, 257]. In the dark area near the center of the H-type heterostack marked by circle in Figure 6.3a and the bottom panel of Figure 6.3d, we observe reduced intensity of the main PL peak with decreased P_c value (bottom panel of Figure 6.3e).

We can intuitively observe the structure of studied H-type HBL from the cryogenic DR map in Figure 6.3c, which consists of small inner triangle with small absolute DR value and large outer triangle with high absolute DR value. The cryogenic DR spectra of intralayer excitons, which probe the intralayer exciton absorption of the positions representative of 2D domain and 0D domain arrays in H-type HBL are shown in Figure 6.3f. The DR resonances of intralayer excitons at 1.63 eV and 1.70 eV on bright spot (top spectrum) develop into two well-resolved resonances and

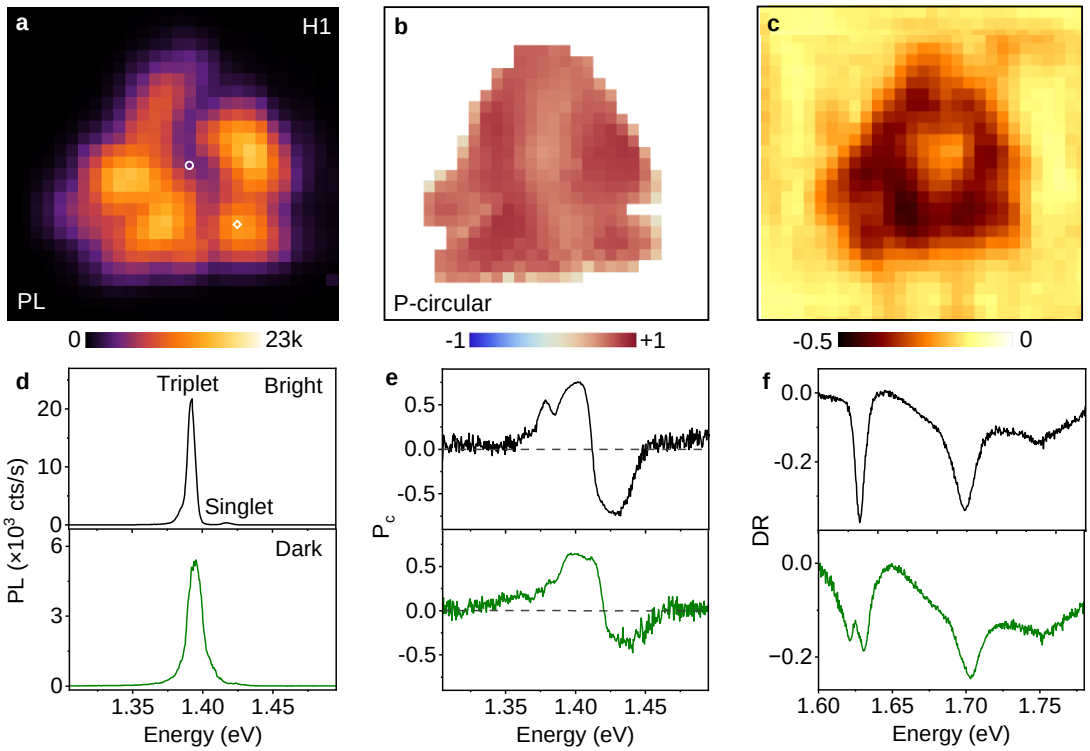

Figure 6.3: a-c, Maps of maximum interlayer exciton PL intensity, degree of circular polarization, P_c and differential reflectivity, DR in H-type geometry. **d**, PL spectra of bright and dark spots marked by diamond and circle in the map. **e**, degrees of circular polarization corresponding to the bright and dark positions in the PL spectra. **f**, DR spectra of intralayer excitons from the bright (top) and dark (bottom) regions. The peak multiplicity is a hallmark of nanoscale domains. The PL spectra were recorded with an excitation wavelength of 726 nm and excitation power of 40 μW.

a broadening around $MoSe_2$ and WSe_2 intralayer exciton transitions in the dark area (bottom spectrum). The observation of doublets in the identifies the central triangles as arrays of reconstructed 0D domains, which can form as nanoscale hexangons of H_h^h registry [51, P2].

All the above features manifest consistently across all of our samples. We selected another H-type HBL and the PL spectroscopy is shown in Figure 6.4. The respective PL spectra of the dark spot is broader and red shift with reduced P_c velue and multi-peak DR spectra (bottom panel in Figure 6.4c-e) compared with that of bright spot (top panel in Figure 6.4c-e). Therefore, we can conclude that the optical properties of our CVD-grown H-type HBLs are quite similar with the optical

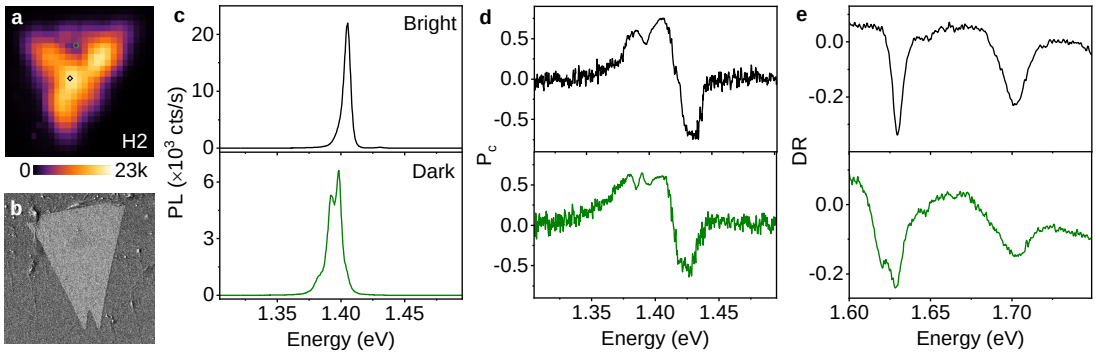

Figure 6.4: a and **b**, PL map of interlayer exciton and SEM image of an analogous H-type HBL. **c**, PL spectra in bright and dark spots marked by diamonds and circles in the map. **d**, degrees of circular polarization in the PL spectra corresponding bright and dark positions. **e**, DR spectra of intralayer excitons from the bright (top) and dark (bottom) regions. The PL spectra were recorded with an excitation wavelength of 726 nm and excitation power of 40 μW.

properties of MLs stacked H-type HBLs.

6.4 Photoluminescence, differential reflectivity and degree of polarization in R-type HBL

Following the analysis method of H-type HBLs, we studied all of the R-type HBLs and selected two flakes for typical research. The laterally extended maps recorded at 4 K shown from left to right the interlayer exciton PL maximum intensity, P_c and DR in Figure 6.5a-c. The PL map exhibits sizable intensity variations on micrometer scales, with nearly two orders of magnitude lower intensity than that in H-type HBLs, which is surprising as reconstructed mechanically stacked samples support the opposite trend [P2]. The variations in PL intensity of the observation spot by a few microns are accompanied by changes in the spectral characteristics shown representatively in Figure 6.5d. In the upper left corner marked by black diamond, the representative black PL spectrum features only one peak at 1.45 eV, which is blue-shifted by 120 meV from its counterpart observed on reconstructed $\mathrm{R_h^X}$ domains of mechanically stacked HBLs at 1.33 eV [P2] and exhibits zero P_c value in the top panel of Figure 6.5e. This finding, combined with the PL energy position and reduced relative brightness, is indicative of interlayer exciton states with z-polarized transitions characteristic of $\mathrm{R_h^M}$ atomic registry [45, 97].

The low intensity PL, labelled by green square in the PL map and shown as

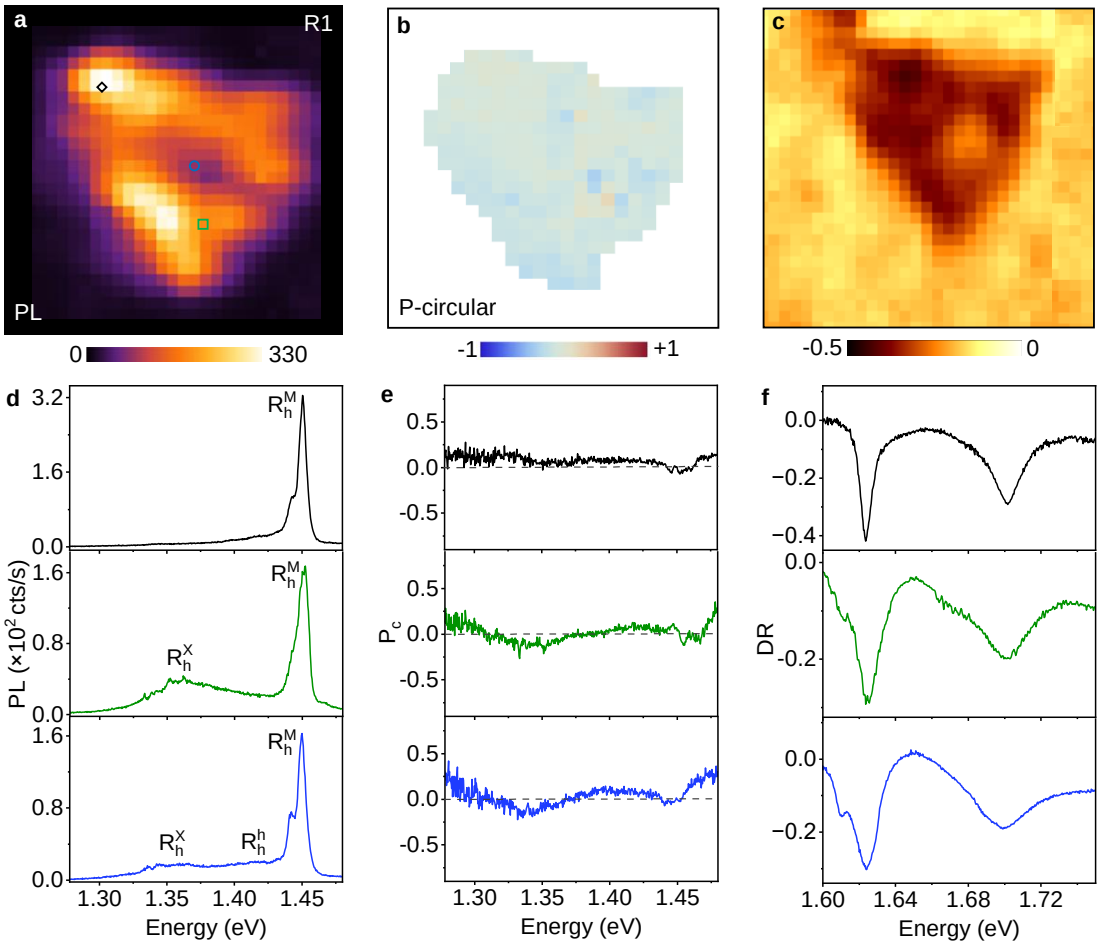

Figure 6.5: a-c, Maps of interlayer exciton PL, P_c and DR in R-type geometry. **d**, PL spectra in three different domain spots marked by diamond, circle and square in the PL map. **e**, degrees of circular polarization relative to the PL spectra positions. **f**, DR spectra of intralayer excitons from the PL corresponding regions. The PL spectra were recorded with an excitation wavelength of 726 nm and excitation power of 20 μW.

green trace in the middle panel of Figure 6.5d, features two peaks at 1.45 eV and 1.35 eV. At the expense of simple single peak at 1.45 eV, the PL at 1.35 eV is spectrally dispersed over 50 meV with a negative P_c value in the middle panel of Figure 6.5e, which is assigned to the singlet interlayer exciton in R_h^X registry. More interesting, there is another peak emergent between R_h^M and R_h^X in the bottom panel of Figure 6.5d with positive P_c value when we focus on the darker spot marked by blue circle near the center of the PL map, we attribute this peak to the singlet interlayer exciton in R_h^h registry [45, P2].

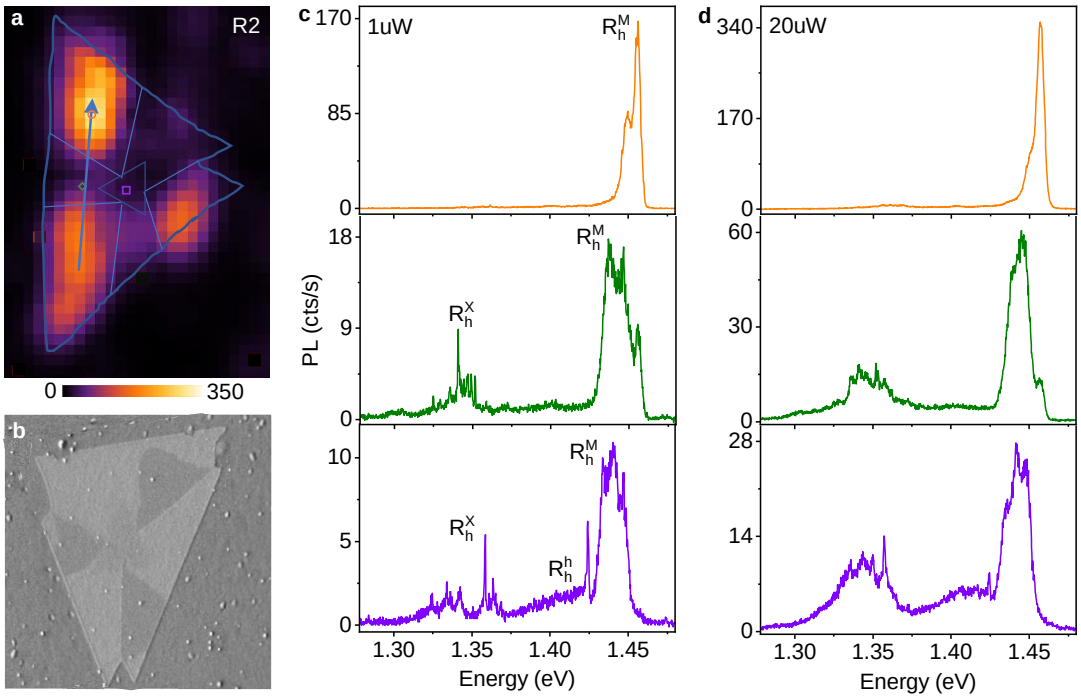

Figure 6.6: a and **b**, maximum PL intensity map of interlayer exciton and SEM image of a R-type HBL. **c** and **d**, PL spectra in three different domain spots marked by diamond, circle and square in the PL map recorded with excitation powers of 1 μW and 20 μW.

The cryogenic DR map in Figure 6.5c matches well with PL map and shows the structure of studied R-type HBL, which consists of small inner triangle with low absolute DR value and large outer triangle with high absolute DR value. Bearing in mind the PL multiplicity of Figure 6.5d, the corresponding characteristics of DR spectra (Figure 6.5f) are straightforwardly explained, which reflects the presence of only one registry in bright spots and different registries present in dark spots, convincingly assigning sample areas with dark PL to areas of 0D arrays.

In order to confirm our results, another R-type flake with more prominent PL spectra is shown in Figure 6.6. There are three separate bright regions alternatingly connected with three separate moderate intensity areas and a much darker region in the center shown in the PL map of Figure 6.6a. The respective PL spectra are presented in Figure 6.6c and d under 1 μW and 20 μW excitation powers. Same with the PL spectra of R1, there is only one narrow peak at 1.45 eV in the top panel of Figure 6.6c and d, marked by orange circle in the PL map. The PL spectra in the middle panel of Figure 6.6c, labeled by green diamond in the PL map, exhibit two

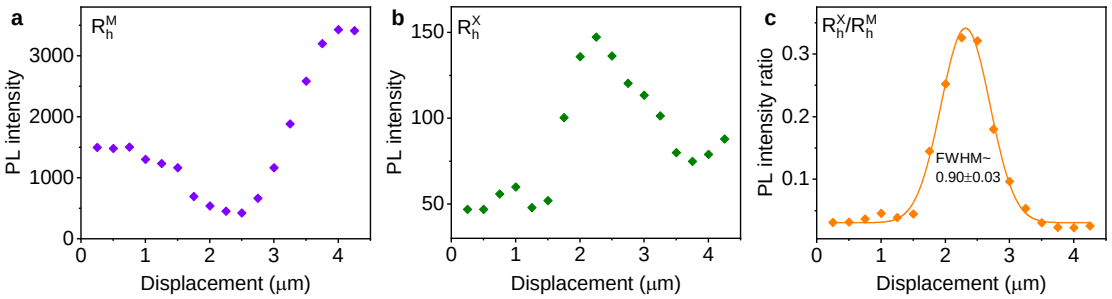

Figure 6.7: **a**, PL intensity of $\mathrm{R_h^M}$ extracted from PL map along the the blue arrow in Figure 6.6a. **b**, PL intensity of $\mathrm{R_h^X}$ extracted from the same positions of **a**. **c**, Intensity ratio of $\mathrm{R_h^X/R_h^M}$ with Gauss fitting.

broad and structured peaks dispersed over 50 meV under 1 μW excitation power, whereas merge into broad peaks under high excitation power 20 μW (middle panel of Figure 6.6d). The PL spectra (bottom panel of Figure 6.6c and d) extracted from the purple diamond spot of the PL map involve three peaks that are more evident under 20 μW. The spectroscopy results can be further verified by SEM image consists of alternating contrast domain colors (white and black) in the outer regions and grey in the middle of the flake shown in Figure 6.6b, which are attributed to the distinct registries inside. The similar SEM results of different R-type registries have been observed in our CVD-grown homobilayer WSe_2 as well. We also extracted and plotted the intensity evolution from one bright region across the dark area to another one bright region (blue arrow in Figure 6.6a). As depicted in Figure 6.7a and b, the intensity of $\mathrm{R_h^M}$ registry reduced and the intensity of $\mathrm{R_h^X}$ increased when across the dark region. We can clearly observe the intensity variations from intensity ratio of $\mathrm{R_h^X/R_h^M}$ in Figure 6.7c by using Gauss fitting, indicating that the mixture of $\mathrm{R_h^X}$ and $\mathrm{R_h^M}$ registries is in the order of the optical spot.

6.5 Exciton g-factors in H- and R-type HBLs

To provide further insights into our high quality CVD grown samples and to verify the nature of multiply atomic registries of R-type HBLs, we performed magneto-luminescence experiments and compared the results with theoretical calculation results in Ref. [P2]. The PL spectra under +9 T and the dispersion of the PL peaks in external magnetic fields applied perpendicular to the HBLs are shown in Figure 6.8. Out-of-plane magnetic fields break the time-reversal symmetry and lift the

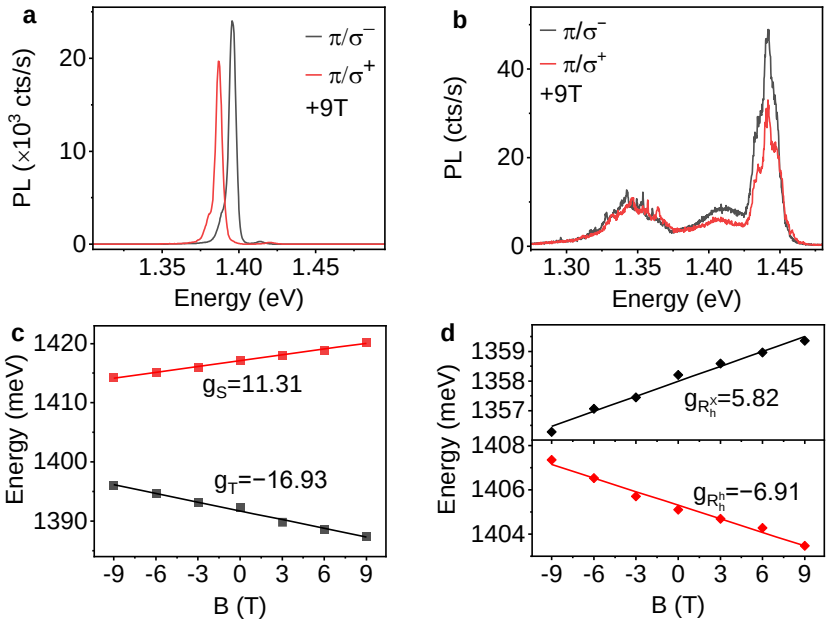

Figure 6.8: a and **b**, PL spectra in a magnetic field of $+9$ T recorded with σ^+ (red) and σ^- (black) polarized detection under linearly polarized excitation (π) of one H bright spot and one R dark spot. **c** and **d**, Peak energy of different stacking registries as a function of B_z.

valley Zeeman splitting $\Delta = E^+ - E^- = g\mu_B B$ propotional to the exciton g-factor, the Bohr magneton μ_B, and the magnetic field B [35, 45]. Polarization-resolved magneto-luminescence spectra of H and R HBLs, recorded at $B = +9$ T with σ^+ and σ^- circular detection under linearly polarized (π) excitation, are shown in Figure 6.8a and b. For H-type HBL, we measured g-factors of -16.93 for $\mathrm{H}^{\mathrm{h}}_{\mathrm{h}}$ triplet and 11.31 for $\mathrm{H}^{\mathrm{h}}_{\mathrm{h}}$ singlet in Figure 6.8c, and for R-type HBL, we measured g-factors of 5.82 for $\mathrm{R}^{\mathrm{X}}_{\mathrm{h}}$ and -6.91 for $\mathrm{R}^{\mathrm{h}}_{\mathrm{h}}$ in Figure 6.8d, consistent with numerous past works on ML stacked H- and R-type $MoSe_2$-WSe_2 heterostructures [280, 281] and DFT calculations [45, P2, 244], but have not been previously reported in CVD grown $MoSe_2$-WSe_2 HBLs. In addition, there is zero Zeeman splitting of the peak at 1.45 eV (Figure 6.8b) under magnetic field $B = +9$ T with σ^+ and σ^- circular detection under linearly polarized (π) excitation.

In Figure 6.9a, we present for the first time the PL intensity map of z-polarized $\mathrm{R}^{\mathrm{M}}_{\mathrm{h}}$ singlet interlayer exciton as a function of out-of-plane magnetic field B from -3 to $+3$ T with circularly polarized σ^+ detection under linearly polarized excitation. To measure this fine structure, we detect with a 1200 grooves/mm grating spectrometer to increase spectral resolution (40 μeV) under low excitation power 1 μW. Unlike the

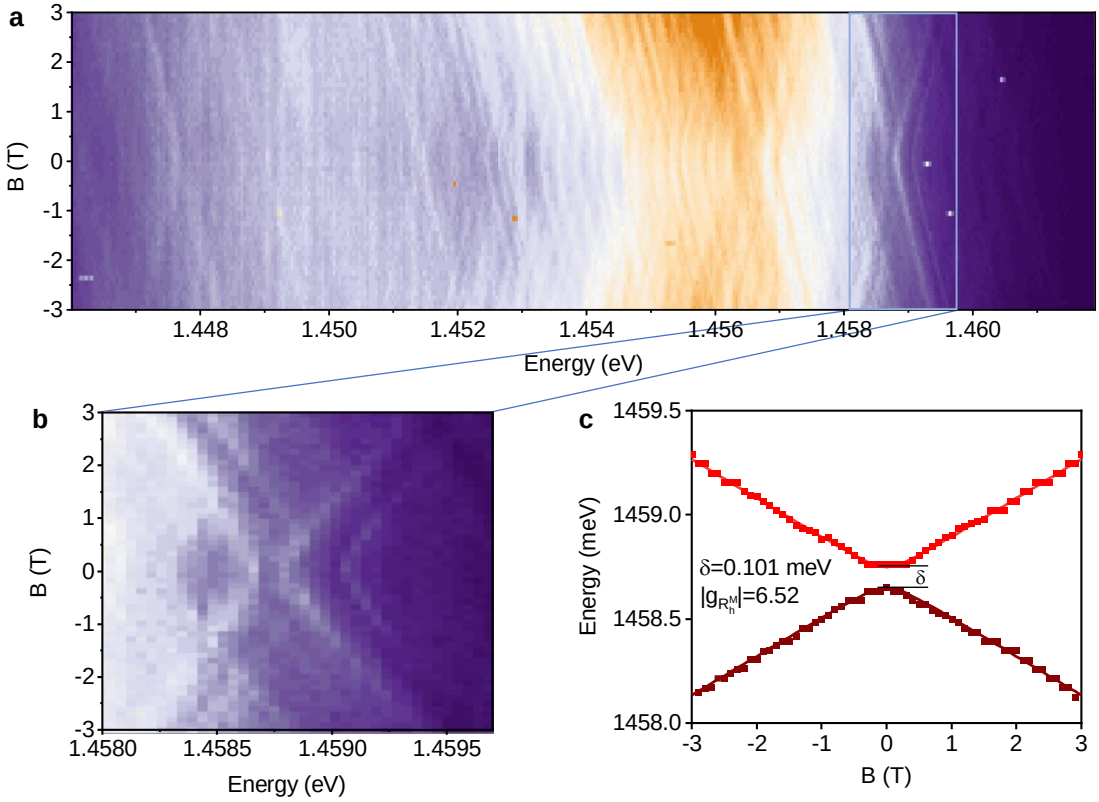

Figure 6.9: **a**, PL intensity map of $\mathrm{R}_{\mathrm{h}}^{\mathrm{M}}$ singlet interlayer exciton as a function of longitudinal magnetic field B measured with σ^+ under under linearly polarized excitation (π). **b**, Zoom-in version of the PL intensity map in the energy range 1458.1-1459.7 meV. **c**, Energy of $\mathrm{R}_{\mathrm{h}}^{\mathrm{M}}$ singlet exciton states as a function of B extracted from **b**.

quite narrow single spectroscopy (FWHM less than 1 meV) in QD-analogous [282, 283], we can observe that the whole PL consists of bunches of narrow spectroscopy with z-polarized interlayer exciton feature from -3 to $+3$ T but merges into each other at high magnetic field except for the spectroscopy at the edge of the highest energy indicated by the zoom-in picture in Figure 6.9b. The Zeeman splitting between the two exciton states is clearly evidenced at large magnetic fields, with an energy separation between the two peaks up to 1.1 meV at $B = +3$ T or -3 T. The energy splitting between the two lines is simply equal to $g_{\mathrm{R}_{\mathrm{h}}^{\mathrm{M}}}\mu_{\mathrm{B}}B$, with $g_{\mathrm{R}_{\mathrm{h}}^{\mathrm{M}}}$ being the g-factor of $\mathrm{R}_{\mathrm{h}}^{\mathrm{M}}$ excitons [35, 45, 282, 283]. We have fitted the energy as a function of B in Figure 6.9c extracted from Figure 6.9b by $E_{\pm} = E_0 \pm \frac{1}{2}\sqrt{\delta^2 + (g\mu_{\mathrm{B}}B)^2}$ with zero-field exciton energy without exchange interaction E_0 and exchange splitting δ [282]. This yields an accurate determination of $\mathrm{R}_{\mathrm{h}}^{\mathrm{M}}$ interlayer exciton exchange splitting $\delta = 0.101$ meV and $\left|g_{\mathrm{R}_{\mathrm{h}}^{\mathrm{M}}}\right| = 6.52$. The g-factor is in quantitative agreement

with our theory result in Table 5.1, predicting a value of 6.3.

6.6 Conclusions

In summary, we carried out cryogenic experiments of interlayer excitons in hBN encapsulated CVD grown $MoSe_2$-WSe_2 HBLs. The optical results demonstrate the high quality of our samples, as evidenced by high PL intensity and narrow-linewidth PL spectra. In H-type stacks, we found 2D domains of $\mathrm{H}_{\mathrm{h}}^{\mathrm{h}}$ atomic registry to dominate extended areas of heterostacks, encompassing a triangular core of 0D domains. In R-type HBLs, three atomic registries $\mathrm{R}_{\mathrm{h}}^{\mathrm{M}}$, $\mathrm{R}_{\mathrm{h}}^{\mathrm{X}}$, $\mathrm{R}_{\mathrm{h}}^{\mathrm{h}}$ coexist in one flake but separate in distinct domains, which is against with that only one ideal atomic registry exists. In addition, in R-type stacks with extended domains of $\mathrm{R}_{\mathrm{h}}^{\mathrm{M}}$ atomic registry, we identify the spectral signatures of interlayer excitons not reported previously from mechanically stacked samples. With extended reconstructed 2D domains and 0D arrays in their inner cores, CVD-grown $MoSe_2$-WSe_2 HBLs realize areas of both moiré-free and moiré-like systems.

Chapter 7

Summary and perspectives

Within this thesis, WSe_2 homobilayer and $MoSe_2$-WSe_2 heterostructures were studied employing comprehensive spectroscopic methods. In homobilayer systems, CVD growth technique was used to achieve large area, twisted angles and free contamination interface flakes. We focused on the optical properties of 2H and 3R stackings encapsulated in hBN, investigated with a confocal microscope under cryogenic conditions. Starting with AFM, Raman spectroscopy and low temperature PL spectra characterizations, we can confirm the high quality of our CVD grown samples. Using optical absorption and PL spectroscopy, we uncover marked differences in the optical characteristics of 2H and 3R bilayer WSe_2. First, the peak multiplicity increases both in PL and DR spectra in 3R stacking. As a second observation, there is a red-shift of 16 meV from the exciton resonance in 2H to that in 3R, as well as a larger red-shift to the first phonon sideband increasing from $\sim$100 mev in 2H to $\sim$150 meV in 3R. We explain the results by combining g-factor measurements and the basis of beyond-DFT theoretical calculations, and find that the lowest energy PL is dominated by momentum-indirect QK and $Q'K$ excitons with intralayer and interlayer character.

In $MoSe_2$-WSe_2 HBLs, we studied twist-angle-dependent HBLs build of MLs and directly CVD growth, and observed distinct optical characters. The formation of interfacial moiré superlattice through rotational misalignment and/or lattice mismatch was a powerful approach to engineer a range of quantum phenomena in van der Waals HBLs. Recent work has theoretically and experimentally reported that HBLs with twist angles $\leqslant 1^\circ$ undergo significant atomic reconstruction leading to discrete commensurate domains divided by narrow domain walls, rather than a smoothly varying rigid-lattice moiré pattern [48, 49, 51, 52, 284]. In our work, we find nanoscale and mesoscopic scale reconstructions in one sample, not only periodically reconstructed patterns. We demonstrate the common domains from SEM images of micron-sized 2D domains at the HBL tips and edges that merge into nanoscale 0D arrays with hexagonal tilling in HBL core in H-type stacking. While the 2D domains are surrounded by elongated 1D stripes that merge into 0D arrays with triangular

tilling in R-type stacking. These reconstructions well account for the sizable intensity variations in the integrated PL map. Experimental and theoretical analysis of P_c, P_l and g-factor indicate that the optimal registries are H_h^h and R_h^X. TRPL revealed distinct recombination times for the individual channels supporting the presented spectral deconvolution. Finally, exciton-exciton interactions were investigated via temperature- and power-dependent measurements.

In our last work, we investigate optical properties of directly CVD grown $MoSe_2$-WSe_2 H- and R-type HBLs with a confocal microscope under cryogenic conditions since there is no relative report. We begin with AFM, SEM and Raman spectroscopy characterizations to demonstrate our pure HBL structures. We observe optical spot sizable 2D domains in the extended outer region and 0D domains near the center of the HBLs. Only H_h^h atomic registry dominates in H-type HBLs. In R-type HBLs, R_h^M and the mixture of R_h^M and R_h^X dominate in the outer triangular region, but all the three atomic registries of R_h^M, R_h^X and R_h^h coexist as 0D domains near the center of the HBLs. Moreover, the main peak in R-type stack is the z-polarized transition of R_h^M atomic registry, which is quite novel.

Our experiments, facilitated by the high quality samples and exceptional quality equipment, providing a comprehensive understanding of the optical features in non-modulated WSe_2 BLs and $MoSe_2$-WSe_2 HBLs. However, there are many limitations to our work which highlight promising areas for further advancements. Interlayer excitons typically possess longer lifetimes and in some cases may affect photoabsorption in solar cells and photodetectors [21, 45, 271]. Therefore, it is of both fundamental and practical importance to explore interlayer excitons in TMDs through external modulations, such as material choice [136, 263, 271], strain [54], pressure [271, 285], and electric field [257, 279, 281], especially gate tunable structures have recently attracted significant interest [255, 257, 279, 281, 286, 287].

With the current dry-transfer technique, people can build up dual gate devices where the dual gate graphene gates can independently control the electrostatic doping and out-of-plane electric field [131]. It has reported that the alternating domains caused by lattice reconstruction have profound impacts on the electric dipole orientations of interlayer excitons [13]. A 5-80% tunable range of degree of circular polarization could be realized by electrostatic doping [37]. Furthermore, an insulating state attributed to the Mott insulating state at half-filling of the moiré superlattice was found in transport measurement [251]. Therefore, the research of optical features and transport measurements of gate tunable devices will be a major topic in our future project.

Bibliography

1. Novoselov, K. S., Geim, A. K., Morozov, S. V., *et al.* Electric field effect in atomically thin carbon films. *Science* **306,** 666–669 (2004).
2. Kosterlitz, J. M. & Thouless, D. J. Long range order and metastability in two dimensional solids and superfluids. (application of dislocation theory). *Journal of Physics C: Solid State Physics* **5,** L124 (1972).
3. Ricci, A., Nielaba, P., Sengupta, S., *et al.* Lack of long-range order in confined two-dimensional model colloidal crystals. *Physical Review E, Statistical, nonlinear, and soft matter physics* **74,** 010404 (2006).
4. Madhi, D. *Ultrafast optics of room-temperature ballistic graphene devices* PhD thesis (Technical University of Denmark, 2018).
5. Azadmanjiri, J., Srivastava, V. K., Kumar, P., *et al.* Graphene-supported 2D transition metal dichalcogenide van der Waals heterostructures. *Applied Materials Today* **19,** 100600 (2020).
6. Li, L., Han, W., Pi, L., *et al.* Emerging in-plane anisotropic two-dimensional materials. *InfoMat* **1,** 54–73 (2019).
7. Schwierz, F. Graphene transistors. *Nature Nanotechnology* **5,** 487–496 (2010).
8. Azizi, A., Eichfeld, S., Geschwind, G., *et al.* Freestanding van der Waals heterostructures of graphene and transition metal dichalcogenides. *ACS Nano* **9,** 4882–4890 (2015).
9. Mak, K. F., Lee, C., Hone, J., *et al.* Atomically thin MoS_2: A new direct-gap semiconductor. *Phys. Rev. Lett.* **105,** 136805 (2010).
10. Liu, H., Neal, A. T., Zhu, Z., *et al.* Phosphorene: an unexplored 2D semiconductor with a high hole mobility. *ACS Nano* **8,** 4033–4041 (2014).
11. Manzeli, S., Ovchinnikov, D., Pasquier, D., *et al.* 2D transition metal dichalcogenides. *Nature Reviews Materials* **2,** 17033 (2017).
12. Paradisanos, I., Shree, S., George, A., *et al.* Controlling interlayer excitons in MoS_2 layers grown by chemical vapor deposition. *Nature Communications* **11,** 2391 (2020).

13. Sung, J., Zhou, Y., Scuri, G., *et al.* Broken mirror symmetry in excitonic response of reconstructed domains in twisted $MoSe_2$/$MoSe_2$ bilayers. *Nature Nanotechnology* **15,** 750–754 (2020).

14. Andersen, T. I., Scuri, G., Sushko, A., *et al.* Excitons in a reconstructed moiré potential in twisted WSe_2/WSe_2 homobilayers. *Nature Materials* **20,** 480–487 (2021).

15. Gillen, R. & Maultzsch, J. Interlayer excitons in $MoSe_2$/WSe_2 heterostructures from first principles. *Phys. Rev. B* **97,** 165306 (2018).

16. Gong, Y., Lin, J., Wang, X., *et al.* Vertical and in-plane heterostructures from WS_2/MoS_2 monolayers. *Nature Materials* **13,** 1135–1142 (2014).

17. Gong, Y., Lei, S., Ye, G., *et al.* Two-step growth of two-dimensional WSe_2/$MoSe_2$ heterostructures. *Nano Lett.* **15,** 6135–6141 (2015).

18. Hsu, W.-T., Lu, L.-S., Wu, P.-H., *et al.* Negative circular polarization emissions from WSe_2/$MoSe_2$ commensurate heterobilayers. *Nature Communications* **9,** 1–7 (2018).

19. Jin, C., Regan, E. C., Yan, A., *et al.* Observation of moiré excitons in WSe_2/WS_2 heterostructure superlattices. *Nature* **567,** 76 (2019).

20. Jin, C., Ma, E. Y., Karni, O., *et al.* Ultrafast dynamics in van der Waals heterostructures. *Nature Nanotechnology* **13,** 994–1003 (2018).

21. Rivera, P., John R., S., Jones, A. M., *et al.* Observation of long-lived interlayer excitons in monolayer $MoSe_2$-WSe_2 heterostructures. *Nature Communications* **6,** 6242 (2015).

22. McCreary, K. M., Phillips, M., Chuang, H.-J., *et al.* Stacking-dependent optical properties in bilayer WSe_2. *Nanoscale* **14,** 147–156 (2022).

23. Wang, G., Chernikov, A., Glazov, M. M., *et al.* Colloquium: Excitons in atomically thin transition metal dichalcogenides. *Rev. Mod. Phys.* **90,** 021001 (2018).

24. Wilson, N. P., Yao, W., Shan, J., *et al.* Excitons and emergent quantum phenomena in stacked 2D semiconductors. *Nature* **599,** 383–392 (2021).

25. Gerber, I. C., Courtade, E., Shree, S., *et al.* Interlayer excitons in bilayer MoS_2 with strong oscillator strength up to room temperature. *Phys. Rev. B* **99,** 035443 (2019).

26. Zhao, W., Ribeiro, R. M., Toh, M., *et al.* Origin of indirect optical transitions in few-layer MoS_2, WS_2, and WSe_2. *Nano Lett.* **13,** 5627–5634 (2013).

27. Molas, M. R., Nogajewski, K., Slobodeniuk, A. O., *et al.* The optical response of monolayer, few-layer and bulk tungsten disulfide. *Nanoscale* **9,** 13128–13141 (2017).

28. Wang, Y., Wang, Z., Yao, W., *et al.* Interlayer coupling in commensurate and incommensurate bilayer structures of transition-metal dichalcogenides. *Phys. Rev. B* **95,** 115429 (2017).

29. Gong, Z., Liu, G.-B., Yu, H., *et al.* Magnetoelectric effects and valley-controlled spin quantum gates in transition metal dichalcogenide bilayers. *Nature Communications* **4,** 2053 (2013).

30. Wu, S., Ross, J. S., Liu, G.-B., *et al.* Electrical tuning of valley magnetic moment through symmetry control in bilayer MoS_2. *Nature Physics* **9,** 149–153 (2013).

31. Jiang, T., Liu, H., Huang, D., *et al.* Valley and band structure engineering of folded MoS_2 bilayers. *Nature Nanotechnology* **9,** 825–829 (2014).

32. Hsu, W.-T., Lin, B.-H., Lu, L.-S., *et al.* Tailoring excitonic states of van der Waals bilayers through stacking configuration, band alignment, and valley spin. *Sci. Adv.* **5,** 7407 (2019).

33. Splendiani, A., Sun, L., Zhang, Y., *et al.* Emerging photoluminescence in monolayer MoS_2. *Nano Lett.* **10,** 1271–1275 (2010).

34. Lindlau, J., Selig, M., Neumann, A., *et al.* The role of momentum-dark excitons in the elementary optical response of bilayer WSe_2. *Nature Communications* **9,** 2586 (2018).

35. Förste, J., Tepliakov, N. V., Kruchinin, S. Y., *et al.* Exciton g-factors in monolayer and bilayer WSe_2 from experiment and theory. *Nature Communications* **11,** 4539 (2020).

36. Funk, V., Wagner, K., Wietek, E., *et al.* Spectral asymmetry of phonon sideband luminescence in monolayer and bilayer WSe_2. *Phys. Rev. Research* **3,** L042019 (2021).

37. Scuri, G., Andersen, T. I., Zhou, Y., *et al.* Electrically tunable valley dynamics in twisted WSe_2/WSe_2 bilayers. *Phys. Rev. Lett.* **124,** 217403 (2020).

38. Wang, Z., Chiu, Y.-H., Honz, K., *et al.* Electrical tuning of interlayer exciton gases in WSe_2 bilayers. *Nano Lett.* **18,** 137–143 (2018).

39. Altaiary, M. M., Liu, E., Liang, C.-T., *et al.* Electrically switchable intervalley excitons with strong two-phonon scattering in bilayer WSe_2. *Nano Lett.* **22,** 1829–1835 (2022).

40. Huang, Z., Zhao, Y., Bo, T., *et al.* Spatially indirect intervalley excitons in bilayer WSe_2. *Phys. Rev. B* **105,** L041409 (2022).

41. Aslan, B., Deng, M., Brongersma, M. L., *et al.* Strained bilayer WSe_2 with reduced exciton-phonon coupling. *Phys. Rev. B* **101,** 115305 (2020).

42. Zimmermann, J. E., Kim, Y. D., Hone, J. C., *et al.* Directional ultrafast charge transfer in a $WSe_2/MoSe_2$ heterostructure selectively probed by time-resolved SHG imaging microscopy. *Nanoscale Horiz.* **5,** 1603–1609 (2020).

43. Purz, T. L., Martin, E. W., Rivera, P., *et al. Ultrafast charge and energy transfer in a $MoSe_2/WSe_2$ heterostructure* in (Conference on Lasers and Electro-Optics, 2020), FF3B.1.

44. Hanbicki, A. T., Chuang, H.-J., Rosenberger, M. R., *et al.* Double indirect interlayer exciton in a $MoSe_2/WSe_2$ van der Waals heterostructure. *ACS Nano* **12,** 4719–4726 (2018).

45. Förg, M., Baimuratov, A. S., Kruchinin, S. Y., *et al.* Moiré excitons in $MoSe_2$-WSe_2 heterobilayers and heterotrilayers. *Nature Communications* **12,** 1656 (2021).

46. Seyler, K. L., Rivera, P., Yu, H., *et al.* Signatures of moiré-trapped valley excitons in $MoSe_2/WSe_2$ heterobilayers. *Nature* **567,** 66 (2019).

47. Tran, K., Moody, G., Wu, F., *et al.* Evidence for moiré excitons in van der Waals heterostructures. *Nature* **567,** 71 (2019).

48. Carr, S., Massatt, D., Torrisi, S. B., *et al.* Relaxation and domain formation in incommensurate two-dimensional heterostructures. *Phys. Rev. B* **98,** 224102 (2018).

49. Enaldiev, V. V., Zolyomi, V., Yelgel, C., *et al.* Stacking domains and dislocation networks in marginally twisted bilayers of transition metal dichalcogenides. *Phys. Rev. Lett.* **124,** 206101 (2020).

50. Weston, A., Zou, Y., Enaldiev, V., *et al.* Atomic reconstruction in twisted bilayers of transition metal dichalcogenides. *Nature Nanotechnology* **15,** 592–597 (2020).

51. Rosenberger, M. R., Chuang, H.-J., Phillips, M., *et al.* Twist angle-dependent atomic reconstruction and moiré patterns in transition metal dichalcogenide heterostructures. *ACS Nano* **14,** 4550–4558 (2020).

52. Enaldiev, V. V., Ferreira, F., Magorrian, S. J., *et al.* Piezoelectric networks and ferroelectric domains in twistronic superlattices in WS_2/MoS_2 and WSe_2/$MoSe_2$ bilayers. *2D Materials* **8,** 025030 (2021).

53. Shabani, S., Halbertal, D., Wu, W., *et al.* Deep moiré potentials in twisted transition metal dichalcogenide bilayers. *Nature Physics* **17,** 720–725 (2021).

54. Bai, Y., Zhou, L., Wang, J., *et al.* Excitons in strain-induced one-dimensional moiré potentials at transition metal dichalcogenide heterojunctions. *Nature Materials* **19,** 1068–1073 (2020).

55. Zhang, Z., Chen, P., Duan, X., *et al.* Robust epitaxial growth of two-dimensional heterostructures, multiheterostructures, and superlattices. *Science* **357,** 788–792 (2017).

56. Van Wijk, M. M., Schuring, A., Katsnelson, M. I., *et al.* Relaxation of moiré patterns for slightly misaligned identical lattices: graphene on graphite. *2D Materials* **2,** 034010 (2015).

57. Dai, S., Xiang, Y. & Srolovitz, D. J. Twisted bilayer graphene: moiré with a twist. *Nano Lett.* **16,** 5923–5927 (2016).

58. Bistritzer, R. & MacDonald, A. H. Moiré bands in twisted double-layer graphene. *Proceedings of the National Academy of Sciences* **108,** 12233–12237 (2011).

59. Wu, F., Lovorn, T. & MacDonald, A. H. Topological exciton bands in moiré heterojunctions. *Phys. Rev. Lett.* **118,** 147401 (2017).

60. Yu, H., Liu, G.-B., Tang, J., *et al.* Moiré excitons: from programmable quantum emitter arrays to spin-orbit-coupled artificial lattices. *Sci. Adv.* **3,** e1701696 (2017).

61. Wu, F., Lovorn, T. & MacDonald, A. H. Theory of optical absorption by interlayer excitons in transition metal dichalcogenide heterobilayers. *Phys. Rev. B* **97,** 035306 (2018).

62. Ponomarenko, L. A., Gorbachev, R. V., Yu, G. L., *et al.* Cloning of dirac fermions in graphene superlattices. *Nature* **497,** 594–597 (2013).

63. Dean, C. R., Wang, L., Maher, P., *et al.* Hofstadter's butterfly and the fractal quantum hall effect in moiré superlattices. *Nature* **497,** 598–602 (2013).

64. Zhang, C., Chuu, C.-P., Ren, X., *et al.* Interlayer couplings, Moiré patterns, and 2D electronic superlattices in MoS_2/WSe_2 hetero-bilayers. *Sci. Adv.* **3,** e1601459 (2017).

65. Yoo, H., Engelke, R., Carr, S., *et al.* Atomic and electronic reconstruction at the van der Waals interface in twisted bilayer graphene. *Nature Materials* **18,** 448–453 (2019).

66. Halbertal, D., Finney, N. R., Sunku, S. S., *et al.* Moiré metrology of energy landscapes in van der Waals heterostructures. *Nature Communications* **12,** 242 (2021).

67. Tartakovskii, A. Moiré or not. *Nature Materials* **19,** 581–582 (2020).

68. Eda, G., Fujita, T., Yamaguchi, H., *et al.* Coherent atomic and electronic heterostructures of single-layer MoS_2. *ACS Nano* **6,** 7311–7317 (2012).

69. Wang, Q., Lai, J. & Sun, D. Review of photo response in semiconductor transition metal dichalcogenides based photosensitive devices. *Opt. Mater. Express* **6,** 2313–2327 (2016).

70. Vishwanath, S., Liu, X., Rouvimov, S., *et al.* Controllable growth of layered selenide and telluride heterostructures and superlattices using molecular beam epitaxy. *Journal of Materials Research* **31,** 900–910 (2016).

71. Splendiani, A., Sun, L., Zhang, Y., *et al.* Emerging photoluminescence in monolayer MoS_2. *Nano Lett.* **10,** 1271–1275 (2010).

72. Radisavljevic, B., Radenovic, A., Brivio, J., *et al.* Single-layer MoS_2 transistors. *Nature Nanotechnology* **6,** 147–150 (2011).

73. Song, J.-G., Park, J., Lee, W., *et al.* Layer-controlled, wafer-scale, and conformal synthesis of tungsten disulfide nanosheets using atomic layer deposition. *ACS Nano* **7,** 11333–11340 (2013).

74. Zhang, Y., Chang, T.-R., Zhou, B., *et al.* Direct observation of the transition from indirect to direct bandgap in atomically thin epitaxial $MoSe_2$. *Nature Nanotechnology* **9,** 111–115 (2014).

75. Cai, Z., Liu, B., Zou, X., *et al.* Chemical vapor deposition growth and applications of two-dimensional materials and their heterostructures. *Chem. Rev.* **118,** 6091–6133 (2018).

76. Ribeiro-Soares, J., Almeida, R. M., Barros, E. B., *et al.* Group theory analysis of phonons in two-dimensional transition metal dichalcogenides. *Phys. Rev. B* **90,** 115438 (2014).

77. Wang, G., Chernikov, A., Glazov, M. M., *et al.* Colloquium: excitons in atomically thin transition metal dichalcogenides. *Rev. Mod. Phys.* **90,** 021001 (2018).

78. Zhang, X., Qiao, X.-F., Shi, W., *et al.* Phonon and Raman scattering of two-dimensional transition metal dichalcogenides from monolayer, multilayer to bulk material. *Chem. Soc. Rev.* **44,** 2757–2785 (2015).

79. Verble, J. L. & Wieting, T. J. Lattice mode degeneracy in MoS_2 and other layer compounds. *Phys. Rev. Lett.* **25,** 362–365 (1970).

80. Zhao, W., Ghorannevis, Z., Amara, K. K., *et al.* Lattice dynamics in mono- and few-layer sheets of WS_2 and WSe_2. *Nanoscale* **5,** 9677–9683 (2013).

81. Wieting, T. J. & Verble, J. L. Infrared and Raman studies of long-wavelength optical phonons in hexagonal MoS_2. *Phys. Rev. B* **3,** 4286–4292 (1971).

82. Zhang, X., Tan, Q.-H., Wu, J.-B., *et al.* Review on the Raman spectroscopy of different types of layered materials. *Nanoscale* **8,** 6435–6450 (2016).

83. Lin, K.-Q., Faria Junior, P. E., Bauer, J. M., *et al.* Twist-angle engineering of excitonic quantum interference and optical nonlinearities in stacked 2D semiconductors. *Nature Communications* **12,** 1553 (2021).

84. Zhao, W., Ribeiro, R. M., Toh, M., *et al.* Origin of indirect optical transitions in few-layer MoS_2, WS_2, and WSe_2. *Nano Lett.* **13,** 5627–5634 (2013).

85. Do, D. T., Mahanti, S. D. & Lai, C. W. Spin splitting in 2D monochalcogenide semiconductors. *Sci. Rep.* **5,** 17044 (2015).

86. Miwa, J. A., Ulstrup, S., Sorensen, S. G., *et al.* Electronic structure of epitaxial single-layer. *Phys. Rev. Lett.* **114,** 046802 (2015).

87. Xiao, D., Liu, G.-B., Feng, W., *et al.* Coupled spin and valley physics in monolayers of MoS_2 and other group-VI dichalcogenides. *Phys. Rev. Lett.* **108,** 196802 (2012).

88. Kormányos, A., Zólyomi, V., Drummond, N. D., *et al.* Spin-orbit coupling, quantum dots, and qubits in monolayer transition metal dichalcogenides. *Phys. Rev. X* **4,** 011034 (2014).

89. Sallen, G., Bouet, L., Marie, X., *et al.* Robust optical emission polarization in MoS_2 monolayers through selective valley excitation. *Phys. Rev. B* **86,** 081301 (2012).

90. Zhao, S., Li, X., Dong, B., *et al.* Valley manipulation in monolayer transition metal dichalcogenides and their hybrid systems: status and challenges. *Reports on Progress in Physics* **84,** 026401 (2021).

91. Echeverry, J. P., Urbaszek, B., Amand, T., *et al.* Splitting between bright and dark excitons in transition metal dichalcogenide monolayers. *Phys. Rev. B* **93,** 121107 (2016).

92. Wang, G., Robert, C., Suslu, A., *et al.* Spin-orbit engineering in transition metal dichalcogenide alloy monolayers. *Nature Communications* **6,** 10110 (2015).

93. Withers, F., Del Pozo-Zamudio, O., Schwarz, S., *et al.* WSe_2 light-emitting tunneling transistors with enhanced brightness at room temperature. *Nano Lett.* **15,** 8223–8228 (2015).

94. Eftekhari, A. Tungsten dichalcogenides (WS_2, WSe_2, and WTe_2): materials chemistry and applications. *J. Mater. Chem. A* **5,** 18299–18325 (2017).

95. Novoselov, K. S., Mishchenko, A., Carvalho, A., *et al.* 2D materials and van der Waals heterostructures. *Science* **353** (2016).

96. He, J., Hummer, K. & Franchini, C. Stacking effects on the electronic and optical properties of bilayer transition metal dichalcogenides MoS_2, $MoSe_2$, WS_2, and WSe_2. *Phys. Rev. B* **89,** 075409 (2014).

97. Förg, M., Colombier, L., Patel, R. K., *et al.* Cavity-control of interlayer excitons in van der Waals heterostructures. *Nature Communications* **10,** 3697 (2019).

98. Constantinescu, G., Kuc, A. & Heine, T. Stacking in bulk and bilayer hexagonal boron nitride. *Phys. Rev. Lett.* **111,** 036104 (2013).

99. Liu, L., Feng, Y. P. & Shen, Z. X. Structural and electronic properties of h-BN. *Phys. Rev. B* **68,** 104102 (2003).

100. Brem, S., Lin, K.-Q., Gillen, R., *et al.* Hybridized intervalley moiré excitons and flat bands in twisted WSe_2 bilayers. *Nanoscale* **12,** 11088–11094 (2020).

101. Wilson, N. R., Nguyen, P. V., Seyler, K., *et al.* Determination of band offsets, hybridization, and exciton binding in 2D semiconductor heterostructures. *Sci. Adv.* **3,** e1601832 (2017).

102. Perdew, J. P., Burke, K. & Ernzerhof, M. Generalized gradient approximation made simple. *Phys. Rev. Lett.* **77,** 3865–3868 (1996).

103. Csonka, G. I., Perdew, J. P., Ruzsinszky, A., *et al.* Assessing the performance of recent density functionals for bulk solids. *Phys. Rev. B,* 155107 (2009).

104. Shishkin, M. & Kresse, G. Self-consistent GW calculations for semiconductors and insulators. *Phys. Rev. B* **75,** 235102 (2007).

105. Grimme, S., Antony, J., Ehrlich, S., *et al.* A consistent and accurate ab initio parametrization of density functional dispersion correction (DFT-D) for the 94 elements H-Pu. *J. Chem. Phys.* **132,** 154104 (2010).

106. Hüser, F., Olsen, T. & Thygesen, K. S. How dielectric screening in two-dimensional crystals affects the convergence of excited-state calculations: monolayer MoS_2. *Phys. Rev. B* **88,** 245309 (2013).

107. Shishkin, M. & Kresse, G. Implementation and performance of the frequency-dependent GW method within the PAW framework. *Phys. Rev. B* **74,** 035101 (2006).

108. Gerber, I. C. & Marie, X. Dependence of band structure and exciton properties of encapsulated WSe_2 monolayers on the hBN-layer thickness. *Phys. Rev. B* **98,** 245126 (2018).

109. Slobodeniuk, A. O., Bala, L., Koperski, M., *et al.* Fine structure of K-excitons in multilayers of transition metal dichalcogenides. *2D Materials* **6,** 025026 (2019).

110. Horng, J., Stroucken, T., Zhang, L., *et al.* Observation of interlayer excitons in $MoSe_2$ single crystals. *Phys. Rev. B* **97,** 241404 (2018).

111. Shree, S., Paradisanos, I., Marie, X., *et al.* Guide to optical spectroscopy of layered semiconductors. *Nature Reviews Physics* **3,** 39–54 (2021).

112. Förg, M. *Confocal and cavity-enhanced spectroscopy of semiconductor van der Waals heterostructures* PhD thesis (Ludwig-Maximilians-Universität München, 2020).

113. Tomasz, W., Paulo, E. F. J., Seifert, G., *et al.* Exciton g-factors of van der Waals heterostructures from first-principles calculations. *Phys. Rev. B* **101,** 235408 (2020).

114. Jena, D. Bloch Theorem, Bandstructure, and Quantum Currents (Oxford University Press, 2022).

115. Faria Junior, P. E., Tedeschi, D., De Luca, M., *et al.* Common nonlinear features and spin-orbit coupling effects in the Zeeman splitting of novel wurtzite materials. *Phys. Rev. B* **99,** 195205 (2019).

116. Wang, G., Bouet, L., Glazov, M. M., *et al.* Magneto-optics in transition metal diselenide monolayers. *2D Materials* **2,** 034002 (2015).

117. Landau, L. D. & Lifshitz, L. M. Quantum Mechanics Non-Relativistic Theory, Third Edition: Volume 3 (Butterworth-Heinemann, 1981).

118. Andor, K., Péter, R. & Guido, B. Landau levels and Shubnikov-de Haas oscillations in monolayer transition metal dichalcogenide semiconductors. *New Journal of Physics* **17,** 103006 (2015).

119. Bechstedt, F. Superlattices and other heterostructures, symmetry and optical phenomena. *Zeitschrift für Physikalische Chemie* **193,** 223–224 (1996).

120. Faria Junior, P. E., Kurpas, M., Gmitra, M., *et al.* K·p theory for phosphorene: Effective g-factors, Landau levels, and excitons. *Phys. Rev. B* **100,** 115203 (2019).

121. Gawarecki, K. & Zieliński, M. Electron g-factor in nanostructures: continuum media and atomistic approach. *Sci. Rep.* **10,** 22001 (2020).

122. Kiselev, A. A., Ivchenko, E. L. & Rössler, U. Electron g-factor in one- and zero-dimensional semiconductor nanostructures. *Phys. Rev. B* **58,** 16353–16359 (1998).

123. Eissfeller, T. *Theory of the Electronic Structure of Quantum Dots in External Fields* PhD thesis (Technische Universität München, 2012).

124. Roth, L. M., Lax, B. & Zwerdling, S. Theory of optical magneto-absorption effects in semiconductors. *Phys. Rev.* **114,** 90–104 (1959).

125. Bir, G. L. & Pikus, G. E. Symmetry and strain-induced effects in semiconductors (Wiley New York, 1974).

126. Xiao, D., Chang, M.-C. & Niu, Q. Berry phase effects on electronic properties. *Rev. Mod. Phys.* **82,** 1959–2007 (2010).

127. Wang, Q. H., Kalantar-Zadeh, K., Kis, A., *et al.* Electronics and optoelectronics of two-dimensional transition metal dichalcogenides. *Nature Nanotechnology* **7,** 699–712 (2012).

128. Berry, M. V. Quantal phase factors accompanying adiabatic changes. *Proc. R. Soc. A* **392,** 45–57 (1984).

129. Kumar, H., Er, D., Dong, L., *et al.* Elastic deformations in 2D van der Waals heterostructures and their impact on optoelectronic properties: predictions from a multiscale computational approach. *Sci. Rep.* **5,** 10872 (2015).

130. Wu, F., Lovorn, T., Tutuc, E., *et al.* Hubbard model physics in transition metal dichalcogenide moiré bands. *Phys. Rev. Lett.* **121,** 026402 (2018).

131. Liu, Y., Zeng, C., Yu, J., *et al.* Moiré superlattices and related moiré excitons in twisted van der Waals heterostructures. *Chem. Soc. Rev.* **50,** 6401–6422 (2021).

132. Zhu, S. & Johnson, H. T. Moiré-templated strain patterning in transition-metal dichalcogenides and application in twisted bilayer MoS_2. *Nanoscale* **10,** 20689–20701 (2018).

133. Yu, H., Liu, G.-B. & Yao, W. Brightened spin-triplet interlayer excitons and optical selection rules in van der Waals heterobilayers. *2D Materials* **5,** 035021 (2018).

134. Huang, D., Choi, J., Shih, C.-K., *et al.* Excitons in semiconductor moiré superlattices. *Nature Nanotechnology* **17,** 227–238 (2022).

135. Zhang, L., Zhang, Z., Wu, F., *et al.* Twist-angle dependence of moiré excitons in WS_2/$MoSe_2$ heterobilayers. *Nature Communications* **11,** 5888 (2020).

136. Yuan, L., Zheng, B., Kunstmann, J., *et al.* Twist-angle-dependent interlayer exciton diffusion in WS_2-WSe_2 heterobilayers. *Nature Materials* **19,** 617–623 (2020).

137. Kang, J., Tongay, S., Zhou, J., *et al.* Band offsets and heterostructures of two-dimensional semiconductors. *Appl. Phys. Lett.* **102,** 012111 (2013).

138. Ding, Y., Wang, Y., Ni, J., *et al.* First principles study of structural, vibrational and electronic properties of graphene-like MX_2 (M=Mo, Nb, W, Ta; X=S, Se, Te) monolayers. *Physica B: Condensed Matter* **406,** 2254–2260 (2011).

139. Zeller, P. & Günther, S. What are the possible moiré patterns of graphene on hexagonally packed surfaces? universal solution for hexagonal coincidence lattices, derived by a geometric construction. *New Journal of Physics* **16,** 083028 (2014).

140. Zeller, P., Ma, X. & Günther, S. Indexing moiré patterns of metal-supported graphene and related systems: strategies and pitfalls. *New Journal of Physics* **19,** 013015 (2017).

141. Wang, J., Shi, Q., Shih, E.-M., *et al.* Diffusivity reveals three distinct phases of interlayer excitons in $MoSe_2$/WSe_2 heterobilayers. *Phys. Rev. Lett.* **126,** 106804 (2021).

142. Nayak, P. K., Horbatenko, Y., Ahn, S., *et al.* Probing evolution of twist-angle-dependent interlayer excitons in $MoSe_2$/WSe_2 van der Waals heterostructures. *ACS Nano* **11,** 4041–4050 (2017).

143. Choi, J., Florian, M., Steinhoff, A., *et al.* Twist angle-dependent interlayer exciton lifetimes in van der Waals heterostructures. *Phys. Rev. Lett.* **126,** 047401 (2021).

144. Cao, Y., Fatemi, V., Demir, A., *et al.* Correlated insulator behaviour at half-filling in magic-angle graphene superlattices. *Nature* **556,** 80–84 (2018).

145. Cao, Y., Fatemi, V., Fang, S., *et al.* Unconventional superconductivity in magic-angle graphene superlattices. *Nature* **556,** 43–50 (2018).

146. Nieken, R., Roche, A., Mahdikhanysarvejahany, F., *et al.* Direct STM measurements of R-type and H-type twisted $MoSe_2$/WSe_2. *APL Materials* **10,** 031107 (2022).

147. Weston, A., Castanon, E. G., Enaldiev, V., *et al.* Interfacial ferroelectricity in marginally twisted 2D semiconductors. *Nature Nanotechnology* **17,** 390–395 (2022).

148. Weston, A. Introduction to 2-dimensional materials and moiré superlattices, 5–28 (Springer International Publishing, 2022).

149. Cao, W., Hod, O. & Urbakh, M. Interlayer registry index of layered transition metal dichalcogenides. *J. Phys. Chem. Lett.* **13,** 3353–3359 (2022).

150. Choi, J., Hsu, W.-T., Lu, L.-S., *et al.* Moiré potential impedes interlayer exciton diffusion in van der Waals heterostructures. *Sci. Adv.* **6,** eaba8866 (2020).

151. Förg, M., Colombier, L., Patel, R. K., *et al.* Cavity-control of interlayer excitons in van der Waals heterostructures. *Nature Communications* **10,** 3697 (2019).

152. Koster, G., Dimmock, J. & Wheeler, R. Properties of the Thirty-Two Point Groups (M. I. T. Press, 1963).

153. Glazov, M. M., Amand, T., Marie, X., *et al.* Exciton fine structure and spin decoherence in monolayers of transition metal dichalcogenides. *Phys. Rev. B* **89,** 201302 (2014).

154. Yu, H., Wang, Y., Tong, Q., *et al.* Anomalous light cones and valley optical selection rules of interlayer excitons in twisted heterobilayers. *Phys. Rev. Lett.* **115,** 187002 (2015).

155. Zhang, L., Gogna, R., Burg, G. W., *et al.* Highly valley-polarized singlet and triplet interlayer excitons in van der Waals heterostructure. *Phys. Rev. B* **100,** 041402 (2019).

156. Mahdikhanysarvejahany, F., Shanks, D. N., Muccianti, C., *et al.* Temperature dependent moiré trapping of interlayer excitons in $MoSe_2$-WSe_2 heterostructures. *npj 2D Materials and Applications* **5,** 67 (2021).

157. Kresse, G. & Furthmüller, J. Efficient iterative schemes for ab initio total-energy calculations using a plane-wave basis set. *Phys. Rev. B* **54,** 11169–11186 (1996).

158. Grimme, S., Ehrlich, S. & Goerigk, L. Effect of the damping function in dispersion corrected density functional theory. *J. Comput. Chem.* **32,** 1456–1465 (2011).

159. Sangwan, V. K., Lee, H.-S., Bergeron, H., *et al.* Multi-terminal memtransistors from polycrystalline monolayer molybdenum disulfide. *Nature* **554,** 500–504 (2018).

160. Yin, Z., Li, H., Li, H., *et al.* Single-layer MoS_2 phototransistors. *ACS Nano* **6,** 74–80 (2012).

161. Li, N., Wang, Q., Shen, C., *et al.* Large-scale flexible and transparent electronics based on monolayer molybdenum disulfide field-effect transistors. *Nature Electronics* **3,** 711–717 (2020).

162. Cai, Z., Liu, B., Zou, X., *et al.* Chemical vapor deposition growth and applications of two-dimensional materials and their heterostructures. *Chemical Reviews* **118,** 6091–6133 (2018).

163. Novoselov, K. S., Geim, A. K., Morozov, S. V., *et al.* Two-dimensional gas of massless dirac fermions in graphene. *Nature* **438,** 197–200 (2005).

164. Allen, M. J., Tung, V. C. & Kaner, R. B. Honeycomb carbon: a review of graphene. *Chem. Rev.* **110,** 132–145 (2010).

165. Budania, P., Baine, P. T., Montgomery, J. H., *et al.* Comparison between scotch tape and gel-assisted mechanical exfoliation techniques for preparation of 2D transition metal dichalcogenide flakes. *Micro Nano Lett.* **12,** 970–973 (2017).

166. Liu, X., Galfsky, T., Sun, Z., *et al.* Strong light-matter coupling in two-dimensional atomic crystals. *Nature Photonics* **9,** 30–34 (2015).

167. Yuan, L., Ge, J., Peng, X., *et al.* A reliable way of mechanical exfoliation of large scale two-dimensional materials with high quality. *AIP Advances* **6,** 125201 (2016).

168. Huang, Y., Pan, Y.-H., Yang, R., *et al.* Universal mechanical exfoliation of large-area 2D crystals. *Nature Communications* **11,** 2453 (2020).

169. Li, H., Wu, J., Yin, Z., *et al.* Preparation and applications of mechanically exfoliated single-layer and multilayer MoS_2 and WSe_2 nanosheets. *Acc. Chem. Res.* **47,** 1067–1075 (2014).

170. Zhang, Y., Yao, Y., Sendeku, M. G., *et al.* Recent progress in CVD growth of 2D transition metal dichalcogenides and related heterostructures. *Adv. Mater.* **31,** 1901694 (2019).

171. Huo, C., Yan, Z., Song, X., *et al.* 2D materials via liquid exfoliation: a review on fabrication and applications. *Science Bulletin* **60,** 1994–2008 (2015).

172. Adilbekova, B., Lin, Y., Yengel, E., *et al.* Liquid phase exfoliation of MoS_2 and WS_2 in aqueous ammonia and their application in highly efficient organic solar cells. *J. Mater. Chem. C* **8,** 5259–5264 (2020).

173. Li, Z., Young, R. J., Backes, C., *et al.* Mechanisms of liquid-phase exfoliation for the production of graphene. *ACS Nano* **14,** 10976–10985 (2020).

174. Coleman, J. N., Lotya, M., O'Neill, A., *et al.* Two-dimensional nanosheets produced by liquid exfoliation of layered materials. *Science* **331,** 568–571 (2011).

175. Sun, L., Yuan, G., Gao, L., *et al.* Chemical vapour deposition. *Nature Reviews Methods Primers* **1,** 5 (2021).

176. Han, Z., Zhang, R., Li, M., *et al.* Recent advances in the controlled chemical vapor deposition growth of bilayer 2D single crystals. *J. Mater. Chem. C* (2022).

177. Wang, Z., Xu, W., Li, B., *et al.* Selective chemical vapor deposition growth of WS_2/MoS_2 vertical on gold foils, lateral heterostructures. *Nanomaterials* **12** (2022).

178. Maduro, L., Noordam, M., Bolhuis, M., *et al.* Position-controlled fabrication of vertically aligned Mo/MoS_2 core-shell nanopillar arrays. *Adv. Funct. Mater.* **32,** 2107880 (2022).

179. Li, J. & Östling, M. Scalable fabrication of 2D semiconducting crystals for future electronics. *Electronics* **4,** 1033–1061 (2015).

180. Zhang, Z., Chen, P., Yang, X., *et al.* Ultrafast growth of large single crystals of monolayer WS_2 and WSe_2. *National Science Review* **7,** 737–744 (2020).

181. Rashid, H., Yu, K., Muhammad Naveed, U., *et al.* Catalyst role in chemical vapor deposition (CVD) process: a review. *Reviews on Advanced Materials Science* **40,** 235–248 (2015).

182. Shinde, V. M., Deivendran, B., Kumar, H., *et al.* Investigation of transport processes in a commercial hot wall CVD reactor with multi-substrates for high-quality pyrocarbon deposition. *Surface and Coatings Technology* **425,** 127685 (2021).

183. Sønsteby, H. H., Yanguas-Gil, A. & Elam, J. W. Consistency and reproducibility in atomic layer deposition. *Journal of Vacuum Science Technology A* **38,** 020804 (2020).

184. You, J., Hossain, M. D. & Luo, Z. Synthesis of 2D transition metal dichalcogenides by chemical vapor deposition with controlled layer number and morphology. *Nano Convergence* **5,** 26 (2018).

185. Li, S., Wang, S., Tang, D.-M., *et al.* Halide-assisted atmospheric pressure growth of large WSe_2 and WS_2 monolayer crystals. *Applied Materials Today* **1,** 60–66 (2015).

186. Bilgin, I., Liu, F., Vargas, A., *et al.* Chemical vapor deposition synthesized atomically thin molybdenum disulfide with optoelectronic-grade crystalline quality. *ACS Nano* **9,** 8822–8832 (2015).

187. Li, X., Kahn, E., Chen, G., *et al.* Surfactant-mediated growth and patterning of atomically thin transition metal dichalcogenides. *ACS Nano* **14,** 6570–6581 (2020).

188. Liu, B., Fathi, M., Chen, L., *et al.* Chemical vapor deposition growth of monolayer WSe_2 with tunable device characteristics and growth mechanism study. *ACS Nano* **9,** 6119–6127 (2015).

189. He, Y., Sobhani, A., Lei, S., *et al.* Layer engineering of 2D semiconductor junctions. *Adv. Mater.* **28,** 5126–5132 (2016).

190. Yu, Y., Li, C., Liu, Y., *et al.* Controlled scalable synthesis of uniform, high-quality monolayer and few-layer MoS_2 films. *Sci. Rep.* **3,** 1866 (2013).

191. Elias, A. L., Perea-Lopez, N., Castro-Beltran, A., *et al.* Controlled synthesis and transfer of large-area WS_2 sheets: from single layer to few layers. *ACS Nano* **7,** 5235–5242 (2013).

192. Chen, Z., Ren, W., Gao, L., *et al.* Three-dimensional flexible and conductive interconnected graphene networks grown by chemical vapour deposition. *Nature Materials* **10,** 424–428 (2011).

193. Gao, L., Ren, W., Zhao, J., *et al.* Efficient growth of high-quality graphene films on Cu foils by ambient pressure chemical vapor deposition. *Appl. Phys. Lett.* **97,** 183109 (2010).

194. Liu, H., Zhu, Y., Meng, Q.-L., *et al.* Role of the carrier gas flow rate in monolayer MoS_2 growth by modified chemical vapor deposition. *Nano Research* **10** (2016).

195. Panahi, A., Sun, X., Song, G., *et al.* On the influences of carrier gas type and flow rate on CVD synthesis of CNTs from postconsumer polyethylene. *Ind. Eng. Chem. Res.* **59,** 14004–14014 (2020).

196. Zhu, Z., You, J., Zhu, D., *et al.* Effect of precursor ratio on the morphological and optical properties of CVD-grown monolayer MoS_2 nanosheets. *Materials Research Express* **8,** 045008 (2021).

197. Singh, A., Moun, M. & Singh, R. Effect of different precursors on CVD growth of molybdenum disulfide. *Journal of Alloys and Compounds* **782,** 772–779 (2019).

198. Iliescu, C., Avram, M., Chen, B., *et al.* Residual stress in thin films PECVD depositions: A review. *Journal of Optoelectronics and Advanced Materials* **13,** 387–394 (2011).

199. Manasevit, H. M. Recollections and reflections of MO-CVD. *Journal of Crystal Growth* **55,** 1–9 (1981).

200. Choi, W., Choudhary, N., Han, G. H., *et al.* Recent development of two-dimensional transition metal dichalcogenides and their applications. *Materials Today* **20,** 116–130 (2017).

201. Butt, M. A., Tyszkiewicz, C., Karasiński, P., *et al.* Optical thin films fabrication techniques-towards a low-cost solution for the integrated photonic platform: a review of the current status. *Materials* **15** (2022).

202. Bilgin, I., Raeliarijaona, A. S., Lucking, M. C., *et al.* Resonant Raman and exciton coupling in high-quality single crystals of atomically thin molybdenum diselenide grown by vapor-phase chalcogenization. *ACS Nano* **12,** 740–750 (2018).

203. Zhou, J., Lin, J., Huang, X., *et al.* A library of atomically thin metal chalcogenides. *Nature* **556,** 355–359 (2018).

204. Cadiz, F., Courtade, E., Robert, C., *et al.* Excitonic linewidth approaching the homogeneous limit in MoS_2 based van der Waals heterostructures : accessing spin-valley dynamics. *Phys. Rev. X* **7,** 021026 (2017).

205. Purdie, D. G., Pugno, N. M., Taniguchi, T., *et al.* Cleaning interfaces in layered materials heterostructures. *Nature Communications* **9,** 5387 (2018).

206. Zhao, W., Ribeiro, R. M., Toh, M., *et al.* Origin of indirect optical transitions in few-layer MoS_2, WS_2, and WSe_2. *Nano Lett.* **13,** 5627–5634 (2013).

207. Arora, A., Drüppel, M., Schmidt, R., *et al.* Interlayer excitons in a bulk van der Waals semiconductor. *Nature Communications* **8,** 639 (2017).

208. Wang, L., Shih, E.-M., Ghiotto, A., *et al.* Correlated electronic phases in twisted bilayer transition metal dichalcogenides. *Nature Materials* **19,** 861–866 (2020).

209. Merkl, P., Mooshammer, F., Brem, S., *et al.* Twist-tailoring coulomb correlations in van der Waals homobilayers. *Nature Communications* **11,** 2167 (2020).

210. Calman, E. V., Fogler, M. M., Butov, L. V., *et al.* Indirect excitons in van der Waals heterostructures at room temperature. *Nature Communications* **9,** 1895 (2018).

211. Deilmann, T. & Thygesen, K. S. Interlayer excitons with large optical amplitudes in layered van der Waals materials. *Nano Lett.* **18,** 2984–2989 (2018).

212. Leisgang, N., Shree, S., Paradisanos, I., *et al.* Giant stark splitting of an exciton in bilayer $MoS2_2$. *Nature Nanotechnology* **15,** 901–907 (2020).

213. Peimyoo, N., Deilmann, T., Withers, F., *et al.* Electrical tuning of optically active interlayer excitons in bilayer MoS_2. *Nature Nanotechnology* **16,** 888–893 (2021).

214. Lorchat, E., Selig, M., Katsch, F., *et al.* Excitons in bilayer MoS_2 displaying a colossal electric field splitting and tunable magnetic response. *Phys. Rev. Lett.* **126,** 037401 (2021).

215. Liu, Y., Dini, K., Tan, Q., *et al.* Electrically controllable router of interlayer excitons. *Sci. Adv.* **6,** 1830 (2020).

216. Hsu, W.-T., Lin, B.-H., Lu, L.-S., *et al.* Tailoring excitonic states of van der Waals bilayers through stacking configuration, band alignment, and valley spin. *Sci. Adv.* **5,** eaax7407 (2022).

217. Hsu, W.-T., Quan, J., Pan, C.-R., *et al.* Quantitative determination of interlayer electronic coupling at various critical points in bilayer MoS_2. *Phys. Rev. B* **106,** 125302 (2022).

218. Liu, K., Zhang, L., Cao, T., *et al.* Evolution of interlayer coupling in twisted molybdenum disulfide bilayers. *Nature Communications* **5,** 4966 (2014).

219. Schneider, L. M., Kuhnert, J., Schmitt, S., *et al.* Spin-layer and spin-valley locking in CVD-grown AA'- and AB-stacked tungsten-disulfide bilayers. *J. Phys. Chem. C* **123,** 21813–21821 (2019).

220. Du, L., Zhang, Q., Zhang, T., *et al.* Robust circular polarization of indirect Q-K transitions in bilayer 3R-WS_2. *Phys. Rev. B* **100,** 161404 (2019).

221. Magorrian, S. J., Enaldiev, V. V., Zólyomi, V., *et al.* Multifaceted moiré superlattice physics in twisted WSe_2 bilayers. *Phys. Rev. B* **104,** 125440 (2021).

222. Gerber, I. C., Courtade, E., Shree, S., *et al.* Interlayer excitons in bilayer MoS_2 with strong oscillator strength up to room temperature. *Phys. Rev. B* **99,** 035443 (2019).

223. Li, H., Lu, G., Wang, Y., *et al.* Mechanical exfoliation and characterization of single- and few-layer nanosheets of WSe_2, TaS_2, and $TaSe_2$. *Small* **9,** 1974–1981 (2013).

224. Zeng, H., Liu, G.-B., Dai, J., *et al.* Optical signature of symmetry variations and spin-valley coupling in atomically thin tungsten dichalcogenides. *Sci. Rep.* **3,** 1608 (2013).

225. Sahin, H., Tongay, S., Horzum, S., *et al.* Anomalous Raman spectra and thickness-dependent electronic properties of WSe_2. *Phys. Rev. B* **87,** 165409 (2013).

226. Luo, X., Zhao, Y., Zhang, J., *et al.* Effects of lower symmetry and dimensionality on Raman spectra in two-dimensional WSe_2. *Phys. Rev. B* **88,** 195313 (2013).

227. Terrones, H., Corro, E. D., Feng, S., *et al.* New first order Raman-active modes in few layered transition metal dichalcogenides. *Sci. Rep.* **4,** 4215 (2014).

228. Puretzky, A. A., Liang, L., Li, X., *et al.* Low-frequency Raman fingerprints of two-dimensional metal dichalcogenide layer stacking configurations. *ACS Nano* **9,** 6333–6342 (2015).

229. Li, Y., Chernikov, A., Zhang, X., *et al.* Measurement of the optical dielectric function of monolayer transition-metal dichalcogenides: MoS_2, $MoSe_2$, WS_2, and WSe_2. *Phys. Rev. B* **90,** 205422 (2014).

230. Rigosi, A. F., Hill, H. M., Li, Y., *et al.* Probing interlayer interactions in transition metal dichalcogenide heterostructures by optical spectroscopy: MoS_2/WS_2 and $MoSe_2/WSe_2$. *Nano Lett.* **15,** 5033–5038 (2015).

231. Ajayi, O. A., Ardelean, J. V., Shepard, G. D., *et al.* Approaching the intrinsic photoluminescence linewidth in transition metal dichalcogenide monolayers. *2D Materials* **4,** 031011 (2017).

232. Wierzbowski, J., Klein, J., Sigger, F., *et al.* Direct exciton emission from atomically thin transition metal dichalcogenide heterostructures near the lifetime limit. *Sci. Rep.* **7,** 12383– (2017).

233. Shree, S., George, A., Lehnert, T., *et al.* High optical quality of MoS_2 monolayers grown by chemical vapor deposition. *2D Materials* **7,** 015011 (2019).

234. You, Y., Zhang, X.-X., Berkelbach, T. C., *et al.* Observation of biexcitons in monolayer WSe_2. *Nature Physics* **11,** 477–481 (2015).

235. Barbone, M., Montblanch, A. R.-P., Kara, D. M., *et al.* Charge-tuneable biexciton complexes in monolayer WSe_2. *Nature Communications* **9,** 3721 (2018).

236. Steinhoff, A., Florian, M., Singh, A., *et al.* Biexciton fine structure in monolayer transition metal dichalcogenides. *Nature Physics* **14,** 1199–1204 (2018).

237. Li, Z., Wang, T., Lu, Z., *et al.* Revealing the biexciton and trion-exciton complexes in BN encapsulated WSe_2. *Nature Communications* **9,** 3719 (2018).

238. Ye, Z., Waldecker, L., Ma, E. Y., *et al.* Efficient generation of neutral and charged biexcitons in encapsulated WSe_2 monolayers. *Nature Communications* **9,** 3718 (2018).

239. Arora, A., Koperski, M., Nogajewski, K., *et al.* Excitonic resonances in thin films of WSe_2: from monolayer to bulk material. *Nanoscale* **7,** 10421–10429 (2015).

240. Wickramaratne, D., Zahid, F. & Lake, R. K. Electronic and thermoelectric properties of few-layer transition metal dichalcogenides. *J. Chem. Phys.* **140,** 124710 (2014).

241. Aivazian, G., Gong, Z., Jones, A. M., *et al.* Magnetic control of valley pseudospin in monolayer WSe_2. *Nature Physics* **11,** 148–152 (2015).

242. Srivastava, A., Sidler, M., Allain, A. V., *et al.* Valley Zeeman effect in elementary optical excitations of monolayer WSe_2. *Nature Physics* **11,** 141–147 (2015).

243. Koperski, M., Molas, M. R., Arora, A., *et al.* Orbital, spin and valley contributions to Zeeman splitting of excitonic resonances in $MoSe_2$, WSe_2 and WS_2 monolayers. *2D Materials* **6,** 015001 (2018).

244. Wozniak, T., Faria Junior, P. E., Seifert, G., *et al.* Exciton g-factors of van der Waals heterostructures from first-principles calculations. *Phys. Rev. B* **101,** 235408 (2020).

245. Deilmann, T., Krüger, P. & Rohlfing, M. Ab initio studies of exciton g-factors: monolayer transition metal dichalcogenides in magnetic fields. *Phys. Rev. Lett.* **124,** 226402 (2020).

246. Xuan, F. & Quek, S. Y. Valley Zeeman effect and Landau levels in two-dimensional transition metal dichalcogenides. *Phys. Rev. Research* **2,** 033256 (2020).

247. Tang, Y., Li, L., Li, T., *et al.* Simulation of Hubbard model physics in WSe_2/WS_2 moiré superlattices. *Nature* **579,** 353–358 (2020).

248. Huang, X., Wang, T., Miao, S., *et al.* Correlated insulating states at fractional fillings of the WS_2/WSe_2 moiré lattice. *Nature Physics* **17,** 715–719 (2021).

249. Ghiotto, A., Shih, E.-M., Pereira, G. S. S. G., *et al.* Quantum criticality in twisted transition metal dichalcogenides. *Nature* **597,** 345–349 (2021).

250. Li, T., Jiang, S., Li, L., *et al.* Continuous Mott transition in semiconductor moiré superlattices. *Nature* **597,** 350–354 (2021).

251. Regan, E. C., Wang, D., Jin, C., *et al.* Mott and generalized Wigner crystal states in WSe_2/WS_2 moiré superlattices. *Nature* **579,** 359–363 (2020).

252. Shimazaki, Y., Schwartz, I., Watanabe, K., *et al.* Strongly correlated electrons and hybrid excitons in a moiré heterostructure. *Nature* **580,** 472–477 (2020).

253. Xu, Y., Liu, S., Rhodes, D. A., *et al.* Correlated insulating states at fractional fillings of moiré superlattices. *Nature* **587,** 214–218 (2020).

254. Zhang, X.-X., Cao, T., Lu, Z., *et al.* Magnetic brightening and control of dark excitons in monolayer WSe_2. *Nature Nanotechnology* **12,** 883–888 (2017).

255. Li, H., Li, S., Regan, E. C., *et al.* Imaging two-dimensional generalized Wigner crystals. *Nature* **597,** 650–654 (2021).

256. Zhang, N., Surrente, A., Baranowski, M., *et al.* Moiré intralayer excitons in a $MoSe_2/MoS_2$ heterostructure. *Nano Lett.* **18,** 7651–7657 (2018).

257. Joe, A. Y., Jauregui, L. A., Pistunova, K., *et al.* Electrically controlled emission from singlet and triplet exciton species in atomically thin light-emitting diodes. *Phys. Rev. B* **103,** L161411 (2021).

258. Ciarrocchi, A., Unuchek, D., Avsar, A., *et al.* Polarization switching and electrical control of interlayer excitons in two-dimensional van der Waals heterostructures. *Nature Photonics* **13,** 131 (2019).

259. Brotons-Gisbert, M., Baek, H., Molina-Sánchez, A., *et al.* Spin-layer locking of interlayer excitons trapped in moiré potentials. *Nature Materials* **19,** 630–636 (2020).

260. McGilly, L. J., Kerelsky, A., Finney, N. R., *et al.* Visualization of moiré superlattices. *Nature Nanotechnology* **15,** 580–584 (2020).

261. Pizzocchero, F., Gammelgaard, L., Jessen, B. S., *et al.* The hot pick-up technique for batch assembly of van der Waals heterostructures. *Nature Communications* **7,** 1–10 (2016).

262. Neumann, A., Lindlau, J., Colombier, L., *et al.* Opto-valleytronic imaging of atomically thin semiconductors. *Nature Nanotechnology* **12,** 329–334 (2017).

263. Alexeev, E. M., Ruiz-Tijerina, D. A., Danovich, M., *et al.* Resonantly hybridized excitons in moiré superlattices in van der Waals heterostructures. *Nature* **567,** 81–86 (2019).

264. Alexeev, E. M., Mullin, N., Ares, P., *et al.* Emergence of highly linearly polarized interlayer exciton emission in $MoSe_2/WSe_2$ heterobilayers with transfer-induced layer corrugation. *ACS Nano* **14,** 11110–11119 (2020).

265. Holler, J., Meier, S., Kempf, M., *et al.* Low-frequency Raman scattering in WSe_2-$MoSe_2$ heterobilayers: evidence for atomic reconstruction. *Appl. Phys. Lett.* **117,** 013104 (2020).

266. Wang, T., Miao, S., Li, Z., *et al.* Giant valley-Zeeman splitting from spin-singlet and spin-triplet interlayer excitons in $WSe_2/MoSe_2$ heterostructure. *Nano Lett.* **20,** 694–700 (2020).

267. Semina, M. A., Glazov, M. M. & Sherman, E. Interlayer exciton-polaron in atomically thin semiconductors. *Annalen Der Physik* **532,** 2000339 (2020).

268. Cao, L., White, J. S., Park, J.-S., *et al.* Engineering light absorption in semiconductor nanowire devices. *Nature Materials* **8,** 643–647 (2009).

269. Tang, Y., Gu, J., Liu, S., *et al.* Dielectric catastrophe at the Wigner-Mott transition in a moiré superlattice. *Nature Communications* **13,** 4271 (2022).

270. Naik, M. H., Regan, E. C., Zhang, Z., *et al.* Intralayer charge-transfer moiré excitons in van der Waals superlattices. *Nature* **609,** 52–57 (2022).

271. Xia, J., Yan, J., Wang, Z., *et al.* Strong coupling and pressure engineering in WSe_2-$MoSe_2$ heterobilayers. *Nature Physics* **17,** 92–98 (2021).

272. Butov, L. Excitonic devices. *Superlattices and Microstructures* **108.** Indirect Excitons: Physics and Applications, 2–26 (2017).

273. Sun, Z., Ciarrocchi, A., Tagarelli, F., *et al.* Excitonic transport driven by repulsive dipolar interaction in a van der Waals heterostructure. *Nature Photonics* **16,** 79–85 (2022).

274. Shanks, D. N., Mahdikhanysarvejahany, F., Stanfill, T. G., *et al.* Interlayer exciton diode and transistor. *Nano Lett.* **22,** 6599–6605 (2022).

275. Jiang, Y., Chen, S., Zheng, W., *et al.* Interlayer exciton formation, relaxation, and transport in TMD van der Waals heterostructures. *Light: Science & Applications* **10,** 72 (2021).

276. Ciarrocchi, A., Tagarelli, F., Avsar, A., *et al.* Excitonic devices with van der waals heterostructures: valleytronics meets twistronics. *Nature Reviews Materials* **7,** 449–464 (2022).

277. Shanks, D. N., Mahdikhanysarvejahany, F., Koehler, M. R., *et al.* Single-exciton trapping in an electrostatically defined two-dimensional semiconductor quantum dot. *Phys. Rev. B* **106,** L201401 (2022).

278. Shi, L.-k., Ma, J. & Song, J. C. W. Gate-tunable flat bands in van der Waals patterned dielectric superlattices. *2D Materials* **7,** 015028 (2019).

279. Liu, H., Hussain, S., Ali, A., *et al.* A vertical WSe_2-$MoSe_2$ p-n heterostructure with tunable gate rectification. *RSC Adv.* **8,** 25514–25518 (2018).

280. Mahdikhanysarvejahany, F., Shanks, D. N., Klein, M., *et al.* Localized interlayer excitons in $MoSe_2$-WSe_2 heterostructures without a moiré potential. *Nature communications* **13,** 5354 (2022).

281. Brotons-Gisbert, M., Baek, H., Campbell, A., *et al.* Moiré-trapped interlayer trions in a charge-tunable WSe_2/$MoSe_2$ heterobilayer. *Phys. Rev. X* **11,** 031033 (2021).

282. Robert, C., Amand, T., Cadiz, F., *et al.* Fine structure and lifetime of dark excitons in transition metal dichalcogenide monolayers. *Phys. Rev. B* **96,** 155423 (2017).

283. Chen, X., Lu, X., Dubey, S., *et al.* Entanglement of single-photons and chiral phonons in atomically thin WSe_2. *Nature Physics* **15,** 221–227 (2019).

284. Woods, C. R., Britnell, L., Eckmann, A., *et al.* Commensurate-incommensurate transition in graphene on hexagonal boron nitride. *Nature Physics* **10,** 451–456 (2014).

285. Ma, X., Fu, S., Ding, J., *et al.* Robust interlayer exciton in WS_2/$MoSe_2$ van der Waals heterostructure under high pressure. *Nano Lett.* **21,** 8035–8042 (2021).

286. Zhao, W., Shen, B., Tao, Z., *et al.* Gate-tunable heavy fermions in a moiré Kondo lattice. *arXiv preprint.* arXiv: 2211.00263 (2022).

287. Xu, Y., Kang, K., Watanabe, K., *et al.* A tunable bilayer Hubbard model in twisted WSe_2. *Nature Nanotechnology* **17,** 934–939 (2022).

List of Publications

P1. Li, Z., Förste, J., Watanabe, K., Taniguchi, T., Urbaszek, B., Baimuratov, A. S., Gerber, I. C., Högele, A. & Bilgin, I. Stacking-dependent exciton multiplicity in WSe_2 bilayers. *Phys. Rev. B* **106,** 045411 (2022).

P2. Zhao, S., Li, Z., Huang, X., Rupp, A., Göser, J., Vovk, I., Kruchinin, S., Watanabe, K., Taniguchi, T., Bilgin, I., Baimuratov, A. & Högele, A. Excitons in mesoscopically reconstructed moiré hetersotructures. *arXiv preprint.* arXiv: 2202.11139 (2022).

P3. Li, Z., Tabataba-Vakili, F., Zhao, S., Rupp, A., Bilgin, I., Herdegen, Z., März, B., Watanabe, K., Taniguchi, T., Schleder, G. R., Baimuratov, A. S., Kaxiras, E., Müller-Caspary, K. & Högele, A. Lattice reconstruction in $MoSe_2$-WSe_2 heterobilayers synthesized by chemical vapor deposition. *arXiv preprint.* arXiv: 2212.07686 (2022).

List of Abbreviations

2D	two-dimensional
BL	homobilayer
CBM	conduction band minimum
CVD	chemical vapor deposition
DFT	density functional theory
DR	differential reflectance
FWHM	full-width at half-maximum
HBL	heterobilayer
hBN	hexagonal boron nitride
ML	monolayer
MoO_2	molybdenum dioxide
MoO_3	molybdenum trioxide
NaCl	sodium chloride
P_c	degree of circular polarization
P_l	degree of linear polarization
PC	poly-Bisphenol A-carbonat
PDMS	polydimethylsiloxane
PVD	physical vapor deposition
sccm	standard cubic centimeters per minute
Se	selenium
Si	silicon
SiO_2	silicon dioxide
TMD	transition metal dichalchogenide
VBM	valence band maximum
WO_2	tungsten dioxide
WS_2	tungsten disulfide
WSe_2	tungsten diselenide

Acknowledgments

I realize that my PhD life will come to the end when I am writing this part. This is definitely beautiful and meaningful four years of my life and I really appreciate many things that have happened and everyone who has helped and supported me over the past few years.

My deepest and sincerest gratitude goes to Alexander Högele, who is an amazing tutor. Thank you so much for giving me the opportunity to be part of our group and for providing me with all the experimental conditions. Many inspiring scientific discussions with you and your patience and encourage made me enjoy working in our group. I have made great progress with your patient and rigorous guidance. Your support was definitely determining in the success of my thesis. Moreover, thank you very much for providing me with a relaxing and pleasant working environment. You always give me enough time to complete each project, which keeps me happy during the whole period of experiments.

I have to thank our Postdocs for the collaborative work environment: Anvar Baimuratov, Farsane Tabataba-Vakili, Ismail Bilgin, Samarth Vadia, Shen Zhao, Subhradeep Misra, and Xin Huang. Thank you Anvar for your rich theoretical knowledge and calculations to explain the experimental results. Thank you Ismail for bringing me to the CVD-grown TMDs world and providing many precious suggestions. Thank you Samarth for helping me with lots of daily problems. Thank you Shen for helping me solve every question and problem that I bothered you frequently over the years and teaching me lots of great stuff in the theory and in the experiments. Thank you Xin for teaching me all of the sample preparation techniques and giving me a lot of significant suggestions during the experiments.

I would like to express my appreciation to all of our group members for many scientific discussions: Anna Rupp, Borislav Polovnikov, Johannes Scherzer, Jonas Göser, Jonathan Förste, Julian Trapp, Lukas Husel, Victor Funk, Huy Nguyen, Tim Wedl, Manuel Nutz, Michael Förg, Chriatian Mohl, Lukas Krelle, Sarah Rößle. Thank you Anna for providing SEM images. Thank you Jonas for sharing CVD growth experience. Thank you Jonathan for helping me solve software problems and load samples. Thank you Johannes for helping me translate the abstract into German.

I am very grateful to our collaborators Bernhard Urbaszek and Iann C. Gerber (Toulouse) for their contributions in theory calculation and explanation. Furthermore,

I want to thank Kenji Watanabe and Takashi Taniguchi (Japan) for providing high quality hBN.

I am also thankful to Philipp Altpeter for the invaluable support in all processes in the clean room and Christian Obermayer for the help with all matters around pumps, gas lines and other technology. Thank you Bert Lorenz and Dayse Ferreirae Silva for the constant help and making life easier. Thanks to Anton Heindl for the constant supply of nitrogen and helium.

I want to thank my country China and China Scholarship Council for its financial support during my PhD work, which allowed me to complete the project without too much pressure.

Finally, my thanks would go to my beloved family for their love and support in me all through these years.

Many thanks also to everyone I might have unintentionally forgotten to mention here.